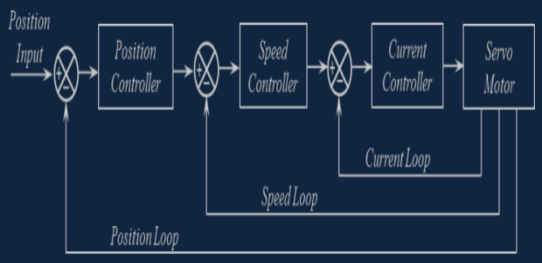

International Advanced Researches and Engineering Journal

e-ISSN

2618-575X

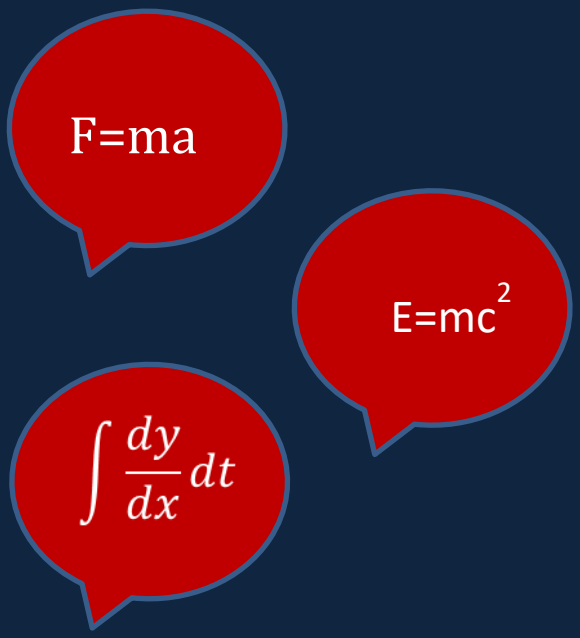

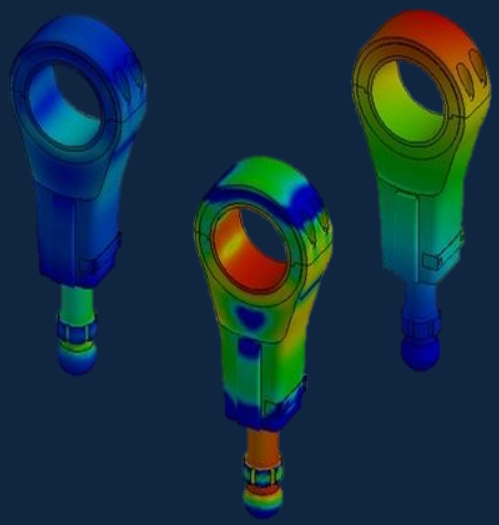

Volume 06 | **Issue** 01

April, 2022

e-ISSN: 2618-575X

Available online at www.dergipark.org.tr/en

INTERNATIONAL ADVANCED RESEARCHES
and
ENGINEERING JOURNAL

Journal homepage: www.dergipark.org.tr/en/pub/iarej

International
Open Access

Volume 06
Issue 01

April, 2022

International Advanced Researches and Engineering Journal (IAREJ) is a double-blind peer-reviewed and publicly available online journal that has Editorial Board (https://dergipark.org.tr/en/pub/iarej/board). The editor in chief of IAREJ welcomes the submissions that cover theoretical and/or applied researches on **Engineering** and related science with Engineering. The publication language of the Journal is **English**. **Writing Rules** are given in Author Guidelines (https://dergipark.org.tr/en/pub/iarej/writing-rules). IAREJ publishes **original papers** that are research papers and technical review papers.

IAREJ publication, which is **open access**, is **free of charge**. There is no article submission and processing charges (APCs).

IAREJ is indexed & abstracted in:

Crossref (Doi beginning: 10.35860/iarej.xxxxxx)
Directory of Open Access Scholarly Researches (ROAD)
Directory of Research Journals Indexing (DRJI)
EBSCO
Google Scholar
Index Copernicus (ICI Journal Master List)
J-Gate
TUBITAK ULAKBIM TR Dizin (TR index)
WorldCAT

Authors are responsible from the copyrights of the figures and the contents of the manuscripts, accuracy of the references, quotations and proposed ideas and the Publication Ethics (https://dergipark.org.tr/en/pub/iarej/page/4240).

e-ISSN: 2618-575X

Available online at www.dergipark.org.tr/en

INTERNATIONAL ADVANCED RESEARCHES
and
ENGINEERING JOURNAL

Journal homepage: www.dergipark.org.tr/en/pub/iarej

International
Open Access

Volume 06
Issue 01

April, 2022

Table of Contents

Available online at www.dergipark.org.tr/en

INTERNATIONAL ADVANCED RESEARCHES and ENGINEERING JOURNAL

Journal homepage: www.dergipark.org.tr/en/pub/iarej

e-ISSN: 2618-575X

International Open Access

Volume 06
Issue 01

April, 2022

Research Article

A novel approach for prediction of daily streamflow discharge data using correlation based feature selection and random forest method

Levent Latifoğlu [a,*]

[a]*Erciyes University, Engineering Faculty, Civil Engineering Dept., Kayseri, Turkey*

ARTICLE INFO

Article history:
Received 25 August 2021
Accepted 22 February 2022
Published 15 April 2022

Keywords:
Correlation-based feature selection
Forecasting
Random Forest
Streamflow discharge

ABSTRACT

The accurate methods for the forecasting of hydrological characteristics are significantly important for water resource management and environmental aspects. In this study, a novel approach for daily streamflow discharge data forecasting is proposed. Streamflow discharge, temperature, and precipitation data were used for feature extraction which were systematically employed for forecasting studies. While the correlation-based feature selection (CFS) was used for feature selection, Random Forest (RF) model is employed for forecasting of following 7 days. Moreover, an accuracy comparison between the RF model and CFS-RF model is drawn by using streamflow discharge data. Acquired results confirmed the accuracy of CFS-RF model for both, middle and extended forecasting times compared to RF model which had similar accuracy values for the closer forecasting times. Moreover, the CFS-RF model proved to be much robust for extended forecasting durations.

1. Introduction

The world population has increased dramatically in the latter half of previous century. However, the scarcity of water is the most pressing issue that sustainable survival of human civilization is facing. Against this backdrop, conservation of water resources needs urgent attention. On the other hand, accurate estimation of water characteristics such as precipitation, flow, evaporation, runoff, land use, and basin characteristics is critical to manage water resources. Furthermore, these estimates have a significant role in minimizing the fallouts of natural disasters such as drought and floods. Above all, one of the most crucial parameter is the streamflow discharge [1]. Moreover, there is an essential role of streamflow data in dam project design, basin management, hydroelectric energy capacity determination, flood control projects etc. Irregularities in water flow may result in significant economic losses and permanent damage to the environment around the river. The factor causing variation in river flows include change in climate, the greenhouse gases emissions, and meteorological and hydrological features [1, 2].

Streamflow discharge processes are challenging to forecast due to their dynamic nature, complexity, non-stationarity, non-linearity. Therefore, the challenges involved in forecast accuracy of streamflow discharge made it an attractive area of research among hydrologists.

Traditionally, time series have been evaluated using models such the Autoregressive Integrated Moving Average (ARIMA) using linear approach which is a parametric approach [3,4]. However, due to the non-stationary and non-linear nature of streamflow discharge data, Artificial Intelligence (AI) techniques have been introduced [5-7].

Furthermore, while predicting streamflow discharge Artificial Neural Network (ANN) based models provided better forecast accuracy. In addition, for estimation of streamflow discharge, models such as generalized regression, radial basis neural networks along with meteorological data are available now [8, 9]. Likewise, in water resource management and hydrological prediction, support vector machines are widely used. [10]. In previous literature, Streamflow discharge data were analyzed as signals, and decomposed using Discrete Wavelet Transform (DWT), Singular Spectral Analysis (SSA), Empirical Mode Decomposition (EMD), and Fourier Transform. The previous values of streamflow discharge data and the sub-band components of the signals are estimated using ANN, Support Vector Machines, and other techniques [6, 7, 11]. In addition, forecasting

* Corresponding author. Tel.: +90 352 207 6666; Fax: +90 352 437 5784.
E-mail addresses: latifoglu@erciyes.edu.tr *(L. Latifoğlu)*
ORCID: 0000-0002-2837-3306 *(L. Latifoğlu)*
DOI: 10.35860/iarej.987245

building energy, streamflow discharge, day-ahead load, an hour ahead wind power and electrical short-term load, Random Forest (RF) is also used in literature [12-15].

The present study used an ensemble of CFS and RF as a novel approach to forecast daily streamflow discharge data. The main contributions of the present study are:

- It proposes a forecasting method for streamflow discharge data with better accuracy by using previous data (seven days before the first forecast day).
- Systematically extracted features from the daily streamflow discharge, precipitation, and temperature data were used using CFS-RF model for training and validation of the proposed method.

2. Materials and Methods

The input data used in this study is based on streamflow discharge (Q), precipitation (P) and temperature (T_{max}, T_{min}) values. The streamflow discharge data (16527 datapoints) was recorded over a period of 46 years from Kootenay River near Skookumchuck basin in British Columbia, Canada. The exact coordinates of the drainage basin location at which data was collected are reported as 49°54'38" N, 115°44'08" W (latitude: 49.91056061, longitude: 115.7355576) as shown in Figure 1. The data was obtained from CANOPEX database [16, 17] from a drainage area of 7196.93 km^2.

Figure 2 shows how the above-mentioned input data was used for the forecast model by utilizing seven days previous data for predicting the discharge data for the following seven days. While the previous seven days are denoted as one-to-seven previous data, the following seven days are mentioned as one-to-seven ahead data. One-to-seven data (denoted as t-n while n takes the value of 1 to 7) for each input (i.e., Q, P, T_{max}, T_{min}, a total of 28 dataset values). Correlation-based method (CFS) was used for selecting the features from the above mentioned 28 datasets for forecasting of one-to-seven ahead data. Also, Figure 2 shows the overall methodology as well as data constituents used for the development of CFS-RF model.

This model is based on 3 steps. The first step is distinguishing between the training and testing data. The second step is feature extraction from the input datasets of 28 values as shown in Table 1. The third step comprises of the application of selected features using RF model and this way a forecasting model was achieved. Later the accuracy of the trained forecasting model was evaluated using the testing data.

More specifically, 70% of the datapoints belonging to all input datasets (P, Q, T_{max}, T_{min}) were used for training the forecasting model. The remaining 30% of the data was used for checking the accuracy of the model.

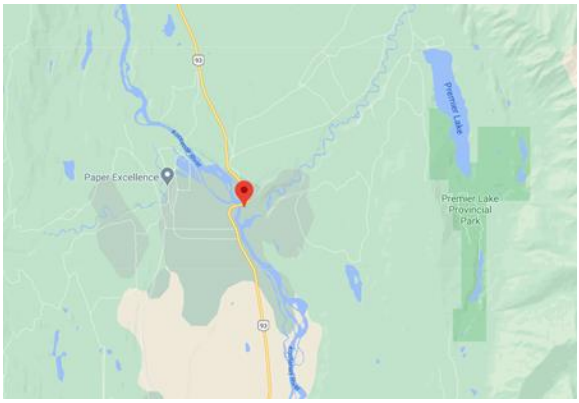

Figure 1. Map of Kootenay River Near Skookumchuck

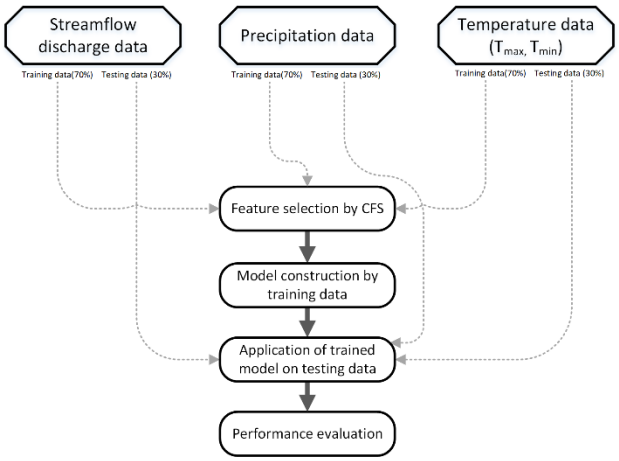

Figure 2. The proposed CFS-RF forecasting model for daily streamflow discharge data

Table 1. Selected features for forecasting of Q(t)

Total features	
Tmax(t-1), Tmax(t-2), Tmax(t-3), Tmax(t-4), Tmax(t-5), Tmax(t-6), Tmax(t-7)	
Tmin(t-1), Tmin(t-2), Tmin(t-3), Tmin(t-4), Tmin(t-5), Tmin(t-6), Tmin(t-7)	
P(t-1), P(t-2), P(t-3), P(t-4), P(t-5), P(t-6), P(t-7)	
Q(t-1), Q(t-2), Q(t-3), Q(t-4), Q(t-5), Q(t-6), Q(t-7),	
Selected Features for One Ahead Forecast	**Output**
Tmax(t-2), Tmin(t-5), Tmin(t-7), P(t-1), Q(t-1)	Q(t)
Selected Features for Two Ahead Forecast	**Output**
Tmax(t-2), Tmin(t-1), P(t-1), P(t-6), Q(t-1)	Q(t+1)
Selected Features for Three Ahead Forecast	**Output**
Tmax(t-3), Tmin(t-1), Tmin(t-1),P(t-1), P(t-2), P(t-7), Q(t-1)	Q(t+2)
Selected Features for Four Ahead Forecast	**Output**
Tmax(t-1), P(t-5), P(t-6), P(t-7), Q(t-1)	Q(t+3)
Selected Features for Five Ahead Forecast	**Output**
Tmax(t-1), P(t-4), P(t-5), P(t-6), P(t-7), Q(t-1)	Q(t+4)
Selected Features for Six Ahead Forecast	**Output**
Tmax(t-1), P(t-4), P(t-5), P(t-6), P(t-7), Q(t-1)	Q(t+5)
Selected Features for Seven Ahead Forecast	**Output**
Tmax(t-1), P(t-4), P(t-5), P(t-6), P(t-7), Q(t-1)	Q(t+6)

Training and testing streamflow discharge data used in this study are shown in Figure 3. Correlation coefficient for all datasets until t (the forecast day) to t-7 (seven days before the forecast day) is shown in Table 2.

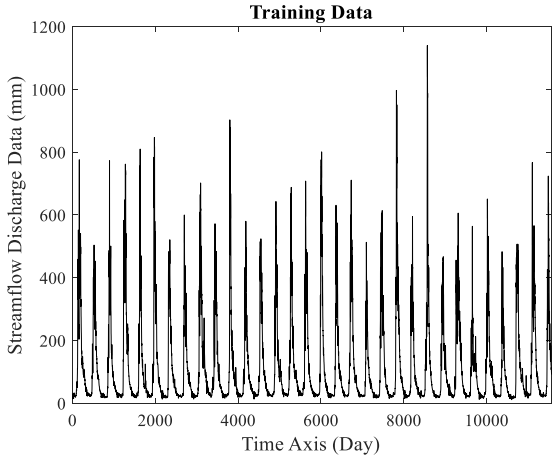

a)

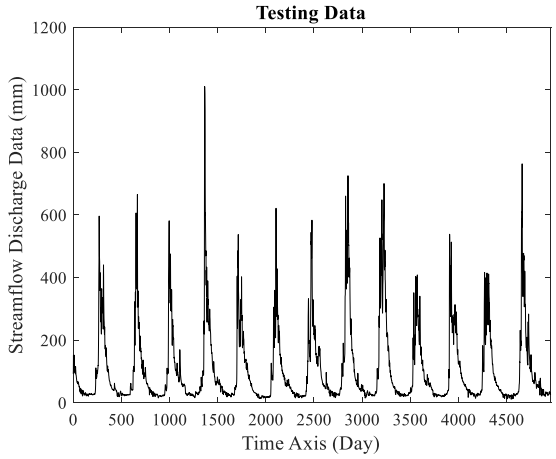

b)

Figure 3. Daily streamflow data measured on Kootenay River Near Skookumchuck basin a) Training Data, b) Testing Data

Table 2. Correlation Coefficient until (t) to (t-7)

Training Correlation Coefficient (t) to (t-7)	Testing Correlation Coefficient (t) to (t-7)
Streamflow Discharge Data	
0.9887, 0.9656, 0.9423, 0.9219, 0.9043, 0.8894	0.9877, 0.9628, 0.9372, 0.9139, 0.8931, 0.8739
Precipitation Data	
0.3259, 0.0897, 0.0599, 0.0513, 0.0454, 0.0473	0.3171, 0.0679, 0.0477, 0.0369, 0.0484, 0.0775
Maximum Temperature Data	
0.9623, 0.9184, 0.8863, 0.8645, 0.8487, 0.8365	0.9586, 0.9111, 0.8766, 0.8528, 0.8358, 0.8243
Minimum Temperature Data	
0.9325, 0.8678, 0.8250, 0.7956, 0.7745, 0.7595	0.9368, 0.8691, 0.8232, 0.7893, 0.7613, 0.7378

2.2 Feature Selection

The feature selection is a machine learning preprocessing stage that reduces the dimensionality of the data, removes irrelevant data, improves learning accuracy, and result comprehensibility. CFS method is a peculiar approach used for regression of datasets by evaluating the classification capabilities of the inherent features. This model prefers non-contradicting features from the datasets by examining its relationship with the expected classification criteria. The CFS model uses the entropy based information theory. The definition of entropy is shown in Equation (1).

$$H(x) = -\sum_{x \in X} P(x_i) log2(P(x_i)) \quad (1)$$

The entropy of variable x is calculated using conditional probability, as shown in Equation 2 based on the input values of y.

$$H(x/y) = -\sum_{x \in X} P(y_j) \sum_{y \in Y} P(x_i/y_j)\, log2(P(x_i/y_j)) \quad (2)$$

Where $P(x_i)$, $P(x_i/y_j)$ are the prior probability for all x values and the posterior probability for x and y values, respectively. Mutual information is defined as the amount by which the entropy of x as a result of additional information about x given by y shown in Equation 3.

$$gain(x/y) = H(x) - H(x/y) \quad (3)$$

If the gain(x/y) > gain(z/y), we can infer that feature y is more associated with feature x than to feature z.

Equation 4 shows the symmetrical uncertainty coefficient (SUC), an important metric which shows the relationship between the features

$$SUC = 2x(\frac{gain}{H(y) + H(x)}) \quad (4)$$

The SUC shows its tendency towards the relationship and has a normalized value with the range [0,1]; 1 denotes that one's knowledge completely predicts the value of the other, whereas 0 denotes that x and y are unrelated. It symmetrically handles a pair of attributes [18].

2.3 Random Forest Algorithm

The random forest (RF) is an ensemble approach that combines the predictions of numerous decision trees into a single forecast and can be used for both, regression and classification problems. Leo Breiman [19] invented the RF technique in 2001. The main principle is bagging, which involves randomly selecting a sample of size m from the training set and fitting it to a regression tree. This is known as a bootstrap sample, and it is picked using replacement, meaning that the same observations may appear many times [20]. The RF algorithm is applied as follows:

- With the Bootstrap method, n size data set is selected. This data set is split into two sections: training data and test data.
- The largest decision tree (CART) is generated using the training dataset, and this decision tree is not pruned. When dividing each node in this tree, m out of a total of p estimator variables are chosen randomly. The condition m<p must be satisfied in this situation because it is undesirable to see the tree grow too fast and adapt too soon. The highest knowledge gain among the m estimators chosen is used for branching. The value of this variable is decided by the Gini index. This process is repeated until there are no more branches to be created for each node.
- Each leaf node is assigned a class. The test data set is then at the top of the tree, and each observation in this data set is assigned to a class.
- All stages from 1st to 3rd step are repeated N times.
- The tree is evaluated using observations that were not used during the development process. The repeat number of observations is used to classify the data.
- A majority of votes is used to decide class assignments for each observation, tree set.

Random forest parameters in Table 3 were established by trial and error throughout the model's creation, taking into consideration calculation time and predicting performance.

2.4 Performance Evaluation

In this study, The Root Mean Square Error (RMSE), The Mean Absolute Error (MAE), The Correlation Coefficient (R) and The Determination Coefficient (R^2) were used to show the performance of the proposed method [21].

The differences between observed time series data and forecasted data by the proposed model are measured by average absolute error. MAE is described as follows:

$$MAE = \frac{1}{N}\sum_{i=1}^{N}|X_{observed,i} - X_{estimated,i}| \quad (5)$$

RMSE is calculated by root of squared the average difference across the time series data. RMSE is denoted by the following equation:

$$\mathrm{RMSE} = \sqrt{\frac{1}{\mathrm{N}}\sum_{\mathrm{i=1}}^{\mathrm{N}}(\mathrm{X_{observed,i}} - \mathrm{X_{estimated,i}})^2} \quad (6)$$

The R value shows the magnitude, direction, and significance of the relationship between measured and forecasted time series data. The R represents the correlation coefficient, which has a value between [-1, 1]. The R value is determined as shown in Equation 7:

Table 3. Random Forest Parameters used in the forecasting study

	Trials	**The best result for forecasting**
Number of iterations	100, 200, 300, 400	300
Number of attributes to randomly investigate	0, 1, 2	0
Number of folds for backfitting	0 ,1	0
Size of each bag, as a percentage of the training set size	70, 80, 100	100
Seed for random number generator	Yes, No	Yes
The desired batch size for batch prediction	70, 80, 100	100

$$\mathrm{R} = \frac{1}{\mathrm{N}-1}\sum_{\mathrm{i=1}}^{\mathrm{N}}\left(\frac{\mathrm{X_{observed,i}} - \mu_{\mathrm{X}}}{\sigma_{\mathrm{X}}}\right)\left(\frac{\mathrm{X_{estimated,i}} - \mu_{\mathrm{Xe}}}{\sigma_{\mathrm{Xe}}}\right) \quad (7)$$

While $\boldsymbol{X_{observed,i}}$ shows the measured data, $\boldsymbol{\mu_X}$ is the average, $\boldsymbol{X_{estimated,i}}$ is predicted data and $\boldsymbol{\sigma_X}$ is the standard deviation of the measured data, $\boldsymbol{\mu_{Xe}}$ shows the average of the predicted data is and the standard deviation $\boldsymbol{\sigma_{Xe}}$.

The R^2 coefficient is widely used to measure the predictability of hydrological models and is described as shown in Equation 8. This statistical criterion takes the value between -∞ and 1. The closer the R^2 value is to 1, higher is the forecast accuracy. [22]. The R^2 value is calculated using the following equation:

$$\mathrm{R^2} = 1 - \frac{\sum_{\mathrm{i=1}}^{\mathrm{N}}[\mathrm{X_{observed,i}} - \mathrm{X_{estimated,i}}]^2}{\sum_{\mathrm{i=1}}^{\mathrm{N}}[\mathrm{X_{observed,i}} - \mu_{\mathrm{X}}]^2} \quad (8)$$

Weka and MATLAB software packages are used to perform all the required calculations.

3. Results and Discussion

The results of the feature selection are given in Table 1. Figures 4, 5, and 6 respectively show the graphical representation of the trained model for the forecasting of t, t+1, t+2 forecasts for streamflow discharge data, out of total t+7 forecasts.

Table 4 on the other hand shows the numerical values of the total forecast from t to t+6.

Q(t-1) feature was applied to obtain Q(t) value for one ahead forecasting, Q(t-1) feature was applied to obtain Q(t+1) value for two ahead forecasting, Similarly, Q(t-1), data was applied as input features for three (Q(t+2)), four (Q(t+3)), five (Q(t+4)), six (Q(t+5)) and seven (Q(t+6)) ahead forecasting. Obtained performance parameters using Q(t-1) feature and RF model are given in Table 5.

Table 4. 1-7Ahead Forecasting performance of CFS-RF Model

	RMSE	MAE	R	R^2
One Ahead	17.9864	8.1520	0.9895	0.9791
Two Ahead	30.1717	13.3113	0.9703	0.9414
Three Ahead	41.2998	19.0428	0.9442	0.8914
Four Ahead	49.0520	23.0490	0.9212	0.8486
Five Ahead	54.5374	26.2710	0.9021	0.8138
Six Ahead	59.0526	28.7231	0.8852	0.7837
Seven Ahead	63.1710	30.7558	0.8685	0.7542

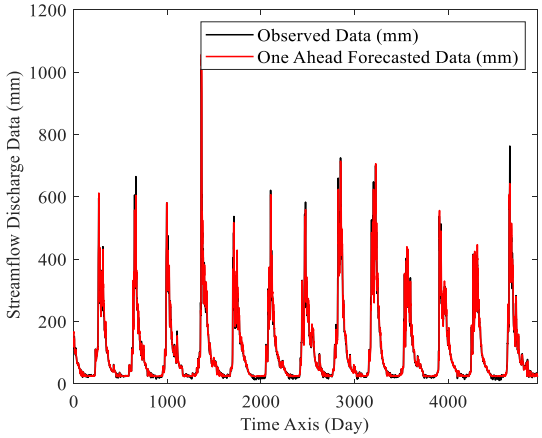

(a)

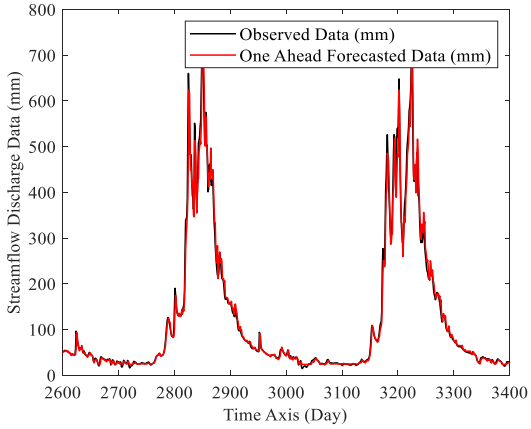

(b)

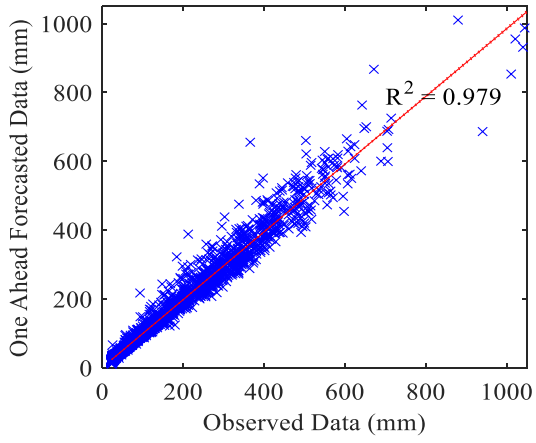

(c)

Figure 4. a) One-ahead forecasting of daily streamflow discharge data using CFS-RF Model, b) Zoomed graphic, c) Scatter plot

In the area of water resources planning and management, efficient water resource utilization demands accurate and successful streamflow discharge data forecasting [23]. A forecasting framework was established in this study to investigate the efficacy of the CFS-RF model with a novel approach. An estimation of daily streamflow discharge data for the upcoming seven days was performed using the CFS-RF model. Daily streamflow discharge data was divided into training and testing data. A comparative analysis was drawn between the forecasting capabilities of single RF model and the CFS-RF model combined.

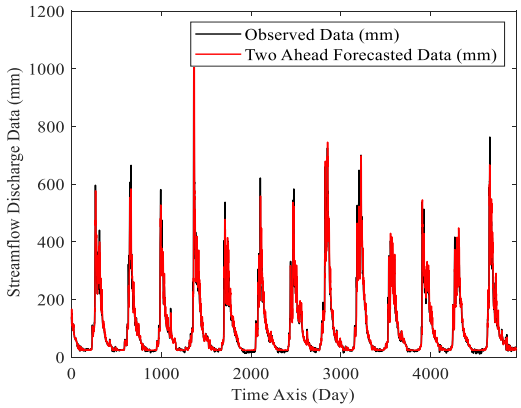

(a)

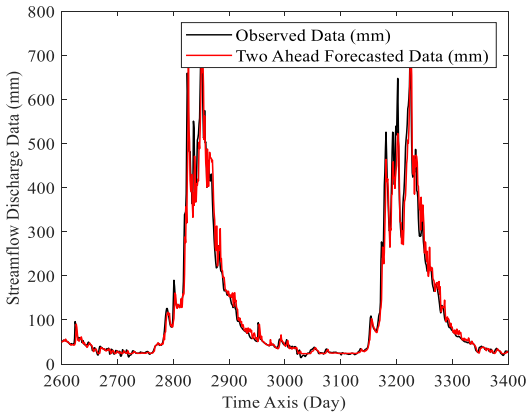

(b)

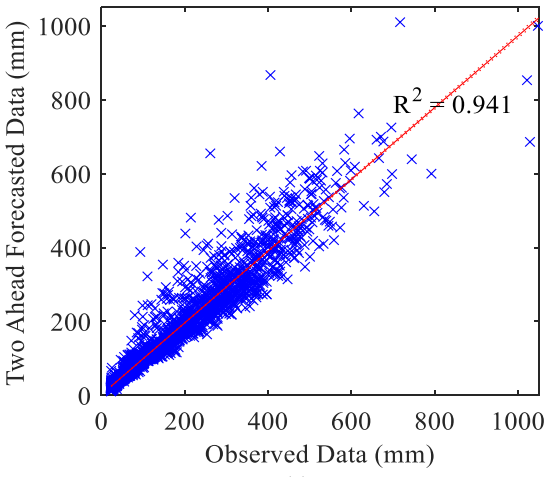

(c)

Figure 5. a) Two-ahead forecasting of daily streamflow discharge data using CFS-RF Model, b) Zoomed graphic, c) Scatter plot

It can be seen from the Table 4 that the R^2 value for the t to t+4 is above 0.80 compared to much later forecast days such as t+5 and t+6 for which the R^2 value is slightly above 0.75. Moreover, the value of R^2 for much earlier forecasts (t and t+1) are above 0.94 as shown in Figure 4 and 5 as well. As significantly linear relation between the forecasted and actual (real) values can be seen (see Figure 4 and 5).

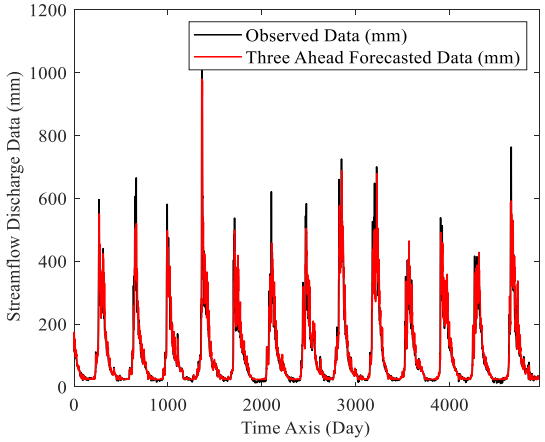

(a)

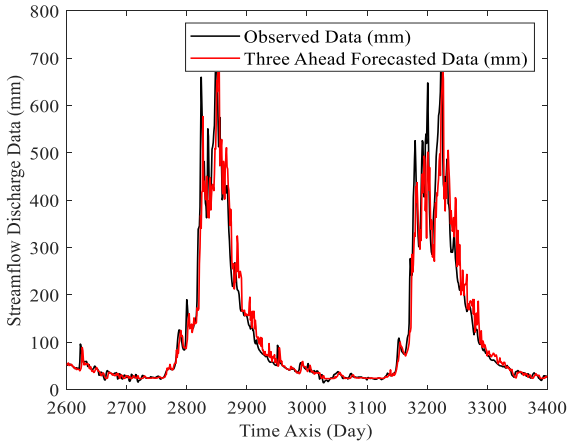

(b)

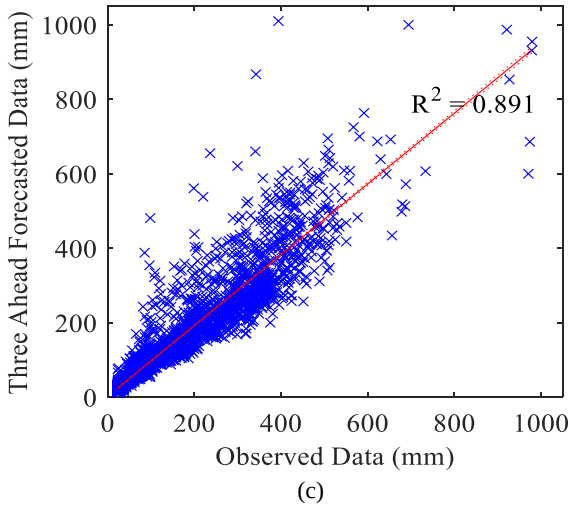

(c)

Figure 6. a) Three-ahead forecasting of daily streamflow discharge data using CFS-RF Model, b) Zoomed graphic, c) Scatter plot

Table 5. 1-7 Ahead Forecasting performance of RF Model

	RMSE	MAE	R	R^2
One Ahead	20.7351	9.3833	0.9859	0.9720
Two Ahead	35.5437	15.7612	0.9584	0.9184
Three Ahead	45.6941	20.5596	0.9307	0.8661
Four Ahead	77.7896	38.8902	0.7922	0.6276
Five Ahead	81.1282	41.0384	0.7725	0.5968
Six Ahead	84.3759	43.1028	0.7535	0.5678
Seven Ahead	87.0211	44.9170	0.7366	0.5426

The forecast study results acquired by CFS-RF model using only streamflow discharge data are given in in Table 5 in order to compare the reliability of CFS-RF and only RF model. It can be clearly seen, after inspecting the numerical values of the Table 4 and 5, that although CFS-RF model given much accurate results for mediocre (t+3 and t+4 forecasting) and extended (t+5, t+6) forecasting, it has low accuracy values for much recent forecasting. Similar scenario is valid for the RF model for closer forecasting time; however, its accuracy is slightly lower than the CFS-RF model.

4. Conclusion

Using temperature and precipitation data instead of only streamflow discharge data increases the forecast performance. Also, the selection of input features plays an important role for model performance and the accuracy of the results. In this study, it is recommended that temperature data, precipitation data in addition to streamflow discharge data should be used to obtain the best input variable combination for forecasting of streamflow discharge data.

Based on the findings, it is established that the RF model combined with CFS model shows an inherent superior capability of streamflow discharge forecasting for the river of Kootenay, Canada.

The proposed model appears to be an important tool that can be used in forecasting studies.

Declaration

The author declared no potential conflicts of interest with respect to the research, authorship, and/or publication of this article. The author also declared that this article is original, was prepared in accordance with international publication and research ethics, and ethical committee permission or any special permission is not required.

Author Contributions

L. Latifoğlu developed the methodology, performed the analysis and wrote the whole article.

References

1. Sharma, P. and D. Machiwal, *Advances in streamflow forecasting: from traditional to modern approaches*. 2021, USA: Elsevier, Inc.
2. Peters, R.L., *The greenhouse effect and nature reserves*. Bioscience, 1985. **35**(11): p.707-717.
3. Rojas, I., O. Valenzuela, F. Roja, A. Guillén, L.J. Herrera, H. Pomares, L. Marquez, and M. Pasadas, *Soft-computing techniques and ARMA model for time series prediction*. Neurocomputing, 2008. **71**(4-6): p. 519-537.
4. Khandelwal, I., R. Adhikari, and G. Verma, *Time series forecasting using hybrid ARIMA and ANN models based on DWT decomposition*. Procedia Computer Science, 2015. **48**: p. 173-179.
5. Yaseen, Z. M., A. El-Shafie, O. Jaafar, H.A. Afan, and K.N. Sayl., *Artificial intelligence based models for stream-flow forecasting: 2000–2015*. Journal of Hydrology, 2015. **530**: p. 829-844.
6. Kisi, O., L. Latifoğlu, and F. Latifoğlu, *Investigation of empirical mode decomposition in forecasting of hydrological time series*. Water Resources Management, 2014. **28**(12): p. 4045-4057.
7. Latifoğlu, L., O. Kişi, and F. Latifoğlu, *Importance of hybrid models for forecasting of hydrological variable*. Neural Computing and Applications, 2015. **26**(7): p. 1669-1680.
8. Meshram, S.G., C. Meshram, C.A.G. Santos, B. Benzougagh, and K.M. Khedher, *Streamflow prediction based on artificial intelligence techniques.* Iranian Journal of Science and Technology, Transactions of Civil Engineering, 2021. p. 1-11.
9. Nourani, V., N.J. Paknezhad, and H. Tanaka, *Prediction interval estimation methods for artificial neural network (ANN)-based modeling of the hydro-climatic processes, a Review*. Sustainability, 2021. **13**(4): p. 1633.
10. Adnan, R. M., X. Yuan, O. Kisi, and Y. Yuan, *Streamflow forecasting using artificial neural network and support vector machine models*. American Scientific Research Journal for Engineering, Technology, and Sciences (ASRJETS), 2017. **29**(1): p. 286-294.
11. Saraiva, S. V., F. de Oliveira Carvalho, C.A.G. Santos, L.C. Barreto, and P.K.D.M.M Freire, *Daily streamflow forecasting in Sobradinho Reservoir using machine learning models coupled with wavelet transform and bootstrapping*. Applied Soft Computing, 2021. **102**: p.107081.
12. Pham, L. T., L. Luo, and A. Finley, *Evaluation of random forests for short-term daily streamflow forecasting in rainfall-and snowmelt-driven watersheds*. Hydrology and Earth System Sciences, 2021. **25**(6): p. 2997-3015.
13. Li, X., J. Sha, and Z.L. Wang, *Comparison of daily streamflow discharge forecasts using extreme learning machines and the random forest method.* Hydrological Sciences Journal, 2019. **64**(15): p. 1857-1866.
14. Lahouar A. and J.B.H. Slama, *Day-ahead load forecast using random forest and expert input selection*. Energy Conversion and Management, 2015. **103**: p. 1040-1051.
15. Huo, J., T. Shi and J. Chang., *Comparison of random forest and SVM for electrical short-term load forecast with different data sources*, in 7th IEEE International conference on software engineering and service science (ICSESS), 2016, Beijing: China. p. 1077-1080.
16. Canopex hydrometeorological watershed database. [cited 2020 1 December]; Available from: http://canopex.etsmtl.net/
17. Arsenault, R., R. Bazile, C. Dallaire-Ouellet, and F. Brissette, *CANOPEX: A Canadian hydrometeorological watershed database*. Hydrological Processes, 2016. **30**(15): p. 2734-2736.
18. Gopika, N. and A. Kowshalaya M.E, *Correlation based feature selection algorithm for machine learning*, in 3rd International Conference on Communication and Electronics Systems (ICCES), 2018, Coimbatore: India. p. 692-695.
19. Breiman L., *Random forests*. Machine Learning, 2001, **45**: p. 5–32.
20. Liu Y., Y. Wang, and J. Zhang, *New machine learning algorithm: Random forest*, in International Conference on Information Computing and Applications, 2012, Chengde: China. p. 246-252.
21. Samanataray, S., and A. Sahoo, *A Comparative study on prediction of monthly streamflow using hybrid ANFIS-PSO approaches*. KSCE Journal of Civil Engineering, 2021. **25**(10): p. 4032-4043.
22. Ali, M.H. and I. Abustan, *A new novel index for evaluating model performance*. Journal of Natural Resources and Development, 2014. **4**: p. 1-9.
23. Kumbur, H., V. Yamaçlı, and A. Küçükbahar, *Mersin province water projections and water information and management system: Erdemli district model*. International Advanced Researches and Engineering Journal, 2018. **2**(3): p. 261-266.

Available online at www.dergipark.org.tr/en

INTERNATIONAL ADVANCED RESEARCHES and ENGINEERING JOURNAL

Journal homepage: www.dergipark.org.tr/en/pub/iarej

e-ISSN: 2618-575X

International Open Access

Volume 06
Issue 01

April, 2022

Research Article

Analyzing the effect of the Covid-19 pandemic on the water consumption of households, workplaces, and public institutions in Kocaeli, Turkey

Nadire Ucler [a,*]

[a] *Van Yuzuncu Yil University, Van Vocational School, Department of Construction, Van, Turkey*

ARTICLE INFO

Article history:
Received 29 November 2021
Accepted 18 March 2022
Published 15 April 2022

Keywords:
Covid-19 pandemic
Household
Lockdown
Public institution
The Wilcoxon test
Water consumption
Workplace

ABSTRACT

The COVID-19 pandemic, which has frightening effects on the health systems all over the world, has forced the governments to take strict measures to fight the terrible consequences of the virus. Both this disease and restrictive measures have caused people to change their consumption habits in this period. In this study, the changes in the water consumption amounts of households, workplaces, and public institutions before and after the pandemic were examined. Kocaeli, a socially and economically essential city of Turkey, was chosen as the study area. Temperature and population changes, which are other parameter that may affect water consumption, were also evaluated. In addition, the month when the full lockdown was applied and the period when all bans were abolished and life returned to normal were also evaluated comparatively. The Wilcoxon test was used to determine whether there was a statistically significant difference in the amount of water consumption between the pre-pandemic, during the pandemic, and post-pandemic period. The results showed that although there was no considerable change in temperature, household water consumption increased markedly 3 months after the first case was announced in Turkey. After the implementation of the pandemic measures, the amount of workplace water usage decreased in April and in May 2020. Additionally, the amount of public water consumption in 2020 was found significantly lower than in 2019. In the full lockdown month, an increase was observed in household and workplace water consumption, in contrast to a significant decrease in the water consumption of public institutions. Among the changes experienced in the last period of 2021, when life was relatively normal, only a significant change was observed in the household water consumption value.

1. Introduction

The COVID-19 pandemic spreading in a frightening way has led to health stresses throughout the world after the first case was reported in December 2019 in Wuhan, China [1]. The impact of the Covid-19 pandemic has not only been limited to health but has also begun to be felt in the social and economic field over time.

During the pandemic period, many countries have adopted measures such as the implementation of strict quarantines, the restrictions of public meetings and transportation, and imposing social distancing, curfews, and lockdowns to prevent the spread of the virus and deal with the negative outcomes of the disease.

Both the disease itself and the measures taken by the administrators caused changes in people's daily routines. This situation has also led many researchers from different disciplines to investigate the effects of the pandemic on different fields.

For instance, Menneer et al. [2] investigated the effects of full lockdown on domestic electricity, gas, and water usage in the UK. Results showed that a 17% increase occurred in water usage during full lockdown due to spending more time at home and washing more.

There are numerous studies investigating water quality of natural resources. Liu et al. [3], Yunus et al. [4] and Selvam et al. [5] have reported improvements in water quality during pandemic. These improvements may have been caused by a decrease in the activity of the factories where wastewaters are created, and thereby, a decrease in the number of pollutants that reach the resources [6].

Özbaş et al. [7] assessed the distinction between water

* Corresponding author. Tel.: +904322251414-22374; Fax: +904322251415.
E-mail addresses: nadireucler@yyu.edu.tr
ORCID: 0000-0001-6407-121X
DOI: 10.35860/iarej.1030213

footprint values of citizens with various socioeconomic standards pre-pandemic and during the pandemic period. According to their results, even though there was a rise in water consumption of many daily activities, the average water footprint value did not rise much because of the reduction in clothing spending and changes in car washing routines. Pesantez et al. [8] examined the effects of the water consumption change experienced during the pandemic process on the water distribution network and proposed a digital twin to couple Advanced Metering Infrastructure data with a hydraulic model.

Antwi et al. [9] have investigated water-related interventions in many European countries throughout the COVID-19 pandemic period. Their results showed that these interventions were predominantly short-term precautions to provide a continued water supply and to reduce the consumers' income decreases. In addition, researchers indicated that water could take a major place to revitalize the European countries' post-COVID-19 economy.

Also, the lockdown has led households to alter their ordinary consumption attitudes, which has caused a keen rise in expenditure, particularly in essentials and foods [10]. For example, a study indicated a prominent change in aggregate water demand peak from 07:10 pre-lockdown to 09:40 during the lockdown in Germany [11]. Similarly, in a study conducted by Abu Bakar [12], water consumption data obtained from 11,528 households over 20 weeks from January 2020 were analyzed. The results of this study revealed a considerable quantifiable alter in water consumption patterns during the COVID-19 lockdown period in the UK. The results of another study indicated that the COVID-19 pandemic influenced water consumption patterns and increased the stress on the already restricted water resources in Tabriz, Iran [13].

Abulibdeh [14] examined the water and electricity consumption during the COVID-19 pandemic across six socioeconomic sectors. The results showed that there was a difference in both consumptions at the block level across all sectors and over time.

Li et al. [15] analyzed how California's urban water consumption was affected by Covid-19 and it was found that the pandemic-related measures reduced California's urban water usage by 7.9%. This reduction was considered as largely connected to an 11.2% decline in the commercial, industrial, and institutional sectors, while there was a 1.4% increase in the water consumption of the residential areas. In another study, Kalbusch et al. [16] applied the Wilcoxon and Kruskal-Wallis non-parametric tests to investigate the effect of coronavirus spread-prevention measures on water consumption in Southern Brazil. Their results revealed that the water consumption differences between pre and post-pandemic periods were statistically significant. Additionally, a decrease in water consumption in the commercial, industrial, and public categories, and an increase in the residential category were detected.

The effects of the pandemic on water consumption continue to be examined at different scales, in different sectors, in regions of the world with different socio-economic characteristics [17-21].

Access to clean water can sometimes be challenging, especially for developing countries with limited budgets. Therefore, any situation that may affect water consumption behavior should be evaluated. Knowing the impact of an unpredictable pandemic on water usage habits will enable the water management decision-making mechanism to operate current water distribution systems and plan water resources more effectively.

The purpose of this study is to investigate whether water consumption of households, workplaces, and public institutions has been affected by the pandemic process. For this purpose, a region of Kocaeli province, which is one of the important industrial cities of Turkey and makes regular and reliable measurements, was determined as the study area.

2. Material and Method

2.1 Covid-19 in Turkey

The first Covid-19 case in Turkey was announced on March 11, 2020, and the first death due to the virus was announced on March 17, 2020 [22]. According to the World Health Organization Covid-19 Data [23], Turkey is one of the countries whose case numbers have exceeded 5 million (Figure 1).

After the Covid-19 pandemic showed its effects in Turkey, in line with the recommendations of the Scientific Committee, it was aimed to reduce the negative effects of the pandemic with measures such as travel restrictions, curfews, quarantine practices, closure of shopping centers and entertainment venues [24].

2.2 Method

It is essential that the data of water distribution systems are measured accurately and continuously, and the components are traceable and controllable. However, it is very difficult to implement these applications simultaneously throughout the distribution system. Therefore, to detect, reduce, and prevent water losses, District Metered Areas (DMA) are generally used as an effective and sustainable method. The borders of DMA are separated from other regions and network elements; hence, they can be defined as zones with a clearly determined entrance. In this study, the DMA-08 isolated region, which served 24 streets with 6377 m of secondary pipes and 3461 m of main pipes, in the Kocaeli city was selected as study area [25] (Figure 2).

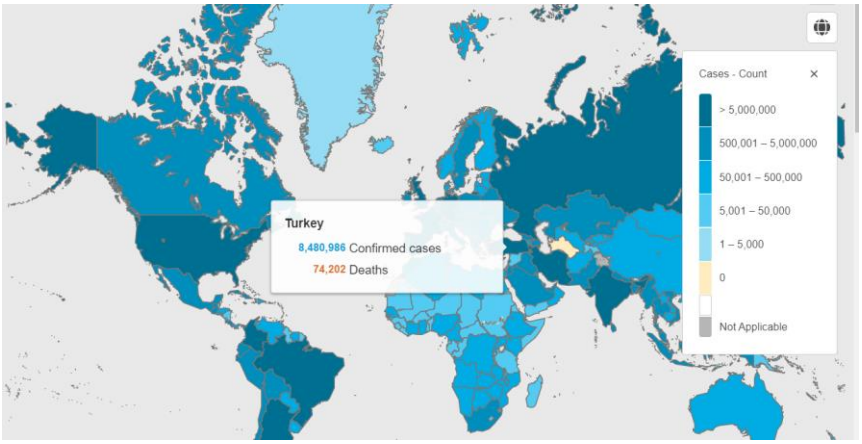

Figure 1. General Covid-19 situation in Turkey on 18.11.2021 [23]

The monthly water consumption values of the DMA-08 isolated region for 2019, 2020 and 2021, which were measured in average 3350 households, 30 workplaces, 20 public institutes, were examined. Since these numbers were not stable and changed every month, in order to make an objective comparison, the values obtained through dividing the monthly total accrual values by the total non-zero accrual number were used.

To compare the pre- and during-pandemic periods, March, when the first case was announced in Turkey, was considered as the starting month. Additionally, the date of July 1, 2021, when the restrictions were ended, all workplaces that had been suspended started their activities again, and the normal working order in public institutions was started, was accepted as the beginning of the normalization process for Turkey. Thus, a comparison of the change experienced after this date with the previous year was also used to determine the effect of the pandemic.

Figure 2. The study area [25]

Moreover, to consider population and temperature change, two other parameters that can affect the amount of water consumption, the population values of the region obtained from the Address Based Population Registration System [26] and temperature data of the Kocaeli station, were also checked.

The Wilcoxon test was used to determine whether the changes observed in the graphics and tables were statistically significant.

2.3 The Wilcoxon Test

The Wilcoxon test is a nonparametric test and used to determine if there are statistically significant differences between two dependent data sets [27]

The hypotheses for this test can be described as below:

H_0: the distributions of both data sets are equal. The sum of the positive and negative differences between the test results is equal.

H_1: the distributions are not equal. The sum of the negative differences is either very small or larger than the sum of the positive differences [27].

3. Results and discussion

3.1 Temperature and Population

The monthly average temperature values for 2019 and 2020 indicated that the temperature value in June 2020 was lower than the previous year, and it rose a few degrees above the previous year as of July (Figure 3). Additionally, the monthly average temperature value (19.4 °C) in May 2021 was equal to the average of the previous two years. Since September of 2021, the temperature values were below the other two years (except for December).

The Wilcoxon test was used to determine whether the monthly average temperature values of 2020 showed a statistically significant difference compared to 2019 and 2021.

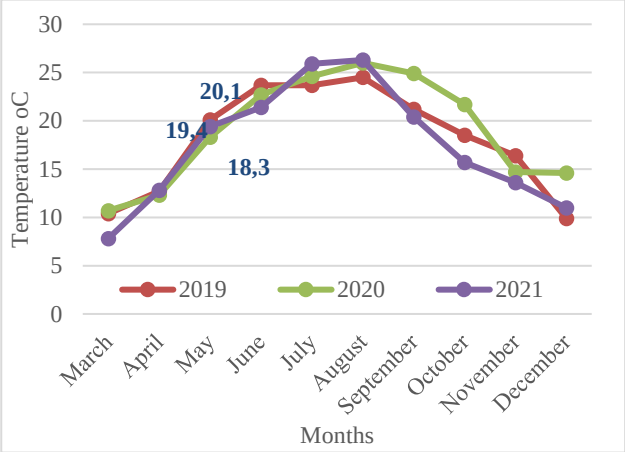

Figure 3. Monthly average temperature for 2019, 2020, and 2021

It was determined that the "z" value was -0.866 (p=0.386) for the comparison of 2019-2020, and it was -1.582 (p=0.144) for the comparison of 2020-2021. These results showed that since p values were greater than 0.05 significance level, there was no statistically significant difference between the temperature values of 2020 and the temperature values of 2019 and 2021.

Based on the results obtained from the Address Based Population Registration System, it was determined that the population of the region decreased by 0.4% and 0.77% in 2020 and 2021, respectively. It is not considered that these changes in the population had a significant effect on the amount of water consumption.

3.2 Household

It was investigated whether there were significant increases in household water consumption due to the transition to distance education, working from home in some sectors, and people's tendency to use more water by being more meticulous about protecting themselves from the virus.

Table 1 provides data on the comparison of household water consumption between 2019- 2020 and 2020- 2021. Negative values show the reductions of 2020 respect to 2019 and the reductions of 2021 respect to 2020.

It is seen that the consumptions in March 2020 and in the following two months, contrary to expectations, were less than the previous year, but there was a significant increase by 43.30% in June and remained high until the end of the year (excluding September). December was almost same with the previous year. (Figure 4). The Wilcoxon test was applied to 10-month values to determine whether the water consumption values of 2020 showed a statistically significant change compared to 2019 after the first case was announced. The test results revealed that there was no statistically significant difference between the household water consumption values of 2020 and 2019 (z=-1.274, p=0.203>0.05).

In addition, while the average temperature value was almost the same as in the other years, in May 2021, the water consumption value reached 10.79 m^3/household which was the highest value of the three years. The consumption value in May also had the highest value compared to the rest of 2021.

It was observed that since June of 2021 (excluding September), there was a decrease at varying rates compared to the 2020. The Wilcoxon test was applied to 6-month values to determine whether the water consumption values of 2021 showed a statistically significant difference compared to 2020 after the normalization steps. The test results showed that there was a statistically significant difference between the household water consumption values of 2021 and 2020 (z=-1.992, p=0.046<0.05).

3.3 Workplaces

Although their number varies on a monthly and yearly basis, there were an average of 30 workplaces in the study area. Within the scope of the pandemic measures implemented by the government, the activities of some workplaces such as cafes, restaurants, hairdressers, and sports centers were either completely stopped or restrictions were made in their working hours and capacities. Some workplaces, on the other hand, resorted to capacity reduction by putting some of their employees on paid leave or allowing them to work from home.

Table 2 shows the percentage of water consumption comparison between 2019-2020 and 2020–2021. Negative values show the reductions of 2020 respect to 2019 and the reductions of 2021 respect to 2020.

With the implementation of the restrictions within the scope of pandemic measures, the amount of water consumption decreased by 41.61% in April 2020 and 21.15% in May 2020. Although the June and July values were higher than the previous year, it can be said that water usage in 2020 was less than in 2019. However, based on the Wilcoxon test results (z=-0.734, p=0.445>0.05), it can be said that this usage difference was not statistically significant.

When the values for May 2021 were examined in terms of workplaces, it was seen that there was no decrease in the water consumption value, on the contrary, the consumption reached the highest value of three years in 2021. This situation can be explained by the fact that many workplace employees are excluded from the scope of the lockdown or continue to work with special permission. The increase in the water consumption values experienced in May 2021 decreased slightly in June and then increased again in July.

It was observed that since July of 2021 (excluding October), there was a decrease at varying rates compared to 2020. According to the Wilcoxon test results, this consumption difference is not statistically significant (z=-1.153, p=0.249>0.05).

Table 1. The household water consumption comparison between 2019 - 2020 and 2020 – 2021

%	March	April	May	June	July	August	September	October	November	December
2019_2020	-2.28	-8.18	-0.17	43.30	12.47	20.70	-3.22	12.75	8.50	-0.03
2020_2021	2.56	9.33	6.94	-32.46	-8.77	-13.49	0.14	-9.22	-10.66	-5.48

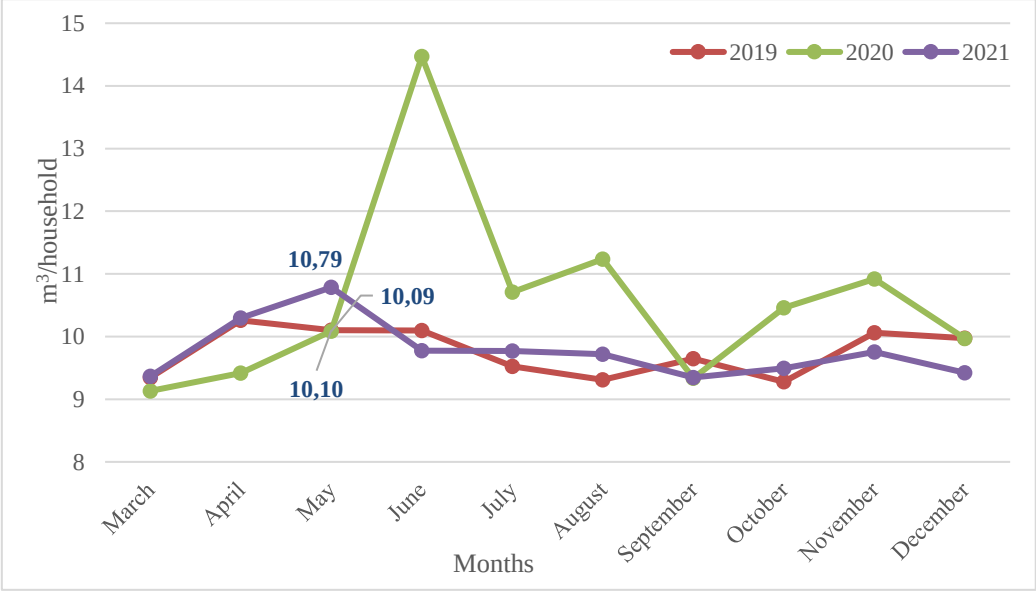

Figure 4. The monthly water consumption values of households in 2019, 2020 and 2021

Table 2. The workplace water consumption comparison between 2019 - 2020 and 2020 – 2021

%	March	April	May	June	July	August	September	October	November	December
2019_2020	9.41	-41.61	-21.15	26.76	13.86	-9.71	-1.85	-8.23	3.03	-27.26
2020_2021	-14.02	54.48	45.61	-24.47	-5.20	-4.90	-0.61	15.66	-17.31	-0.59

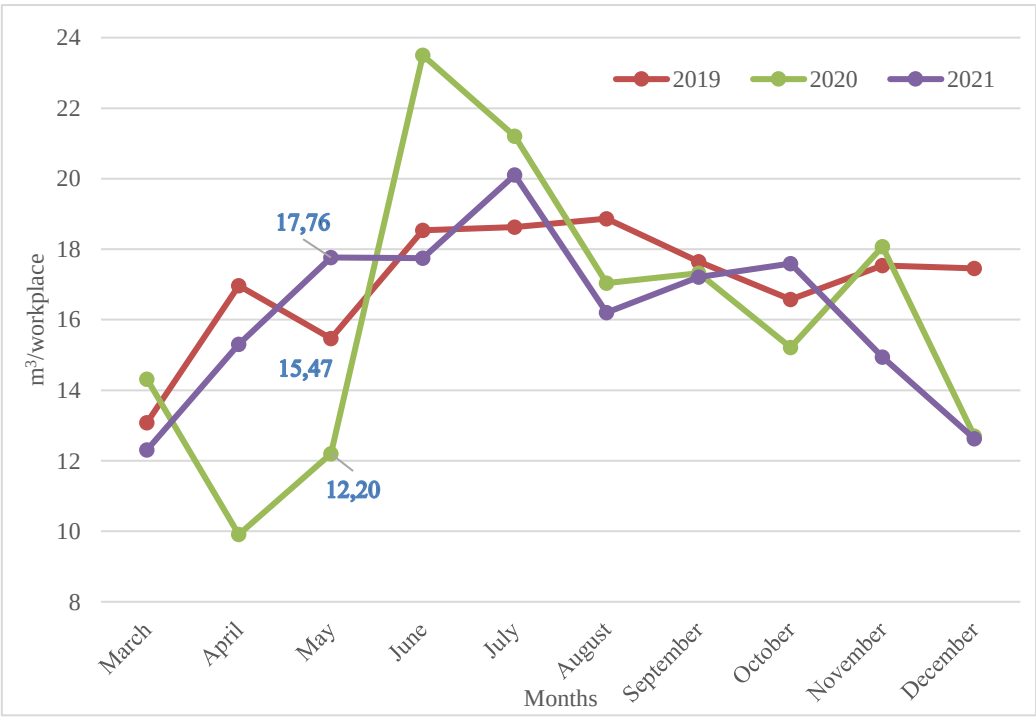

Figure 5. The monthly water consumption values of workplaces in 2019, 2020 and 2021

3.4 Public Institution

During the pandemic process, employees who were pregnant, with chronic diseases, and over the age of 65 were considered on administrative leave in public institutions. Educational institutions switched to distance education. To maintain social distance in closed places, some employees started to work on a rotating basis. While some health institutions started to serve only Covid patients, some citizens took care not to go to the hospital except for emergencies due to the fear of the virus. For these reasons, water consumption of public institutions was affected significantly. The rotating, flexible, and remote working practice, which was initiated with the circular published on March 22, 2020, within the scope of Corona Virus measures, ended on June 1, 2020. With the circular published on August 26, 2020, alternate, flexible, and remote working in public institutions and organizations was allowed again.

In the study area, there are an average of 20 public institutions. In Table 3, negative values show the reductions of 2020 respect to 2019 and the reductions of 2021 respect to 2020.

As can be seen in Table 3 and Figure 6, the water consumption amount of public institutions in 2020 was much less than the previous year, except for August. In June, July, and August, when the remote work permit was revoked, the rate of decrease in the amount of water consumption slowed down, and there was even an increase in August. The difference in consumption reached 76%, especially in the period when inspections were tightened, and events organized by official institutions, unions, and non-governmental organizations were postponed. The Wilcoxon test results showed that pandemic measures affected water consumption values in public institutions ($z=-2.293$, $p=0.022<0.05$).

When the water consumption values of public institutions in May 2021 are analyzed, it is seen that there was a dramatic decrease over the years. In addition, the water consumption values of public institutions for the rest of 2021 are higher than the consumption value in May. The water consumption values of 2021, which were significantly below the other two years until October, became more than the values of 2020 after this month and approached the values of 2019. This situation can be interpreted as the fact that the effects of the normalization process were felt more in the last two months of 2021. The Wilcoxon test results also support this situation, showing that the change in water consumption in the last 6 months is not statistically significant ($z=-0.943$, $p=0.345>0.05$).

Table 3. The public institution water consumption comparison between 2019 - 2020 and 2020 – 2021

%	March	April	May	June	July	August	September	October	November	December
2019_2020	-10.62	-43.18	-48.30	-38.31	-20.59	19.71	-66.31	-76.03	-57.58	-61.68
2020_2021	-77.46	-46.43	-51.22	-82.66	-83.62	-87.08	-57.54	0.79	41.58	22.09

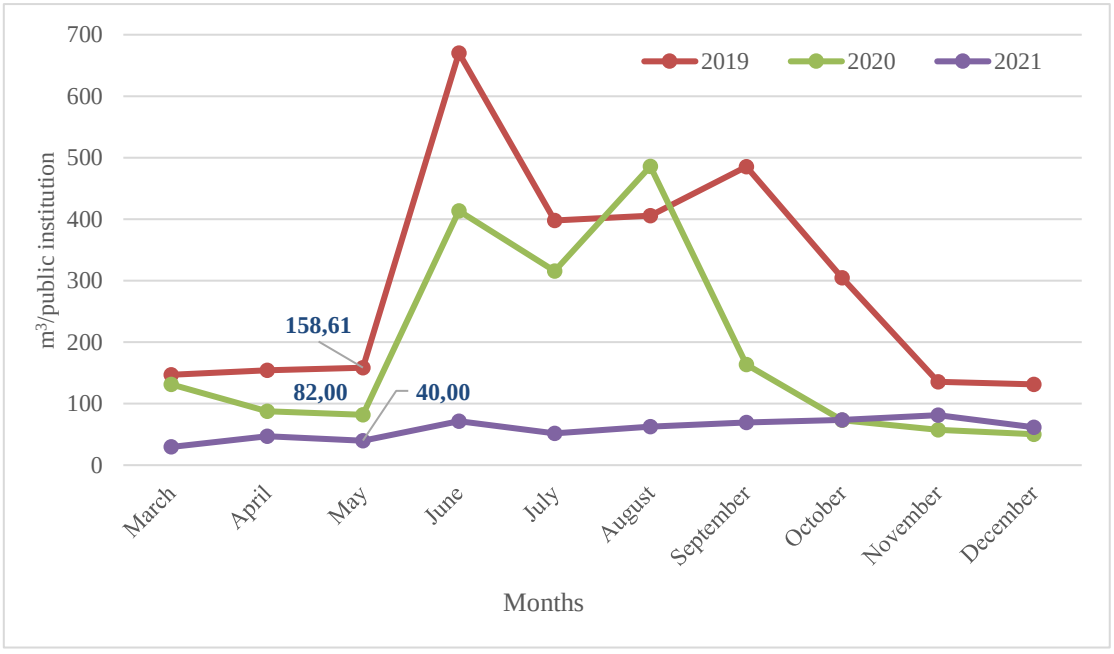

Figure 6. The monthly water consumption values of public institutions in 2019, 2020 and 2021

4. Conclusions

In this study, the effect of the pandemic process on the amount of water consumption in households, workplaces, and public institutions was investigated.

According to the results of the Wilcoxon test applied to understand whether the changes observed on a monthly basis are meaningful, as a period only the household water consumption value experienced after the normalization period and the change in the public institution water consumption values during the pandemic period compared to the previous year were found to be statistically significant.

Especially, to be able to understand the effects of the 19-day full lockdown precisely, it is necessary to reach the daily and hourly data of the subscribers separately instead of the total monthly consumption data.

Studies examining the effects of the pandemic process on water consumption are generally carried out for urban areas. However, conducting similar studies on rural water consumption is important in terms of understanding the effects of the pandemic on different socio-economic classes.

In addition, investigating the effects of the pandemic not only on the water consumption amounts of industrial facilities but also on the water demand of agriculture and livestock enterprises will allow us to see the widespread effect of the pandemic.

Declaration

The author declared no potential conflicts of interest with respect to the research, authorship, and/or publication of this article. The author also declared that this article is original, was prepared in accordance with international publication and research ethics, and ethical committee permission or any special permission is not required.

Author Contributions

N. Ucler obtained the data, analyzed them, and wrote the manuscript.

Acknowledgment

The data used in this study was obtained from the Kocaeli Water and Sewerage Administration Directorate.

References

1. Lu, R., Zhao, X., Li, J., Niu, P., Yang, B., Wu, H., … & Tan, W. *Genomic characterisation and epidemiology of 2019 novel coronavirus: implications for virus origins and receptor binding.* The lancet, 2020. **395**: p. 565-574.
2. Menneer, T., Qi, Z., Taylor, T., Paterson, C., Tu, G., Elliott, L. R., ... & Mueller, M. *Changes in domestic energy and water usage during the UK covid-19 lockdown using high-resolution temporal data.* International journal of environmental research and public health, 2021. **18**: 6818.
3. Liu, F., M., Wang, and M., Zheng, *Effects of COVID-19 lockdown on global air quality and health.* Sci. Total Environ, 2021. **755:** 142533.
4. Yunus, A.P., Y.,Masago, and Y., Hijioka, *COVID-19 and surface water quality: improved lake water quality during the lockdown.* Sci. Total Environ. 2020. **731**: 139012.
5. Selvam, S., K., Jesuraja, S., Venkatramanan, S.Y., Chung, P.D., Roy, P., Muthukumar, and M., Kumar, *Imprints of pandemic lockdown on subsurface water quality in the coastal industrial city of Tuticorin, South India: a revival perspective.* Sci. Total Environ. 2020. **738**: 139848.
6. Sivakumar, B., *COVID-19 and water.* Stoch. Environ. Res. Risk Assess. 2020. **6**: p. 10–13.
7. Özbaş E., E., Akın, Ö., Güneysu, S., Özcan, H. K., & Öngen, A. *Changes occurring in consumption habits of people during COVID-19 pandemic and the water footprint.* Environment, Development and Sustainability. 2021. p. 1-17.
8. Pesantez, J. E., Alghamdi, F., Sabu, S., Mahinthakumar, G., & Berglund, E. Z. *Using a digital twin to explore water infrastructure impacts during the COVID-19 pandemic.* Sustainable Cities and Society, 2022. **77:** 103520.
9. Antwi, S. H., D., Getty, S., Linnane, and A. Rolston, *COVID-19 water sector responses in Europe: A scoping review of preliminary governmental interventions.* Science of The Total Environment, 2021. **762**: 143068.
10. Baker, S. R., R. A., Farrokhnia, S., Meyer, M., Pagel, and C. Yannelis, *How Does Household Spending Respond to an Epidemic? Consumption During the COVID-19 Pandemic.* Rev. Asset. Pricing Stud. 2020. **10**: p. 834–862.
11. Aquatech. *Case study: Data links COVID-19 lockdown to consumption change*. [cited 2020 29 June]; Available from:https://www.aquatechtrade.com/news/utilities/covid-19-lockdownsimpact-water-consumption/.
12. Abu-Bakar, H., L., Williams, and S. H. Hallett, *Quantifying the impact of the COVID-19 lockdown on household water consumption patterns in England*. NPJ Clean Water, 2021. **4**(1): p. 1-9.
13. Feizizadeh, B., D., Omarzadeh, Z., Ronagh, A., Sharifi, T., Blaschke, and T., Lakes, *A scenario-based approach for urban water management in the context of the COVID-19 pandemic and a case study for the Tabriz metropolitan area, Iran.* Science of The Total Environment, 2021. **790**: 148272.
14. Abulibdeh, A. *Spatiotemporal analysis of water-electricity consumption in the context of the COVID-19 pandemic across six socioeconomic sectors in Doha City, Qatar.* Applied Energy, 2021. **304**: 117864.
15. Li, D., Engel, R. A., Ma, X., Porse, E., Kaplan, J. D., Margulis, S. A., & Lettenmaier, D. P. *Stay-at-home orders during the COVID-19 pandemic reduced urban water use.* Environmental Science & Technology Letters, 2021. **8**(5): p. 431-436.
16. Kalbusch, A., Henning, E., Brikalski, M. P., de Luca, F. V., & Konrath, A. C. (). *Impact of coronavirus (COVID-19) spread-prevention actions on urban water consumption.* Resources, Conservation and Recycling, 2020. **163**: 105098.

17. Campos, M. A. S., Carvalho, S. L., Melo, S. K., et al.. *Impact of the COVID-19 pandemic on water consumption behaviour*. Water Supply, 2021. **21**(8): p. 4058-4067.
18. Nemati, M. *Covid-19 and urban water consumption.* Change, 2020. **40**(60): p. 9-11.
19. Lüdtke, D. U., Luetkemeier, R., Schneemann, M., & Liehr, S. *Increase in daily household water demand during the first wave of the covid-19 pandemic in Germany*. Water, 2021. **13**(3): p. 260.
20. Dzimińska, P., Drzewiecki, S., Ruman, M., Kosek, K., Mikołajewski, K., & Licznar, P. *The use of cluster analysis to evaluate the impact of COVID-19 pandemic on daily water demand patterns.* Sustainability, 2021. **13**(11): p. 5772.
21. Almulhim, A. I., & Aina, Y. A. *Understanding Household Water-Use Behavior and Consumption Patterns during COVID-19 Lockdown in Saudi Arabia*. Water, 2022. **14**(3): p. 314.
22. Ministry of Health, *COVID-19 information platform, general coronavirus chart*. [cited 2021 29 June]; Available from: https://covid19.saglik.gov.tr/TR-66935/genel-koronavirus-tablosu.html.
23. WHO, *Covid-19 dashboard*. [cited 2021 18 November]; Available from: https://covid19.tubitak.gov.tr/dunyada-durum
24. Ministry of Internal Affairs, *Covid-19 pandemic and Turkey*, [cited 2021 18 November]; Available from: https://www.icisleri.gov.tr/arem/covid-19-pandemisi-ve-turkiye
25. Kocaeli Water and Sewerage Administration. *The general information and data of DMA-08.* 2021. Technical Report.
26. TUIK. Address Based Population Registration System. [cited 2022 18 February]; Available from: https://biruni.tuik.gov.tr/medas/?kn=95&locale=tr
27. Wilcoxon, F. Individual comparisons by ranking methods. in Breakthroughs in statistics.1992. New York: Springer. p. 196-202.

.

Available online at www.dergipark.org.tr/en

INTERNATIONAL ADVANCED RESEARCHES and ENGINEERING JOURNAL

Journal homepage: www.dergipark.org.tr/en/pub/iarej

e-ISSN: 2618-575X

International Open Access

Volume 06
Issue 01

April, 2022

Research Article

Job shop scheduling with genetic algorithm-based hyperheuristic approach

Canan Hazal Akarsu [a,*] ***and Tarık Küçükdeniz*** [b]

[a] *Department of Industrial Engineering, Istanbul Esenyurt University, Istanbul, 34510, Turkey.*
[b] *Department of Industrial Engineering, Istanbul University – Cerrahpasa, Istanbul, 34320, Turkey.*

ARTICLE INFO

Article history:
Received 22 November 2021
Accepted 21 March 2022
Published 15 April 2022

Keywords:
Dispatching rules
GA-based hyperheuristics
Genetic algorithms
Hyperheuristics,
Job shop scheduling

ABSTRACT

Job shop scheduling problems are NP-hard problems that have been studied extensively in the literature as well as in real-life. Many factories all over the world produce worth millions of dollars with job shop type production systems. It is crucial to use effective production scheduling methods to reduce costs and increase productivity. Hyperheuristics are fast-implementing, low-cost, and powerful enough to deal with different problems effectively since they need limited problem-specific information. In this paper, a genetic algorithm-based hyperheuristic (GAHH) approach is proposed for job shop scheduling problems. Twenty-six dispatching rules are used as low-level heuristics. We use a set of benchmark problems from OR-Library to test the proposed algorithm. The performance of the proposed approach is compared with genetic algorithm, simulating annealing, particle swarm optimization and some of dispatching rules. Computational experiments show that the proposed genetic algorithm-based hyperheuristic approach finds optimal results or produces better solutions than compared methods.

1. Introduction

Job shop scheduling problem has been widespread and tough problem in literature that has been raised in recent 60 years [1]. There are many factories that make production worth millions of dollars with job shop type production system all around the world. It is really important to employ effective production scheduling methods in order to decrease costs and increase labor productivity and profitability [2]. The aim of this paper is to propose an effective GA-based hyperheuristic approach for JSSPs.

It has been accepted that the first studies, on which job shop scheduling was built, started in 1950s [3]. Johnson [4]'s algorithm, which was improved for double-machine flow type scheduling problem, was adapted to job shop scheduling problem by Jackson [5]. During 1950s, polynomial time algorithms directed towards the solution of the problem of job shop scheduling continued to be improved. The studies conducted in 1960s focused on reaching optimal result by using enumerative algorithms. Disjunctive graphs illustration was firstly proposed by Roy and Sussmann [6] in 1964 and the first disjunctive graph-based enumerative approach was implemented by Balas [7] in 1969. As well as being the most common enumerative approach, branch and bound algorithm's area of usage has been limited due to the fact that optimal solution can't be found for many problems. The complexity of problem has been the focal point of the studies during 1970s and the middle of 1980s. It has been discussed that only small parts of job shop scheduling problems could be solved with polynomial time algorithms and the majority of them belongs to NP-hard class. This situation has caused approximate solution methods to gain importance. Dispatching rules are the first approximate solution methods that have been improved. Between 1988 and 1991, innovative approximate solution methods [8] such as bottleneck algorithm and in 1990s, hybrid methods were developed [3]. While heuristic methods aim to produce appropriate solutions within reasonable calculation time, they don't guarantee optimal solution [9]. The reasons why the popularity of heuristic methods has increased since 1991 are the fact that their calculation power is strong and they have conversion features [10]. Dispatching rules, which are also called as priority rules or scheduling rules in literature, are the rules that are used for the solutions of scheduling problems because of its ease of implementation, quick reaction to sudden changes and production of valid solutions [11]. In literature, selection

* Corresponding author. Tel.: +90 444 9 123/1325; Fax: +90 212 699 09 90.
E-mail addresses: hazalakarsu@esenyurt.edu.tr *(C.H. Akarsu)*, tarik.kucukdeniz@gmail.com *(T. Küçükdeniz)*
ORCID: *0000-0003-1692-7727 (C.H. Akarsu), 0000-0002-6670-1809 (T. Küçükdeniz)*
DOI: 10.35860/iarej.1018604

of dispatching rules to be used is carried out with two methods: steady state simulation and artificial intelligence methods [11]. The selection of dispatching rules to be used within this study was provided by GA-based hyperheuristic approach.

Hyperheuristic approaches are high-level heuristics that look for a good solution instead of looking for a direct solution, by managing a series of low-level heuristics and they need limited problem-specific information [12]. The concept of hyperheuristic was first used to describe the protocol including the use of different artificial intelligence methods [13]. It was first described as "heuristics to choose heuristics" in accordance with combinatorial optimization as an independent concept in 2000 [14]. Burke et al. [13] divided hyperheuristics into two, according to the nature of heuristic search space. These are heuristic-selection that call for one of available low-level heuristics and heuristic-generation that form new heuristics by using available low-level heuristics [see 15–19]. Hyperheuristics can be classified depending on the type of low-level heuristics (LLHs) used as "construction" or "perturbation". Hyperheuristics that use dispatching rules as LLHs are included in construction class according to the structure of low-level heuristics. In this paper, GA-based hyperheuristic approach that is included in heuristic selection-construction class was proposed for job shop scheduling problems.

The aim of this paper is to propose an effective GA-based hyperheuristic approach for job shop scheduling problems. To the best of our knowledge, there are only few studies using GA-based hyperheuristic for the solution of the JSSP. This study is one of the few studies proposing a GA-based hyperheuristic for job shop scheduling problems. Other studies are given in Section 5. Unlike the few similar studies in the literature, 26 dispatching rules were used as low-level heuristics to provide an effective GA-based hyperheuristic approach for job shop scheduling problems.

2. Problem Statement

Job shop scheduling problem is described as qualifying starting time of each operation making objective function optimum by fulfilling precedence and capacity constraints specified in advance for performing *n* operations in *m* machines [20]. The number of possible schedules in JSSP is $(n!)^m$ for *m* machines and *n* operations [21]. In a study carried out by Lenstra and Rinnooy Kan [22], it was proved that JSSP was included in NP-hard class in case of availability of more than three machines. Relevant calculation time increases exponentially along with the increase in the size of the problem in order to obtain optimal solution for the problems that are included in NP-hard class. $J = \{J_1, J_2, \dots, J_n\}$ is the set of jobs and $M = \{M_1, M_2, \dots, M_m\}$ is the set of machines. It is accepted that each operation is performed only once in each machine. Processing of a job J_j in a machine M_i is called as an operation and the operation of a job is showed as O_{ij}. Each job follows special sequence of machines by technological constraints. Each job has its own sequence of machines and it is independent from the sequence of other jobs. Each O_{ij} operation has a special processing time and this time is shown as $p_{ij.}$ All processing times are known and fixed. Setup times and transfer times are integrated into processing times.

In scheduling problems, a large number of complicated and sometimes conflicting objective functions can be built. Mellor [23] listed 27 scheduling problem objective functions. Minimization of maximum completion time is the first objective function used by the researchers in 1950s. Its academic and industrial use is common due to the fact that its mathematical formulation is easy [3]. Mathematical formulation of general job shop scheduling problem, which its objective function is the minimization of maximum completion time is as follows [21]:

C_{max}: maximum completion time (makespan)

y_{ij}: starting time of job j on machine i

p_{ij}: processing time of job j on machine i

N: set of all operations (i,j) that must be performed on n jobs.

A: set of all precedence constraints $(i,j) \rightarrow (k,j)$ that require job j to be processed on machine i before it is processed on machine k

min C_{max}

subject to

$$y_{kj} - y_{ij} \geq p_{ij} \; for \; all \; (i,j) \rightarrow (k,j) \in A \quad (1)$$

$$C_{max} - y_{ij} \geq p_{ij} \; for \; all \; (i,j) \in N \quad (2)$$

$$y_{ij} - y_{il} \geq p_{il} \; or \; y_{il} - y_{ij} \geq p_{ij} \; for \; all \; (i,l),(i,j) \in N \quad (3)$$

$$y_{ij} \geq 0 \; for \; all \; (i,j) \in N \quad (4)$$

Constraints (1) ensure all precedence constraints $(i,j) \rightarrow (k,j)$ that require job j to be processed on machine i before it is processed on machine k. Constraints (2) ensure that maximum completion time is not exceeded. Constraints (3) ensure that an operation cannot be interrupted, once it begins. Constraints (4) ensure nonnegativitiy of decision variables y_{ij}.

3. The GA Metaheuristic

The genetic algorithm (GA) developed by Holland [24] is a general search strategy and optimization method especially used in combinatorial optimization problems [25]. Genetic algorithms are used in many fields such as engineering, computer science, economy administration and supply chain management [26]. GA approach for the solution of scheduling problems was first developed by Davis [27] for job shop scheduling problem. GA has several advantageous features in comparison with other metaheuristics [26]:

- Flexibility of identification of constraints and quality measures,
- The ability to work with continuous and discrete variables,
- Ability of comprehensive search space,
- The ability to provide multiple optimal or good solutions,
- Use of parallel calculation techniques to reduce processing time.

Contrary to local search methods which handle one feasible solution such as simulated annealing and tabu search, GA uses population of solutions during search in order to prevent early convergence to local minimum [25]. Each individual in the population is called as a chromosome. Each chromosome consists of genes and represents a feasible solution. Chromosomes are evaluated with the calculation of fitness values. Crossover and mutation operators are used to produce new generations. Produced new generations are called as offspring. After many produced generations, the population converges with a solution that can be local or global optimum [28]. Since the time it was first developed, there have been significant improvements in chromosome representation of GA [29-31], crossover operator [32], mutation operator [32, 33], selection operator [32, 34] and generation of an initial population [35]. These developments have made traditional GA stronger [26]. Cheung and Zhou [36] proposed genetic algorithm and heuristic rule-based hybrid approach for JSSP. It was concluded that heuristic increased the performance of GA. Wang and Zheng [37] proposed integrated use of GA and SA for job shop scheduling problem. Zhou, Feng and Han [38] proposed integrated use of genetic algorithm, neighborhood search algorithm and dispatching rules (SPT, MWKR). It was stated that proposed algorithm proved good solutions in comparison with neighborhood search algorithm, simulated annealing and traditional GA. Gao, Sun and Gen [39] proposed integrated use of GA and variable neighborhood search methods for multi-objective flexible job shop scheduling problems. Variable neighborhood algorithm was used in order to increase convergence speed of GA. Two-vector chromosome representation that consists of a machine assignment vector and a job order vector was used in GA. It was shown that proposed method produced equal or better results in 157 out of 181 benchmark instances with available methods. Dao, Abhary and Marian [26] made a bibliometric analysis of published genetic algorithm studies between 1972 and 2014.

4. Dispatching Rules

Dispatching rules are the rules that are developed to make a quick selection among appropriate operations to be assigned in each time to form the schedule [18]. Dispatching rules are classified as static and dynamic based on the time variable [11]. While static dispatching rules such as earliest due date (EDD) and shortest processing time (SPT) can make evaluations before scheduling starts, dynamic rules such as most total work remaining (MTWR) and first in first out (FIFO) make changeable evaluations in any iteration while forming schedule [18]. According to their structural features, dispatching rules are classified as simple dispatching rules, combined dispatching rules, weighted dispatching rules and heuristic dispatching rules. Simple dispatching rules such as SPT, EDD have a single parameter objective function [11]. Simple dispatching rules can optimize limited scheduling objective functions [18]. Combined dispatching rules that are formed with the use of several simple dispatching rules are more successful for the solution of complicated problems. Weighted dispatching rules are linear combination of simple dispatching rules in which specified weights are assigned to operations according to their importance. Heuristic dispatching rules such as expert knowledge are generally used with simple, combined and weighted dispatching rules based on the structure of the system [11]. As new dispatching rules can be formed with the combination of one or more available dispatching rules, they can also be formed with one or more heuristic rules and dispatching rules [40].

Dispatching rules are heuristic rules that are often used for the solution of scheduling problems with the ability of producing valid solutions in limited time and quick response to sudden changes. When scheduling literature is considered, it is clear that sequencing rules, scheduling rules, priority rules and dispatching rules are used to describe the same technique [11]. Panwalkar and Iskander [41] listed and classified more than 100 dispatching rules. Dispatching rules have been used and continued to be developed for more than fifty years [41]. Even though there are many studies on dispatching rules, the majority of new studies are about combination and modification of old dispatching rules [11].

5. GA-based Hyperheuristic Algorithm

Generally, development of a heuristic, based on a relevant problem, is time consuming and it requires detailed information of the field. Though it gives successful results for the problems for which they are developed, they can't be generalized to new or similar problems very often [42]. The motivation behind hyperheuristics is to expand application fields of developed methods. The studies carried out for this aim date back to the beginning of 1960s [13]. In early studies [see 43,44], when the concept of hyperheuristics wasn't used yet, producing better results was aimed by using different dispatching rules in iterations according to a specific order.

Apart from simple low-level heuristics, hyperheuristics don't require any problem-specific information. Each LLH communicates with high-level heuristic with an interface structure independent from the problem. Hyperheuristic can call a LLH to see what happens when a LLH is used. Called LLH sends various parameters in which we can observe the performance of LLH such as objective function value and computational time [14].

Indirect chromosome representation is used in genetic algorithm-based hyperheuristics using genetic algorithm as high-level heuristic. In indirect chromosome representation, each chromosome represents the way of forming a solution instead of the solution itself [12]. In traditional GA, while chromosome directly encodes a solution via binary arrays or permutations, early studies were about indirect chromosome encoding as a result of difficulty of direct encoding due to the complicated nature of real-life problem [12]. Fang, Ross and Corne [45] is one of the first publications in which indirect chromosome representation is used. Eight dispatching rules were used as low-level heuristics for the solution of open shop scheduling problem. Each chromosome consists of a pair of gene sequences. In each pair, the first gene represents a dispatching rule and the second gene represents the job to be assigned with the implementation of this dispatching rule. It was seen that obtained results were very close to available solution in the literature; in fact, they were sometimes better.

To the best of our knowledge, there are only few studies using GA-based hyperheuristic for the solution of the JSSP. This study is one of the few studies proposing a GA-based hyperheuristic for job shop scheduling problems. Unlike the few similar studies in the literature, 26 dispatching rules were used as low-level heuristics in our study. Other studies are [43], [46] and [47]. Dorndorf and Pesch [43] used GA-based approach specifying sequence of LLHs to minimize makespan in JSSP. As low-level heuristics, twelve dispatching rules were used. One chromosome includes $n-1$ genes for n operations and each gene represents the heuristic to be used for scheduling an operation. Norenkov and Goodman [46] developed heuristic combination method for JSSPs. Scheduling problem was divided into two main problems as sequencing of jobs and their assignment to servers and heuristics were designated for each sub-problem. The aim of the method is to find optimal implementation order of heuristics. In its dimension, each chromosome is represented by a matrix of size $n \times q$ where n is the number of jobs and q is the number of consecutive service stages in which each job experiences during its processing. The schedule is formed for each service stage by adding a job in each stage. Vázquez-Rodríguez and Petrovic [47] developed hyperheuristic approach called as Dispatching Rule-Based GA for the solution of multiobjective JSSP. Genetic algorithm works in the space of dispatching rules and the chromosome representing the solution is expressed through (h, p) binary notation where h is the sequence of dispatching rules and p is the number of consecutive calls of each dispatching rule. The results of the approach were found to be superior when they were compared with GA using permutation chromosome representation and hyperheuristic using dispatching rule-based chromosome representation.

GA-based hyperheuristics are also used for other scheduling problems in [48-50]. Hart, Ross and Nelson [48] proposed GA-based approach for scheduling of chicken catching crew with the aim of sending chickens according to the orders received in chicken breeding facility, which is a real-life problem. A chromosome representation consisting of four parts was used. In the first part, there is a fixed problem specific criterion for narrowing the search space. In the second part, the information of the order sequence is included. In the third part, there is a heuristic dividing orders into duties and in the fourth part, there is a heuristic assigning the duties to the crew members. As a result of the study, it was observed that proposed method produced schedules within minutes competed with the schedules prepared by experts in days. For the trainer scheduling problem, Cowling, Kendall and Han [49] developed a GAHH approach called as hyper-GA. Working as a high-level heuristic, genetic algorithm specifies implementation sequence of LLHs into the problem. Twelve problem-specific heuristics were used as LLHs. In a chromosome, each gene was expressed through an integer value representing a LLH and the chromosome specifies implementation sequence of low-level heuristics. It was shown that proposed approach gave better results than the individual results of low-level heuristics and genetic algorithm. Bacha *et al.* [50] proposed a GA-based hyperheuristic approach for permutation flow shop problems. Authors used genetic algorithms as LLHs and also as a high-level heuristic. Each chromosome consisted of 10 genes and each gene includes a genetic operator or a parameter such as population size, number of generations, selection method, crossover method, crossover probability etc. The high-level heuristic was also a genetic algorithm which aim was to produce a tailored genetic algorithm to permutation flow shop scheduling problems. Since the effectiveness of GA depends on the selection of genetic operators and parameters, high-level GA calibrates low-level genetic algorithms. Authors indicated that there is definitely a correlation between benchmark instances and the appropriate GA parameters/operators that solve them efficiently. In the literature, GA-based hyperheuristic algorithms are also applied to different problems such as one-dimensional bin-packing problem [51], design of the packaging process of two-dimensional rectangular blocks

[52], multitask-oriented manufacturing service composition [53] and parameter tuning [54].

6. The Proposed GA-Based Hyperheuristic Algorithm

In this study, a genetic algorithm-based hyperheuristic approach is proposed for job shop scheduling problems. Proposed hyperheuristic approach is expressed through two modules: hyperheuristic module and low-level heuristics module. With a domain barrier, hyperheuristic module works independently from the problem. Hyperheuristics don't need to know problem-specific information or the names and methodologies of LLHs. LLHs are the heuristics directly working in the solution space of the problem. Therefore, LLHs module can be seen as a black box that hides problem details from the hyperheuristic and sends only objective function value of the current schedule to the hyperheuristic module.

6.1 Low-Level Heuristics Module

LLHs are the heuristics making a search in the solution space of the problem and requiring problem-specific information. In this paper, 26 dispatching rules shown in Table 1 were used as low-level heuristics. Dispatching rules were selected due to their success in scheduling problems, ease of implementation and flexibility [47]. The adaptation of developed approach to the changes in the problem can be easily provided by adding or removing new dispatching rules without changing the structure of the hyperheuristic.

The terminology below was used for the formulation of dispatching rules [55]:

C_{ij} : completion time of operation j of job i

$N_{ij}(t)$: number of jobs waiting in the queue containing operation j of job i at time t

p_{ij} : processing time of operation j of job i

q : index of unassigned operations ($q = j, \dots, m_i$)

X_{ij} : random number between 0 and 1 assigned to operation j of job i

$Y_{ij}(t)$: total work of jobs waiting in the queue containing operation j of job i at time t

$Z_i(t)$: priority value of job i at time t. Smallest values have greatest priority.

In traditional scheduling algorithm one dispatching rule is selected initially and assignments of all operations are performed according to this rule. In the proposed method, at each decision (assignment) point, the same or a different dispatching rule specified by the hyperheuristic is applied. Our developed scheduling algorithm is as follows:

1st step: Select the first unassigned operation according to job routing of each job and specify their machines. The precedence constraints of operations are satisfied in this step.

2nd step: Select the machine that becomes idle earliest among the machines.

3rd step: Assign the operation to selected machine according to the dispatching rule in k^{th} gene of the chromosome specified by the hyperheuristic ($k = 1$ in the first decision point).

4th step: Update schedule matrix. Update $k = k + 1$.

5th step: If all the operations are assigned, go to 6th step. Otherwise, go to 1st step.

6th step: Calculate objective function value of the schedule and send it to the hyperheuristic module.

6.2 Hyperheuristic Module

Hyperheuristic module is the part where the strategy of selecting the most appropriate heuristic to be called from LLH set is built in order to make the assignment at decision points of the problem. Steps of developed GA-based hyperheuristic module are as follows:

1st step: Create a population consisting of candidate solutions (each of them is called as a chromosome).

2nd step: Sent the population to LLH module.

3rd step: Select the chromosomes giving better results in accordance with objective function values returning from LLH module for the next population.

4th step: Create a new population from selected chromosomes with crossover and mutation operators.

5th step: Send the new population to LLH module again and take objective function values from LLH module.

6th step: If termination condition is not satisfied, go to the 3rd step. Otherwise, go to the 7th step.

7th step: Accept the chromosome giving the best objective function value so far as optimal result.

One of the factors specifying the quality of the solution is the method of encoding to chromosome. Cheng, Gen, & Tsujimura [56] stated that there were two main coding approaches of chromosome representation for job shop scheduling problems: direct encoding approach and indirect encoding approach. While in direct encoding approach, the schedule that is the direct solution of the problem is encoded onto the chromosome, in indirect encoding approach, for example in dispatching rule-based chromosome representation, implementation sequence of dispatching rules into the problem are encoded to the chromosome. In this paper, real valued dispatching rule-based chromosome representation is used. In dispatching rule-based representation, dispatching rules are matched with the numbers starting from 1 to the number of dispatching rules and candidate solution is created as a sequence of these numbers of size $m \times n$, where m is the number of machines and n is the number of jobs

Table 1. Low-level heuristics

DR	**Description** Selects the job which has…	$Z_i(t)$
RANDOM	the smallest value of random priority	X_{ij}
FIFO	arrived at machine queue first	$C_{i,j-1}$
LIFO	arrived at machine queue last	$-C_{i,j-1}$
SPT	the shortest processing time (Also used as tie-breaking rule)	p_{ij}
LPT	the longest processing time	$-p_{ij}$
STPT	the shortest total processing time	$\sum_{j=1}^{m_i} p_{ij}$
LTPT	the longest total processing time	$-\sum_{j=1}^{m_i} p_{ij}$
LTWR	the least total work remaining	$\sum_{q=j}^{m_i} p_{iq}$
MTWR	the most total work remaining	$-\sum_{q=j}^{m_i} p_{iq}$
SDT	the smallest ratio of $(processing\ time \div total\ processing\ time)$	$p_{ij}/\sum_{j=1}^{m_i} p_{ij}$
LDT	the largest ratio of $(processing\ time \div total\ processing\ time)$	$-(p_{ij}/\sum_{j=1}^{m_i} p_{ij})$
SDR	the smallest ratio of $(processing\ time \div total\ remaining\ processing\ time)$	$p_{ij}/\sum_{q=j}^{m_i} p_{iq}$
LDR	the largest ratio of $(processing\ time \div total\ remaining\ processing\ time)$	$-(p_{ij}/\sum_{q=j}^{m_i} p_{iq})$
SMT	the smallest value of $(processing\ time \times total\ processing\ time)$	$p_{ij} \times \sum_{j=1}^{m_i} p_{ij}$
LMT	the largest value of $(processing\ time \times total\ processing\ time)$	$-(p_{ij} \times \sum_{j=1}^{m_i} p_{ij})$
SMR	the smallest value of $(processing\ time \times total\ remaining\ processing\ time)$	$p_{ij} \times \sum_{q=j}^{m_i} p_{iq}$
LMR	the largest value of $(processing\ time \times total\ remaining\ processing\ time)$	$-(p_{ij} \times \sum_{q=j}^{m_i} p_{iq})$
FRO	the fewest number of remaining operations	$m_i - j + 1$
LRO	the largest number of remaining operations	$-(m_i - j + 1)$
AVPRO_1	the shortest average processing time [59].	$\sum_{j=1}^{m_i} p_{ij}/m_i$
AVPRO_2	the longest average processing time [59]	$-(\sum_{j=1}^{m_i} \frac{p_{ij}}{m_i})$
SIO	shortest imminent operation [40].	$p_{i,j+1}$
WINQ	the least total work in the queue of its next operation	$Y_{i,j+1}(t)$
NINQ	the least number of jobs in the queue of its next operation	$N_{i,j+1}(t)$
PT+WINQ	the smallest value of $(processing\ time +$ total work in the queue of its next operation)[59].	$p_{ij} + Y_{i,j+1}(t)$
2PT+WINQ+NPT	the smallest value of $(2 \times processing\ time +$ total work in the queue of its next operation $+$ $processing\ time\ of\ next\ operation)$[60].	$2 \times p_{ij} + Y_{i,j+1}(t) + p_{i,j+1}$

In real valued representation, dispatching rules used as LLHs are represented by the number intervals between 0 and 1 instead of integers. A candidate solution consists of $m \times n$ unit of value, which is between 0 and 1. A low-level heuristic can be repeated more than once in a candidate solution.

An illustration of chromosome representation for a problem of size (2×4) is shown in Figure 1. Four low-level heuristics (h_1, h_2, h_3, h_4) were used and their intervals were defined by a minimum and a maximum value making selection probability of all low-level heuristics equal (25%). Each gene in the chromosome carries a random value. Each LLH falls into its specific discrete probability range and values in the chromosome are used to transform the chromosome representation to the LLH representation by using these discrete probability ranges. When the chromosome is decoded, the sequence of LLHs called by hyperheuristic respectively at each decision point is also given in Figure 1. It is seen that the solution obtained from hyperheuristic shows the way to be followed in order to reach optimal solution instead of direct solution of the scheduling problem.In this study, 26 low-level heuristics were used and their intervals were defined in order to make selection probability of all low-level heuristics equal. Until all operations were assigned, low-level heuristics encoded in the chromosome are called by hyperheuristic respectively at each decision point and an operation is assigned to the selected machine. Initial population is generated randomly. Uniform distribution is used as probability distribution function for creating the first population in real valued encoding.

Chromosome Representation	0.552	0.068	0.745	0.98	0.015	0.383	0.014	0.997
Sequence of low-level heuristics	h_3	h_1	h_3	h_4	h_1	h_2	h_1	h_4

Figure 1. Illustration of chromosome representation

Table 2. Average makespan of selected problems on benchmarked algorithms

Benchmark Instances	Optimum	Metaheuristics			Hyper-heuristic	Dispatching Rules				
		GA	SA	PSO	GAHH	SPT	MTWR	SIO	FIFO	PT+WINQ
FT06	55	56.96	56.20	57.96	55	84	58	69	74	74
LA01	666	672.43	666.76	677.56	666	817	828	867	912	912
LA06	926	926.13	926.00	926.00	926	1205	971	1199	1082	1082
LA11	1222	1226.26	1222	1225.76	1222	1537	1268	1453	1299	1299
LA19	842	939.63	899.06	942.50	876.93	1011	1000	1160	919	1028.7
ORB01	1059	1239.06	1173.26	1250.43	1085.46	1266	1374	1466	1327	1327
ABZ7	656	910.80	798.36	864.90	732.7	818	788	969	859	859
SWV11	2983	4920.83	4267.46	4745.23	3584.06	3712	4382	4232	4224	3923

In order to create a new population, some chromosomes coming from previous population should be selected to the new population as parent chromosomes. There are different methods in order to decide which chromosomes to choose. These methods are divided into two classes as fitness proportionate selection and ordinal selection [57]. In this study, roulette wheel selection, known as the most common proportional selection method, is used. In roulette wheel selection, roulette wheel slots are assigned to each individual proportional to its fitness value. Good solutions have more slots and therefore more probability of being selected. Roulette wheel selection steps are as follows [57]:

1st step: Calculate the fitness value (f_i) of each individual in the population.

2nd step: Calculate the probability of being selected (slot size) for each individual in the population: $p_i = \frac{f_i}{\sum_{j=1}^{n} f_j}$.

3rd step: Calculate the cumulative probability for each individual: $q_i = \sum_{j=1}^{n} p_j$.

4th step: Generate a uniform random number, $r \in (0,1]$.

5th step: If $r < q_1$ then select first chromosome (x_1), otherwise select chromosome x_i such that $q_{i-1} < r \leq q_i$.

6th step: Repeat *4th* and *5th* steps n times.

7. Computational Analysis

The performance of proposed GA-based hyperheuristic approach was evaluated by comparing with some metaheuristics and dispatching rules on a set of benchmark instances obtained from OR-Library [58]: FT06 (6×6), LA01 (10×5), LA06 (15×5), LA11 (20×5), LA19 (10×10), ORB1 (10×10), ABZ7 (20×15), SWV11 (50×10). The methods that were compared are GA, SA, PSO and SPT, MTWR, SIO, FIFO, PT + WINQ dispatching rules that were found to be successful in the literature for minimization of makespan in job shop problems.

In this paper, parallel GA and parallel GA-based hyperheuristic were used. Though genetic algorithms are more resistant against premature convergence to local optimum according to other local search methods, they aren't completely immune. One of proposed methods for reducing premature convergence of GA is parallelization of the GA into disjoint subpopulations. Parallel GA helps reducing computational time due to the use of parallel processors [25]. The code of proposed GAHH method was written in MATLAB. Population size, crossover rate and mutation rate parameter values for GA and GA-based hyperheuristic were used as 100, 0.7 and 0.1, respectively. The proposed GA-based hyperheuristic approach, GA, SA and PSO were run 30 times with 1000 iterations in each run. Average results are given in Table 2. The proposed GAHH approach gave optimal results for FT06, LA01, LA06 and LA11 instances and gave better results than the benchmark methods on the other instances. The best results for each run are given in Table 3. Also, boxplots of the 30 runs on each dataset can be seen in Figure 2. As an example, Gantt chart representing the optimal schedule to the FT06 instance is shown in Figure 3.

Table 3. Best values achieved among all the runs for each benchmarked algorithm

Benchmark Instances	Optimum	Metaheuristics			Hyper-heuristic	Dispatching Rules				
		GA	SA	PSO	GAHH	SPT	MTWR	SIO	FIFO	PT+WINQ
FT06	55	55	55	55	55	84	58	69	74	74
LA01	666	666	666	666	666	817	828	867	912	912
LA06	926	926	926	926	926	1205	971	1199	1082	1082
LA11	1222	1222	1222	1222	1222	1537	1268	1453	1299	1299
LA19	842	895	875	889	867	1011	1000	1160	919	1028.7
ORB01	1059	1171	1100	1183	1078	1266	1374	1466	1327	1327
ABZ7	656	857	767	820	723	818	788	969	859	859
SWV11	2983	4570	4128	4430	3513	3712	4382	4232	4224	3923

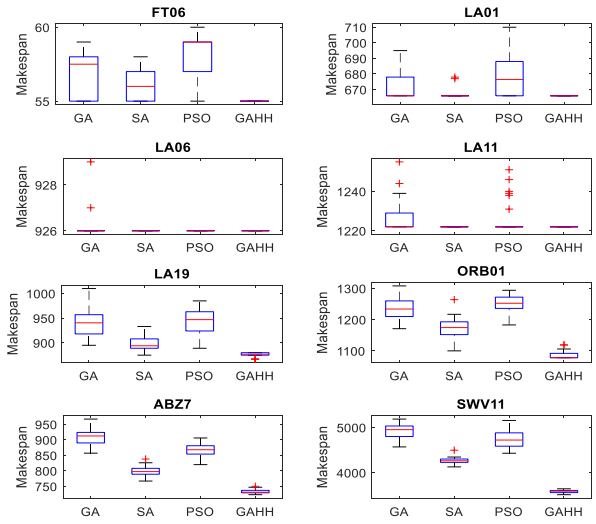

Figure 2. Boxplots of the 30 runs on each dataset

When average running results are considered, the proposed GA-based hyperheuristic approach gives the optimal results in 4 instances and produces better results than GA, SA, PSO, SPT, MTWR, SIO, FIFO, PT+WINQ in LA19 by 6.67%, 2.46%, 6.96%, 13.26%, 12.31%, 24.4, 4.58%, 14.75% respectively; in ORB01 by 12.4%, 7.48%, 13.19%, 14.26%, 21%, 25.96%, 18.2%, 18.2% respectively; in ABZ07 by 19.55%, 8.23%, 15.29%, 10.43%, 7.02%, 24.39%, 14.7%, 14.7% respectively; in SWV11 by 27.17%, 16.01%, 24.47%, 3.45%, 18.21%, 15.31%, 15.15%, 8.64% respectively.

When best running results are considered, the proposed GA-based hyperheuristic approach produces better results than GA, SA, PSO, SPT, MTWR, SIO, FIFO, PT+WINQ in LA19 by 3.13%, 0.91%, 2.48%, 14.24%, 13.3%, 25.26, 5.66%, 15.72% respectively; in ORB01 by 7.94%, 2%, 8.88%, 14.85%, 21.54%, 26.47%, 18.76%, 18.76% respectively; in ABZ07 by 15.64%, 5.74%, 11.83%, 11.61%, 8.25%, 25.39%, 15.83%, 15.83% respectively; in SWV11 by 23.13%, 14.9%, 20.7%, 5.36%, 19.83%, 16.99%, 16.83%, 10.45% respectively.

8. Conclusions

In today's highly competitive production environment, developing effective production scheduling methods has become a requirement for surviving in the market and maintaining competition. Increasing profitability is possible by increasing productivity in production and decreasing the costs by using effective scheduling methods. For this aim, a genetic algorithm-based hyperheuristic approach for job shop scheduling problem is proposed in this paper. The hyperheuristic approach is based on selection of the most appropriate heuristic from simple heuristics set which are called as low-level heuristics embedded under the hyperheuristic in order to make assignments at decision points of the problem. Since hyperheuristic approach doesn't need any problem-specific information except low-level heuristics.

In this paper, 26 dispatching rules were used as low-level heuristics. Dispatching rules were chosen due to their success, ease of implementation and flexibility in scheduling problems. The performance of proposed GA-based hyperheuristic approach was evaluated by comparing with GA, SA, PSO and SPT, MTWR, SIO, FIFO, PT + WINQ dispatching rules that were found to be successful in the literature for minimization of makespan in job shop scheduling problems. Eight benchmark instances in different sizes from different data sets were obtained from OR-Library. Computational experiments showed that the proposed GAHH approach has reached to the optimal solution in 4 out of 8 benchmark instances and was superior than the GA, SA, PSO and dispatching rules on the other instances. Computational results showed that proposed GAHH approach is an effective and promising method for JSSPs. We can further improve GAHH by combining a learning mechanism such as reinforcement learning. Reinforcement learning can avoid premature convergence and escape local optimum for 4 benchmark instances. Furthermore, we can test our proposed GAHH approach on different sets of benchmark instances and compare their results to the best methods in the state of art.

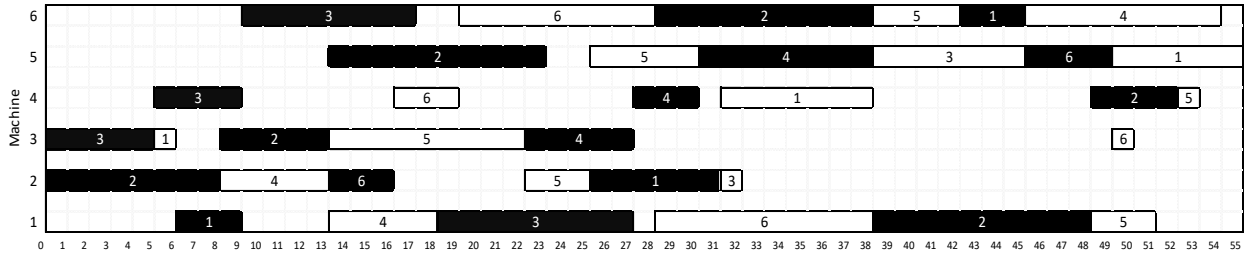

Figure 2. Gantt chart of optimal schedule for FT06

Declaration

The authors declared no potential conflicts of interest with respect to the research, authorship, and/or publication of this article. The authors also declared that this article is original, was prepared in accordance with international publication and research ethics, and ethical committee permission or any special permission is not required.

Author Contributions

C.H. Akarsu developed the methodology, performed the analysis and wrote the original draft. T. Küçükdeniz developed the methodology, supervised and improved the study.

Nomenclature

GAHH : Genetic algorithm-based hyperheuristic
GA : Genetic algorithm
SA : Simulated annealing
PSO : Particle swarm optimization
EDD : Earliest due date
SPT : Shortest processing time
MTWR : Most total work remaining
FIFO : First in first out
JSSP : Job shop scheduling problem
LLH : Low-level heuristic

References

1. Potts, C. N. and V. A. Strusevich, *Fifty years of scheduling : a survey of milestones*. J. Oper. Res. Soc., 2009. **60**(1): p. 41–68.
2. Jones, A., L. C. Rabelo, and A. T. Sharawi, *Survey of job shop scheduling techniques*, in *Wiley encyclopedia of electrical and electronics engineering*, 1999, Wiley Online Library.
3. Jain, A. S. and S. Meeran, *Deterministic job-shop scheduling: Past, present and future*. Eur. J. Oper. Res., 1999. **113**(2): p. 390–434.
4. Johnson, S., *Optimal two- and three-stage production schedules with setup times included*. Nav. Res. Logist. Q., 1954. **1**: p. 61–68.
5. Jackson, J., *An extension of Johnson's result on job-lot scheduling.* Nav. Res. Logist. Q., 1956. **3**(3): p. 201–204.
6. Roy, B. and B. Sussmann, *Les problemes d'ordonnancement avec contraintes disjonctives*. Note ds, 1964. **9**.
7. Balas, E., *Machine scheduling via disjunctive graphs: An implicit enumeration algorithm*. Oper. Res.,1969. **17**: p. 941–957.
8. Kovalev, M. Y., et al., *Approximation scheduling algorithms: A survey.* Optimization, 1989. **20**(6): p. 859–878.
9. Sharma, P. and A. Jain, *A review on job shop scheduling with setup times.* Proc. Inst. Mech. Eng. Part B J. Eng. Manuf., 2016. **230**(3): p. 517–533.
10. Jones, D. F., S. K. Mirrazavi, and M. Tamiz, *Multi-objective meta-heuristics: An overview of the current state-of-the-art.* Eur. J. Oper. Res., 2002. **137**(1): p. 1–9.
11. Fan, H. L., et al., *Survey of the selection and evaluation for dispatching rules in dynamic job shop scheduling problem*, in *2015 Chinese Automation Congress (CAC)*, 2015. p. 1926–193.
12. Chakhlevitch, K. and P. *Cowling, Hyperheuristics: Recent developments* in *Adaptive and Multilevel Metaheuristics*, 2008, Springer. p. 3–29.
13. Burke, E. K., et al., *A classification of hyper-heuristic approaches*, in *Handbook of Metaheuristics*, 2010, Springer. p. 449–468.
14. Cowling, P., G. Kendall, and E. Soubeiga, *A hyper heuristic approach to scheduling a sales summit*, in *International conference on the practice and theory of automated timetabling*, 2020. p.176-190.
15. Hunt, R., M. Johnston, and M. Zhang, *Evolving machine-specific dispatching rules for a two-machine job shop using genetic programming*, in *2014 IEEE Congress on Evolutionary Computation (CEC)*, 2014. p. 618–625.
16. Nguyen, S., et al., *Automatic design of scheduling policies for dynamic multi-objective job shop scheduling via cooperative coevolution genetic programming*. IEEE Trans. Evol. Comput., 2014. **18**(2): p. 193–208.
17. Sim, K. and E. Hart, *A novel heuristic generator for JSSP using a tree-based representation of dispatching rules*, in *Proceedings of the Companion Publication of the 2015 Annual Conference on Genetic and Evolutionary Computation*, 2015. p. 1485–1486.
18. Hart, E. and K. Sim, *A hyper-heuristic ensemble method for static job-shop scheduling.* Evol. Comput., 2016. **24**(4): p. 609–635.
19. Branke, J., et al., *Automated design of production scheduling heuristics: A review.* IEEE Trans. Evol. Comput., 2016. **20**(1): p. 110–124.
20. Yenisey, M. M. and M. Şevkli, *Atölye tipi çizelgeleme problemleri için parçacık sürü optimizasyonu yöntemi*. İTÜDERGİSİ/d, 2006. **5**(2): p. 58–68.
21. Pinedo, M. L., *Scheduling: Theory, algorithms and systems*. 2008, New Jersey: Prentice-Hall.
22. Lenstra, J. K. and A. R. Kan, *Computational complexity of discrete optimization problems.* Ann. Discret. Math., 1979. **4**: p. 121–140.
23. Mellor, P., *A Review of Job Shop Scheduling*. J. Oper. Res. Soc., 1966. **17**(2): p. 161–171.
24. Holland, J. H., *Adaptation in natural and artificial systems: an introductory analysis with application to biology, control, and artificial intelligence*. 1975, Ann Arbor (MI):

The University of Michigan Press.

25. Park, B. J., H. R. Choi, and H. S. Kim, *A hybrid genetic algorithm for the job shop scheduling problems.* Comput. Ind. Eng., 2003. **45**(4): p. 597–613.
26. Dao, S. D., K. Abhary, and R. Marian, *A bibliometric analysis of Genetic Algorithms throughout the history*. Comput. Ind. Eng., 2017. **110**: p. 395–403.
27. Davis, L., *Job shop scheduling with genetic algorithms*, in *Proceedings of an international conference on genetic algorithms and their applications*, 1985.
28. Gen, M. and R. Cheng, *Genetic algorithms and engineering optimization*. 2000, John Wiley & Sons.
29. Zhong, T. X. and J. C. Chen, *A hybrid-coded genetic algorithm based optimisation of non-productive paths in CNC machining*. Int. J. Adv. Manuf. Technol., 2002. **20**(3): p. 163–168.
30. Wang, Y. M., H. L. Yin, and J. Wang, *Genetic algorithm with new encoding scheme for job shop scheduling*. Int. J. Adv. Manuf. Technol., 2009. **44**(9–10): p. 977–984.
31. Dao, S. D., K. Abhary, and R. Marian, *Optimisation of partner selection and collaborative transportation scheduling in virtual enterprises using GA.* Expert Syst. Appl., 2014. **41**(15): p. 6701–6717.
32. Qing-dao-er-ji, R. and Y. Wang, *A new hybrid genetic algorithm for job shop scheduling problem.* Comput. Oper. Res., 2012. **39**(10): p. 2291–2299.
33. Tang, P.-H. and M.-H. Tseng, *Adaptive directed mutation for real-coded genetic algorithms.* Appl. Soft Comput., 2013. **13**(1): p. 600–614.
34. Wu, X., et al., *A genetic algorithm for cellular manufacturing design and layout.* Eur. J. Oper. Res., 2007. **181**(1): p. 156–167.
35. Šetinc, M., M. Gradišar, and L. Tomat, *Optimization of a highway project planning using a modified genetic algorithm.* Optimization, 2015. **64**(3): p. 687–707.
36. Cheung, W. and H. Zhou, *Using genetic algorithms and heuristics for job shop scheduling with sequence-dependent setup times.* Ann. Oper. Res., 2001. **107**(1–4): p. 65–81.
37. Wang, L. and D. Zheng, *An effective hybrid optimization strategy for job-shop scheduling problems.* Comput. Oper. Res., 2001. **28**(6): p. 585–596.
38. Zhou, H., Y. Feng, and L. Han, *The hybrid heuristic genetic algorithm for job shop scheduling.* Comput. Ind. Eng., 2001. **40**(3): p. 191–200.
39. Gao, J., L. Sun, and M. Gen, *A hybrid genetic and variable neighborhood descent algorithm for flexible job shop scheduling problems.* Comput. Oper. Res., 2008. **35**(9): p. 2892–2907.
40. Gere, W. S., *Heuristics in job shop scheduling*. Manage. Sci., 1966. **13**(3): p. 167–190.
41. Panwalkar, S. S. and W. Iskander, *A survey of scheduling rules.* Oper. Res., 1977. **25**(1): p. 45–61.
42. Burke, E. et al., *Hyper-heuristics: a survey of the state of the art.* J. Oper. Res. Soc., 2013. **64**(12): p. 1695–1724.
43. Dorndorf, U. and E. Pesch, *Evolution based learning in a job shop scheduling environment.* Comput. Oper. Res., 1995. **22**(1): p. 25–40.
44. Hart, E. and P. Ross, *A heuristic combination method for solving job-shop scheduling problems*, in *International Conference on Parallel Problem Solving from Nature*, 1998. p. 845–854.
45. Fang, H., P. Ross, and D. Corne, *A promising hybrid GA/heuristic approach for open-shop scheduling problems*, in *Proceedings of 11th European Conference on Artificial Intelligence*, 1994. p. 590–594.
46. Norenkov, I. P. and E. D. Goodman, *Solving scheduling problems via evolutionary methods for rule sequence optimization*, in *Soft computing in engineering design and manufacturing*, 1998, Springer. p. 350–355.
47. Vázquez-Rodríguez, J. A. and S. Petrovic, *A new dispatching rule based genetic algorithm for the multi-objective job shop problem.* J. Heuristics, 2010. **16**(6): p. 771–793.
48. Hart, E., P. Ross, and J. A. D. Nelson, *Scheduling chicken catching – An investigation into the success of a genetic algorithm on a real-world scheduling problem.* Ann. Oper. Res., 1999. **92**: p. 363–380.
49. Cowling, P., G. Kendall, and L. Han, *An investigation of a hyperheuristic genetic algorithm applied to a trainer scheduling problem*, in *the IEEE Congress on Evolutionary Computation (IEEE CEC02)*, 2002.
50. Ahmed Bacha, S. Z., et al., A *New Hyper-Heuristic to Generate Effective Instance GA for the Permutation Flow Shop Problem.* Procedia Comput. Sci., 2019. **159**: p. 1365–1374.
51. Ross, P., et al., *Learning a procedure that can solve hard bin-packing problems: A new ga-based approach to hyper-heuristics*, in *Genetic and Evolutionary Computation Conference*, 2003. p. 1295–1306.
52. Thomas, J. and N. S. Chaudhari, *Design of efficient packing system using genetic algorithm based on hyper heuristic approach.* Adv. Eng. Softw., 2014. **73**: p. 45–52.
53. Zhang, S., Y. Xu, and W. Zhang, *Multitask-oriented manufacturing service composition in an uncertain environment using a hyper-heuristic algorithm.* J. Manuf. Syst., 2021. **60**: p. 138–151.
54. Pang, L. M., H. Ishibuchi, and K. Shang, *Using a Genetic Algorithm-based Hyper-heuristic to Tune MOEA/D for a Set of Various Test Problems*, in *IEEE Congress on Evolutionary Computation (CEC)*, 2021. p. 1486–1494.
55. Haupt, R., *A survey of priority rule-based scheduling.* OR Spectr., 1989. **11**(1): p. 3–16.
56. Cheng, R., M. Gen, and Y. Tsujimura, *A tutorial survey of job-shop scheduling problems using genetic algorithms—I. representation.* Comput. Ind. Eng., 1996. **30**(4): p. 983–997.
57. Sastry, K., D. E. Goldberg, and G. Kendall, *Genetic algorithms*, in *Search methodologies*, 2005, Springer. p. 97–125.
58. Beasley, J. E., *OR-Library*, 1990. [cited 2017 20 Nov]; Available from: http://people.brunel.ac.uk/~mastjjb/jeb/orlib/jobshopinfo.html.
59. Jayamohan, M. S. and C. Rajendran, *New dispatching rules for shop scheduling : A step forward.* Int. J. Prod. Res., 2000. **38**(3): p. 563–586.
60. Rajendran, C. and O. Holthaus, *Efficient jobshop dispatching rules: Further developments*. Prod. Plan. Control Manag. Oper., 2000. **11**(2): p. 171–178.

Available online at www.dergipark.org.tr/en

INTERNATIONAL ADVANCED RESEARCHES and ENGINEERING JOURNAL

Journal homepage: www.dergipark.org.tr/en/pub/iarej

e-ISSN: 2618-575X

International Open Access

Volume 06
Issue 01

April, 2022

Research Article

Effect of pattern on air permeability, mechanical resistance and thickness of wovens

Hayriye Hale Aygün [a,*]

[a]*University of Kahramanmaras Sutcu Imam, Department of Design, 46060, Turkey*

ARTICLE INFO

Article history:
Received 20 September 2021
Accepted 24 January 2022
Published 15 April 2022

Keywords:
Abrasion resistance
Air permeability
Bi-directionally tensile strength
Cotton yarns
Weave pattern
Woven fabric

ABSTRACT

This study examines the effect of different patterns on aesthetic properties, air permeability characteristics and mechanical performance of woven fabrics constructed with 100% cotton ring spun yarns. Weaving process were proceeded by using 28/2 Ne combed warp and 32/2 Ne carded weft yarns with identical manufacturing parameters. Fabrics with 5 dissimilar patterns were obtained and 5 measurements were done for each pattern type. Average yarn floats, crimp percentage and yarn settings were calculated and fabric thickness, abrasion resistance, air permeability and bi-directionally tensile strengths of these fabrics were tested. Test results showed that increasing the numbers of floating yarns made fabric more air-permeable but less resistant against to applied mechanical forces. Besides, it caused to increase in fabric thickness. All test results were statistically evaluated by ANOVA and Duncan comparison tests and it was seen that the effect of weave pattern was at significance level of $p<0.001$. Air permeability characteristics of wovens can be easily and inexpensively arranged by pattern effect. In order to satisfy mechanical and functional specifications, further studies should be performed on panama woven structures with different yarn floats.

1. Introduction

Designing is the process of preparing end product to meet functional and visual demands by considering basic criterias. By means of fabric designing, raw material selection and appropriate manufacturing parameters have crucial effect in order to handle sufficient performance of desired functional, visual and mechanical responce. Mechanics of textile fabrics are strictly depending on basic traditional route but further steps are different as comparing engineering fabric design with artistic one. In engineering fabric design, woven fabrics differentiate from other fabric types due to controllable manufacturing conditions on unit area of fabric structure during fabric weaving [1].

Cotton-based fabrics are mostly used textile surfaces in clothing industry due to their very good breathable characteristics and they present wide range of end products for summer and winter clothing by being manufactured with different surface manufacturing techniques [2]. In order to handle attractive apperance and extend lifetime of cotton-based garments, selecting of suitable pattern has crucial importance and preferred pattern can be given by different manufactuing methods such as knitting, braiding and weaving. Individual controlling of structural yarns in 2-D woven fabrics, namely warp and weft, makes possible to manufacture various fabrics easily with different characteristics. Because variability on controlling of individual yarns determines the number of total floats or interlacements which are related with weave pattern. Thereby, it can be possible to present wide range of fabrics having different characteristics either in fabric length, width or both [3].

As well as aesthetic properties of a woven fabric to be used in clothing industry, it is important to focus on its mechanical specifications. While putting on a garment or wearing it on daily use, it is exposed to various forces. In order to prolong garments' life, both structural and mechnical specifications should be considered in a whole as trying to reach aesthetic performance [4]. By appropriate pattern effect, woven fabrics can easily satisfy the required demands such as thermal [5], visual [6], textural [7] and mechanical [8,9] performances. In woven fabrics, pattern effect and structural components are responsible from the occurence of interyarn coincidence which determines resistance characteristics of fabric structure [10-14] and interyarn pores which determines air permability characteristics [14-18].

* Corresponding author. Tel.: *+90 344 300 24 66*; Fax: +09 344 300 25 02.
E-mail addresses: hsolak@ksu.edu.tr *(H. H. Aygün)*
ORCID: 0000-0002-2812-8079
DOI: 10.35860/iarej.997843

There are many researches about the effects of basic fabric patterns, their derivatives (with less floating yarns such as 2/1 or 3/1 twill) and yarn structure either on air permeability or abrasion resistance of woven fabrics but not both of them. Besides, tensile behaviors of these patterns are not examined bi-directionally which garments are exposed to these forces as being dressed by users. In this study, woven fabrics with different patterns having long yarn floats were manufactured by using 100% cotton weft and warp yarns. Bi-directionally tensile strength, air permeability and abrasion resistance of various wovens were tested and thickness of samples were measured. Structural properties of fabrics were also calculated by corresponding formula. Obtained test results were correlated with corresponding fabric pattern.

2. Experimental Study

2.1 Materials

Unsized warp yarns and weft yarns were used for manufacturing of woven fabrics with various patterns. Specifications of warp and weft yarns are given in Table 1.

2.2 Methods

Fabrics used in this study were woven by CCI Evergreen Loom with a weaving width of 20 inch and reed width was 110/2. Woven fabrics were grey in color and directly tested without any further applications. Structural views of five woven fabrics are illustrated in Figure 1.

2.3 Characterization

Determination of structural parameters of woven fabrics: Due to the difference in fabric design and different number of yarn floats in patterns, structural parameters for each pattern should be calculated and clarified. For this reson, yarn diameters, crimp percentage, yarn settings and fabric weights were determined and associated with other test results.

Measurement of fabric thickness: Thickness of woven fabrics were tested with R&B Cloth Thickness Tester by considering TS 7128 EN ISO 5084 standard. The test was performed by taking measurements on five different surface areas of each sample.

Abrasion resistance test: The abrasion resistances of wovens were tested by Martindale Abrasion Tester according to yarn breakage method of ASTM D4157-02 standard (Figure 2(a)). Test was performed by increasing abrasing head rate (rpm) at certain intervals unless two yarn breakages were observed for each sample and abrasion resistance characteristics of samples were evaluated according to circle numbers [19].

Testing of air permeability: Measurements of air permeability of woven samples were performed by Prowhite Air Permeability Instrument according to TS 391 EN ISO 9237 standard as shown in Figure 2 (b). By applying 100 Pa air pressure onto 20 cm^2 area of samples, 5 measurements for each sample were taken from different areas of fabrics and average test results were calculated.

Bi-directionally tensile strength testing: Tensile strengths were tested by Instron 4411 testing device according to ASTM D1682 strip method. Five measurements were done for each pattern and average test results were considered for evaluating tensile behaviors of samples on corresponding direction.

In this study, it is reported that how weave pattern alters structural properties and affects thickness, air permeability characteristic and resistance of fabrics against to tensile and abrassive forces. Despite of many researches on fabric pattern, this paper differentiates from its counterparts via weaves with long yarn floats, testing mechanical and aesthetic properties of 2-D fabrics woven with folded yarns and determining structural properties of fabrics theoretically. Significance of test results were interpreted by ANOVA and Duncan comparison test.

Table 1. Properties of yarns used for weaving fabric

	Warp	Weft
Raw material	Cotton	Cotton
Spinning method	Combed ring	Carded ring
Count (Ne)	32/2	28/2
Twist (T/m)	778	648
Strength (Rkm)	28.32	17.57
U (%)	8.59	7.41
CV_m (%)	11.01	9.36
Fiber length (mm)	29	29
Fiber fineness (μ)	4.4	4.4

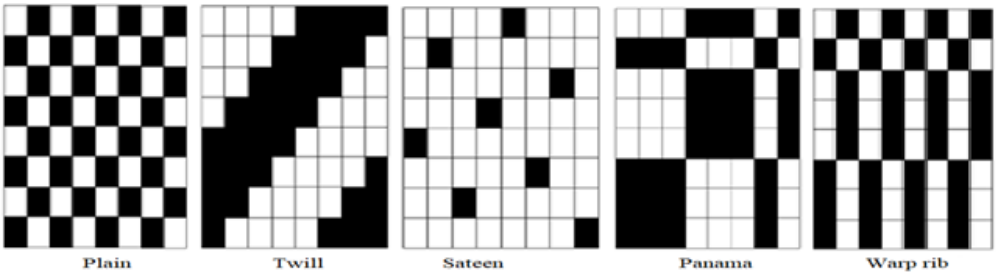

Figure 1. Structural views of wovens P $\frac{1}{1}$, T $\frac{4}{4}$, S $\frac{1}{7}$ (3), Pa $\frac{3}{3}\ \frac{1}{1}$, W_R $\frac{3}{3}\ \frac{1}{1}$

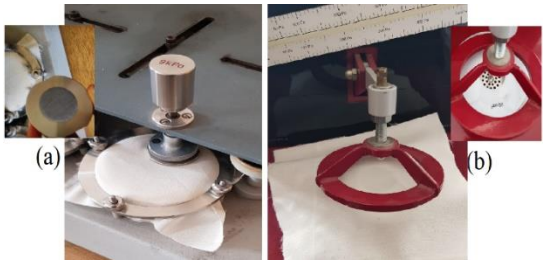

Figure 2. Testing of samples (a) abrasion resistance test (b) air permeability test

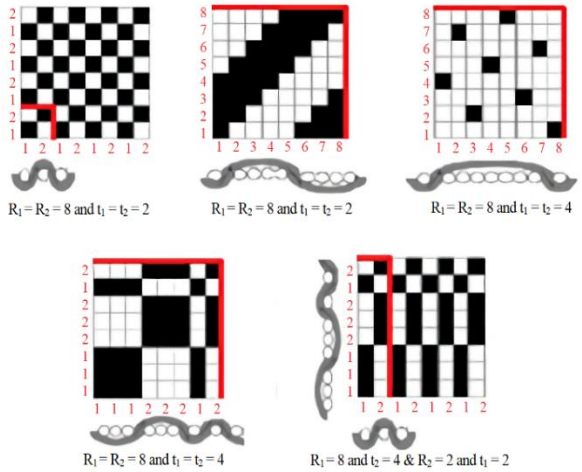

Figure 3. Weave repeats and interlacing points of patterns

3. Results and Discussion

3.1 Determination of Structural Properties of Wovens

In Figure 1, it is seen that warp and weft yarns intersect each other at right angles. But yarn length between two consecutive yarns in same direction differs due to pattern effect so average yarn floats for patterns and other structural properties for fabrics should be determined. Average yarn floats for warp and weft yarns were calculated according to Ashenhurst theory by the following formula [20]:

$$F_{1,2} = \frac{R_{2,1}}{t_{1,2}} \quad (1)$$

Where *F* is yarn float, *R* is no of yarn in repeat, *t* is no of point in interlacing, subscripts *1* and *2* refer to warp and weft, respectively.

Weave repeats are square weaves for all woven patterns but not for warp rib. This means that yarn interlacing is similar for warp and weft direction in fabrics with square weave repeats but different in fabric with warp rib pattern [20]. Yarn interlacing and weave repeats for patterns are illustrated in Figure 3.

According to Brierly's theory, yarn setting on loom depends on yarn properties and pattern type used for weaving. Brierly stated that yarn settings affected from yarn count, constant obtained from yarn type and yarn count system, average float length and weave constant. For woven fabrics with different yarn counts in warp and weft direction, yarn setting can be calculated from the following formula [21]:

$$S = \sqrt{K \times N_{ave}} \times F^{m} \quad (2)$$

$$N_{ave} = 2 \times \left[\frac{N_{warp} \times N_{weft}}{N_{warp} + N_{weft}}\right] \quad (3)$$

Where *S* is yarn sett/inch, *K* is constant based on yarn count and yarn type (200 for cotton yarn, 134 for worsted yarn, 61 for woolen yarn), N_{ave} is average yarn count in indirect system (N_e), *F* is average yarn float, *m* is weave constant (0.45 for plain and panama, 0.39 for twill, 0.42 for sateen, 0.42 for warp rib (take 0.42 for short and long float weaves and add +7-8% to result) [21,22].

Yarn diameters of warp and weft yarns were calculated from the formula [23,24]:

$$d_{1,2} = \frac{a}{\sqrt{N_{1,2}}} \quad (4)$$

Where *d* is yarn diameter, *a* is yarn correction factor (0.95 for cotton yarns), *N* is yarn count in indirect system (N_m), subscripts *1* and *2* refer to warp and weft, respectively.

Yarn crimp and weave angle for warp and weft yarns were also calculated from the following formula [25]:

$$Cos\ \theta_{1,2} = \frac{d_{1,2}}{d_1 + d_2} \quad (5)$$

$$Cos\ \theta_1 + Cos\ \theta_2 = 1 \quad (6)$$

Crimp percentage for warp and weft yarns can be calculated from the following formula [25]: All structural properties determined for fabrics with different weave patterns are given in Table 2.

$$C_{1,2} = \left[\frac{\pi\,(d_1 + d_2)}{180\sqrt{{d_{2,1}}^2 + 2 \times d_1 \times d_2}} \times Cos^{-1}\frac{d_{1,2}}{d_1 + d_2} - 1\right] \Big/ F_{1,2} \quad (7)$$

3.*2 Measurement of Sample Thickness*

Interlacing of warp and weft yarns caused a change in fabric thickness due to individual crossectional height of each yarn and various number of intersecting point on differently woven fabrics. According to the results, the highest (0.0085 mm) and lowest (0.0050 mm) fabric thickness were measured in sateen and plain woven fabrics, respectively. In Figure 4, it is seen that thickness of samples woven with derivatives of plain weave have also thinner fabric thickness and thickness increases by increasing yarn floats. During weaving process, weft and warp yarns intersect each other and this case limits the crossectional area of each yarn in intersection points. Interlacing number is directly related with weave pattern and thickness values are not identical in fabrics woven with same yarns. Increase in intersecting points among yarns causes thinner fabric manufacturing [26-28]. Additionally fabric thickness is affected from warp and weft sett in unilayer and multilayer fabrics. In this study, unilayer fabrics are woven and fiber type of yarns are identical but yarn counts are different from each other and yarn setts are variable for different weave patterns. Due to the intent of comparing fabric pattern effect on fabric thickness and wide range of difference on quantitative thickness values, it is resulted that weave pattern

has a considerable effect on unilayer fabric thickness and yarn setting variation on fabrics.

3.3 Air permeability test

Air permeability is quantitative characteristic of a porous surface through which air passes. Volume of air passing through these fabrics was measured as approximately 150 dm^3/min. Mohammed [29] states that air permeability of sateen woven fabric is higher than those of hopsack and kautshok woven fabrics due to higher yarn floats and lower cross-over point on sateen. In this study, the longest yarn floats were observed in sateen woven fabrics both on warp and weft directions. In twill and panama woven fabrics, yarn floats were more than those of plain woven fabrics. This case clearifies the difference on air permeability that it is strongly related with yarn float variations by considering the patterns used in this study.

It was seen that air volume passing through plain fabric was 30 dm^3/min although constituting yarns of plain weave had the highest yarn intersection. In some studies, it is reported that air permeability is mainly dependent upon the textile fabric's weight and construction [30,31]. By changing the sequence of yarn floats and number of interlacings, air permeability of textile surfaces can be differed. Size, arrangement and shape of the pores are decisive parameters on permeability characteristics of a fabric [19]. Umar et. al. [32] reported that longer yarn floats were resulted from less interlacements and air permeability of fabric was developed by increasing yarn float. Plain woven fabrics were found too dense to be a permeable fabric. In our study, plain woven fabrics have poor air permeability and previous studies support this result. Figure 5 demostrates that sateen fabric is the most air-permeable sample.

It was observed that air permeability was highest in the sateen weave due to less interlacements. In contrast to this fact, plain woven fabrics were the least permeable fabrics in which warp and weft yarns intersected each other densely. This case is supported by Kullmann [33]. Kullman claimed that sateen woven fabrics were more sensitive to air pressure, they tend to elongate much more than other wovens so weave pattern had crucial effect on air permeability characteristics of fabric. Due to longer yarn floats and less interlacements in sateen weave, volume of air passing through the voids of yarns was measured higher than other wovens had. Air permeability decreased by diverging pattern from sateen to plain weave and fabrics woven with inter-patterns such as, twill and warp rib, had medium air permeability characteristics. Şekerden [34] studied that air permeability was higher in the fabrics woven with blended weft yarns having at least 70% cellulosic fiber and the effect of weave type on air permeability was lower than that of the fibre proportion if cellulosic fibre content was less than 70%. Below these values, air permeability was lower in the fabrics woven with sateen and twill weaves and fibre content and type in blended yarns had highly crucial effect on air permeability characteristic of woven than weave pattern. But in this study, unblended 100% cotton yarns with different yarn counts were used for weaving differently-patterned fabrics. Taştan et. al. [17] reported that increase in yarn twist improved air permeability characteristic. In this paper, fabrics were woven with 32/2 Ne combed warp yarns and 28/2 Ne carded weft yarns and dominant effect of pattern on air permeability was easily observed by using inexpensive weft yarn usage. Because giving more twist to yarns or combing process lead to increase in cost. Besides, long yarn floats result to low yarn consumption due to less crimp effect. So it can be resulted that air permability of woven fabrics can be inexpensively controlled by pattern affect with eliminating some spinning mill processes and giving less twist.

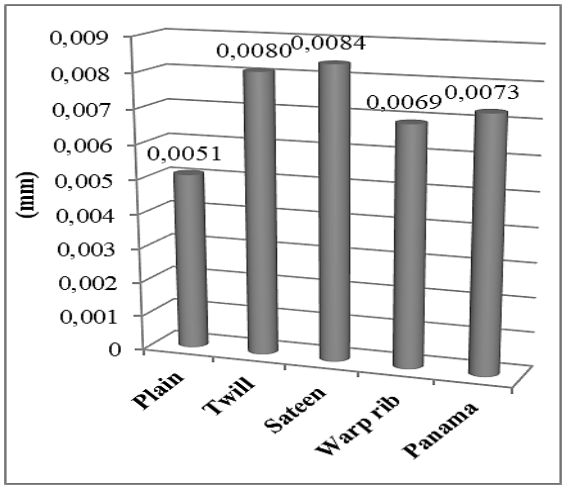

Figure 4. Average sample thickness according to patterns

Table 2. Structural properties of woven fabrics

Weave pattern		Yarn dia.	Ave. floats	Yarn / cm	Crimp (%)	Fabric weight (g/m^2)	Fabric thickness (mm)
Plain	Warp	0.182	1	22	0.21	192.95	0.0051
	Weft	0.195	1	22	0.20		
Twill	Warp	0.182	4	38	0.052	307.05	0.0080
	Weft	0.195	4	36	0.05		
Sateen	Warp	0.182	4	40	0.052	319.25	0.0084
	Weft	0.195	4	37	0.05		
Panama	Warp	0.182	2	30	0.105	252.32	0.0069
	Weft	0.195	2	28	0.10		
Warp rib	Warp	0.182	2	32	0.105	246.98	0.0073
	Weft	0.195	1	23	0.20		

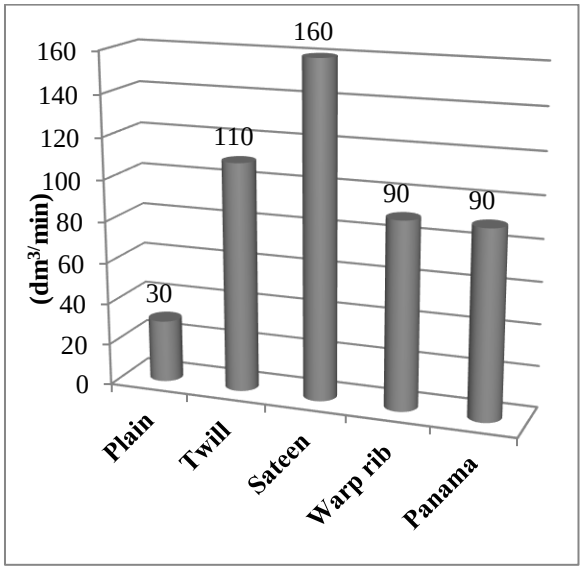

Figure 5. Air permeability test results of wovens

3.4 Abrasion resistance of samples

Abrasion resistance can be defined as the capacity to absorb stress energy occuring by a series of repeated rubbing. Figure 6 shows cycling number on which the woven samples are abrased. Plain and plain-derivated woven fabrics were found as more resistant to abrasion. Fan and Hunter [35] stated that fabrics resisted flat abrasive forces if a decrease was observable in yarn floats and an increase were available in tightness, thickness and weight of fabric. Sateen and twill fabrics woven from ring-spun or wrap-spun cotton yarns had slightly lower flex abrasion resistance than that of plain woven. Sateen or twill samples woven from yarns with same linear density, crimp and equal sett in warp and weft direction were found as more resistant to flat abrasion. In this study, fabrics were woven from 2-folded ring-spun cotton yarn and yarn setts were close to each other in sateen and twill wovens thereby it was not seen a slight difference on resistance of sateen and twill wovens. Plain wovens again had high flat abrasion resistance and results were supported by study of Fan and Hunter.

The least abrasion resistance among samples was observed in sateen woven fabrics and two yarn breakage was occured after 9800 cycle of abrasive head. Kaynak and Topalbekiroğlu [36] reported that long yarn float and less interlacement facilitated yarn lose due to easier movement of yarns by rubbing and increase in cycle caused more yarn lose in different woven fabrics. More resistant fabric to abrasion forces could be manufactured by abrading abrassive load over a greater number of fibres while preventing fibre removal from fabric.

3.5 Bidirectionally tensile strength testing of samples

Deteorations due to tensile stress were not same for all types of woven fabrics. Previous studies resulted that tensile strength of a fabric was not only related with characteristics of constituents yarns but also structure of fabric and tensile strength testing method [37-39]. According to the obtained test results of strip test method, plain-woven fabris were the most resistant to tensile forces with 106.4 MPa along warp direction. Besides fabrics woven with derivative patterns of plain weave such as panama and warp rib, had higher tensile strength values than those of sateen and twill woven fabrics. Ferdousa et al. (2014) stated that tensile behavior of a fabric was based on the weave pattern and low breaking strength was resulted from too much larger floats and too firmest interlacement [40]. In this study, warp and weft setts were variable on loom state for all weave types and this difference can be expressed as weave pattern has great importance on tensile strength behavior of structure than yarn sett. The lowest tensile resistance was tested on sateen woven fabrics which had the highest yarn setts and were found as most air permeable. The inverse relationship between tensile strength and air permability behaviors of a woven is glared as it is previously stated in literature reviews [41].

Fabrics having high degree of intersecting point elongate at break point more than other wovens. This case can be obviously seen by comparing panama and warp rib-woven fabrics. Although they are derivatives of plain weave, there is a clear elongation difference due to various numbers of intersecting point they have. Elongation at break due to forces applied along warp direction is related with density of weave and cloth setting [1]. Woven samples behaved differently against to tensile stresses along warp and weft directions. In Figure 7, it was shown that the highest tensile strengths were measured in fabric widths of warp rib- and sateen-woven fabrics, respectively. Some studies reported that tensile strength of plain woven fabrics were higher than that of twill wovens with same yarn settings and strength along weft direction could be developed by increasing weft sett [42, 43].

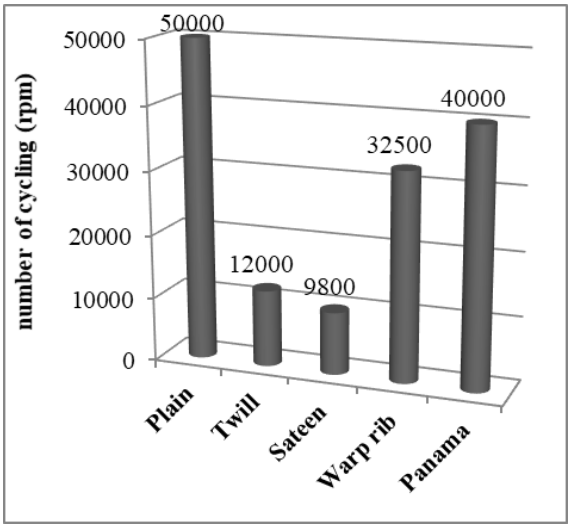

Figure 6. Number of cycling at which two yarn breakages observed

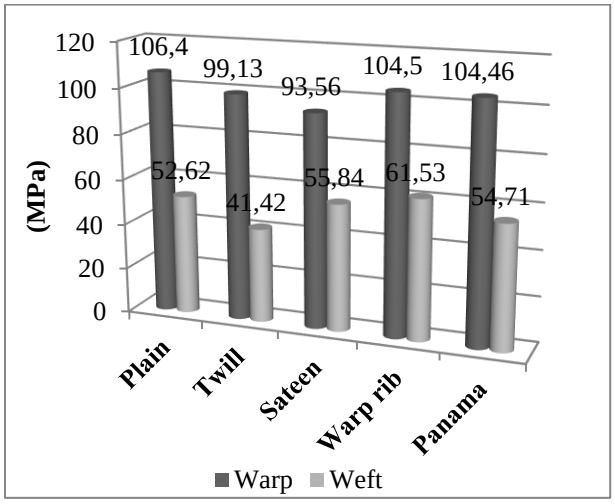

Figure 7. Ultimate tensile strength of wovens

Tensile strengths of plain woven fabrics along weft and warp directions were found as 52.62 MPa and 106.40 MPa, respectively. Due to balanced interlacing in plain weave, resistance to tensile loading on both directions were found higher than other weaves. But in sateen wovens, less number of interlacing point between yarns caused that weft yarns were exposed to resist tensile loading much more than interlacing forces. This case can be seen in derivatives with less yarn interlacements of basic patterns and high tensile resistance along weft direction can be observed in sateen weave [44]. Although long yarn floats of sateen wovens, tensile strength on weft direction compated with other wovens. In this study, warp and weft settings were variable and count of weft yarn was higher and twist on weft yarns were lower than those of warp yarns. Due to these reasons, resistance to tensile stress along weft direction was found lower and elongations at break for differently-patterned wovens were higher along warp direction but not along weft direction. Kurtça (2001) reported that lineer relationship was available between breaking and tensile strength of textile woven fabrics and breaking strength was basically dependent upon weave pattern and yarn characteristics. As increasing yarn count of weft yarn, both tensile and breaking strength decreased along fabric width, namely weft direction [45]. Although low tensile strength of sateen woven fabric along weft direction, percent elongation at break of weft yarns were close to other wovens had. It is seen that tensile properties of wovens are affected by weave pattern of fabric because components, namely yarns, are same for all fabrics with different weave patterns. On the other hand, the degree of yarn twist affects fabric elongation [1,45]. Reduction in twist improves cover and elongation but decreases yarn strength. Thereby, elongation and tensile strength properties of all samples along weft direction are poorer than those of warp direction. Figure 8 illustrates percentage strain of samples at breaking point.

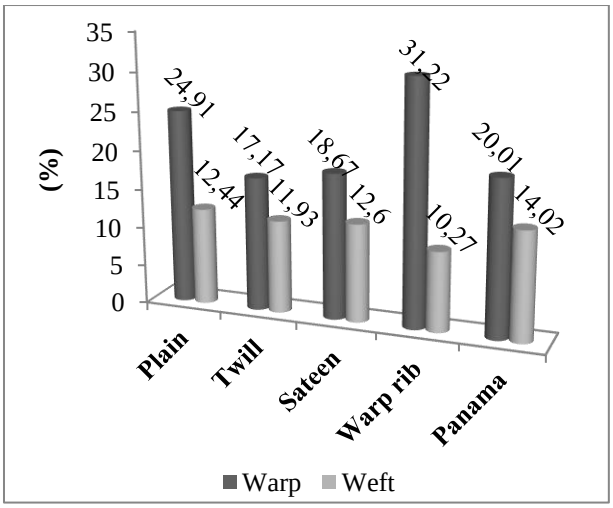

Figure 8. Tensile strain at break

Table 3. Statistical analysis of the effect of weave pattern on fabric properties

Pattern	Thickness	Air permeability	Abrasion resistance	Tensile Strength		Tensile Strain	
				Warp	Weft	Warp	Weft
Plain $\left(P\ \frac{1}{1}\right)$	0,0050^{a} (0,00008)	30,0020^{a} (0,01483)	50010^{e} (736,036)	106,4^{c} (1,2159)	52,60^{b} (0,8215)	24,91^{d} (0,6337)	12,44^{b} (0,2318)
Twill $\left(BT\ \frac{4}{4}\right)$	0,0080^{c} (0,00008)	107,62^{c} (4,3188)	120000^{b} (842,614)	99,13^{b} (1,1145)	41,42^{a} (0,7318)	17,17^{a} (0,2325)	11,93^{b} (0,3606)
Sateen $\left(S\ \frac{1}{7}\ (3)\right)$	0,0085^{d} (0,00005)	157,008^{d} (4,1875)	9810^{a} (888,397)	93,562^{a} (1,0417)	55,84^{c} (1,2461)	18,67^{b} (1,1450)	12,60^{b} (1,2000)
Warp rib $\left(R\ \frac{3\ 1}{3\ 1}\right)$	0,0069^{b} (0,00011)	86,530^{b} (4,1760)	32540^{c} (2055,298)	104,5^{c} (1,7944)	61,53^{d} (0,6213)	31,22^{e} (1,5952)	10,27^{a} (0,3126)
Panama $\left(P\ \frac{3\ 1}{3\ 1}\right)$	0,0070^{b} (0,00018)	85,220^{b} (4,1365)	40010^{d} (1895,850)	104,46^{c} (3,2160)	54,71^{c} (1,7961)	20,008^{c} (0,6866)	14,02^{c} (0,3435)
Sign.	p<0,001	p<0,001	p<0,001	p<0,001	p<0,001	p<0,001	p<0,001

Groups and significance of different weave patterns and also effects of these patterns on tested properties were statically interpreted by one-way ANOVA and Duncan comparison tests. All test results were found as statistically important with significance level of $p<0.001$ [36,46]. Despite of low standard deviation of warp rib, panama showed better distribution by means of homogenity. Warp rib and panama exhibited similar behaviors from the points of thickness, air permability and tensile strength along warp directions. Among all weave patterns, the highest standard deviation was determined in sateen weave for all tested parameters. Results of statistical analysis are given in Table 3.

4. Conclusions

Due to the inter-yarn pores available on inner and outer surfaces of fabric, possibility of variable numbers of yarn interlacement and controlling properties of structural components, woven fabrics have widespread usage either in clothing and other technical areas. By the way, woven fabrics take attentions of both artistic and engineering fabric designers. Because it makes possible to manufacture surfaces with demanded specifications for intended use. However, woven fabrics can exhibit variable mechanical and visual characteristics due to too many controllable parameters during weaving such as structural, operational or further process parameters.

In this study, the effect of fabric pattern on mechanical properties, permeability performances and thickness of woven fabrics are investigated and structural properties of fabrics are determined. Fiber type, yarn spinning method, reed width and fabric manufacturing technology were identical for all samples. Plain wovens were found as thinner, more resistant on warp direction and less air-permeable than those of other fabrics due to well-packaged yarn construction with high interlacement. Panama and warp rib which are derivatives of plain weave, exhibited similar characteristics but elongation at break was higher in warp rib fabric due to balanced long yarn floats. On the other hand, sateen fabric were more air permeable but thicker and less resistant against abrasive and tensile forces. Test results shows that panama woven fabrics which have average yarn setts among other fabrics can satisfy demands for mechanical, physical, structural and functional specifications.

Declaration

The author declared that no potential conflicts of interest with respect to the research, authorship and publication of this article. The author also declared that this article is original, was prepared in accordance with international publication and research ethics, and ethical committee permission or any special permission is not required.

Author Contributions

H.H. Aygün developed the methodology, improved the study, reported/illustrated the obtained test results and concluded the studied work.

Acknowledgement

The author would like to thank to Marteks Inc. Co. for yarn suppliement.

References

1. Gandhi, K. *Woven textiles: principles, technologies and applications.* 2012, England: Woodhead.
2. Khanzada, H., M. Khan and S. Kayani, *Cotton based clothing. In: Wang H., Memon H. (eds) Cotton science and processing technology*. 2020, Singapore: Springer.
3. Uddin, F. *Introductory Chapter: Textile Manufacturing Processes*. 2019, Croatia: InTechopen.
4. Clegg, A., W. Yu, J. Tan, C.K. Liu and G. Turk, *Learning to dress: Synthesizing human dressing motion via deep reinforcement learning.* ACM Transactions on Graphics. 2018. **37**(6): p. 1-10.
5. Asayesh, A., M. Talaei and M. Maroufi, *The effect of weave pattern on the thermal properties of woven fabrics*, International Journal of Clothing Science and Technology, 2018. **30**(4): p. 525-535.
6. Hussain, M.A.I., B. Khan, Z. Wang and S. Ding, *Woven fabric pattern recognition and classification based on deep convolutional neural networks*, Electronics, 2020. **9**: p. 1-12
7. Jing, J., M. Xu, P. Li, Q. Li and S. Liu, *Automatic classification of woven fabric structure based on texture feature and PNN*. Fibers and Polymers, 2014. **15**: p. 1092–1098.
8. Cao, J., R. Akkerman, P. Boisse, J. Chen, H. S. Cheng and E. F. de Graaf, *Characterization of mechanical behavior of woven fabrics: Experimental methods and benchmark results*, Composites Part A: Applied Science and Manufacturing, 2008. **39**(6): p. 1037-1053.
9. Jahan, I. *Effect of fabric structure on the mechanical properties of woven fabrics.* Advanced Research in Textile Engineering. 2017. **2**(2): p. 1-4.
10. Hossain, M.M., E. Datta and S. Rahman, *A review on different factors of woven fabrics' strength prediction*. Science Research, 2016. **4**(3): p. 88-97.
11. Turukmane, R. and R. Patil, *Structural behavior of fabric design on mechanical properties of woven fabrics.* Melliand International, 2019. **25**(1): p. 83-85.
12. Azeem M., Z. Ahmad, J. Wiener, A. Fraz, H.F. Siddique and A. Havalka, *Influence of weave design and yarn types on mechanical and surface properties of woven fabric.* Fibres & Textiles in Eastern Europe, 2018. **127**(1): p. 42-45.
13. Sardag, S. *Investigation of mechanical properties of fabrics woven with tencel/ cotton blend yarns.* Textile and Apparel, 2019. **29**(2): p. 162-170.
14. Havlova, M. *Air permeability and constructional parameters of woven fabrics*. Fibres & Textiles in Eastern Europe, 2013. **21-2**(98): p. 84-89.
15. Sarıoglu, E. And O. Babaarslan, *Porosity and air permeability relationship of denim fabrics produced using core-spun yarns with different filament finenesses for filling.* Journal of Engineered Fibers and Fabrics, 2019. **14**(1): p. 1-8.

16. Ceven, E.K. and G. Karakan Günaydın, *Investigation of some mechanical and air permeability properties of shirting fabrics produced from compact yarns made of natural and synthetic fibres.* Uludağ University Journal of The Faculty of Engineering, 2019. **24**(2): p. 445-460.
17. Tastan, E., M. Akgun, A. Gurarda, and S. Omeroglu, *Investigation of the effect of different structural parameters of cotton woven fabrics on their air permeability*. IOP Conference Series: Materials Science and Engineering, 2017. **254**: p. 1-4.
18. Ozgen, B. and S. Altas, *Evaluation of air permeability of fabrics woven with slub yarns*. Tekstil ve Konfeksiyon, 2017. **27**(2): p. 126-130.
19. Nielson K.J., *Interior textiles: fabrics, application, and historic style.* 2007, USA: Wiley&Sons.
20. Ozdemir, H., B.M. Icten and A. Doğan, *Experimental investigation of the tensile and impact properties of twill and twill derivative woven fabric reinforced composites.* Tekstil ve Konfeksiyon, 2018. **28**(4): p. 258-272.
21. Turhan, Y. and R. Eren, *Dokunabilirlik sınırıyla ilgili deneysel çalışmaların değerlendirilmesi.* Pamukkale Mühendislik Bilimleri Dergisi, 2005. **11**(2): p. 205-218.
22. Galuszynski, S., *Structure and tightness of woven fabrics.* Indian Journal of Textile Research, 1987. **12**: p. 71-77.
23. Kim, H.A. And S.J. Kim, *Simulation of the weave structural design of synthetic woven fabrics.* Fibers and Polymers, 2010. **11**(6): p. 905-910.
24. Dobrik Dubrovski, P., *Woven fabric engineering*. 2010, Croatia: Books on Demand.
25. Ebrahem, H.A.A., *Single woven fabric characterization in terms of yarn diameter and average float: Theoretical considerations and test results.* Mansoura Engineering Journal, 2009. **43**(2): p. 24-32.
26. Sekerden, F., *PES/VİS/LYCRA® içerikli atkı elastan dokumalarda çeşitli dokuma faktörlerinin kumaşın fiziksel ve mekanik özelliklerine etkisinin incelenmesi, in: Textile Engineering2009,* Çukurova University: Turkey. p.193.
27. Sirkova, B.K., *Description of fabric thickness and roughness on the basis of fabric structure parameters,* AUTEX Research Journal, 2012. **12**(2): p. 40-43.
28. Cherif, C., *Textile materials for lightweight constructions: technologies-methods-materials-properties*, 2015, Germany: Springer-Verlag Berlin Heidelberg.
29. Mohammad, G.A. *Comparative study of air permeability of polyester/metallic blended woven fabrics*. Life Science Journal, 2015. **12**(6): p. 78-82.
30. Abou-Nassif, G.A., *Predicting the tensile and air permeability properties of woven fabrics using artificial neural network and linear regression models.* Journal of Textile Science and Engineering, 2015. **5**(5): p. 209-215.
31. Ogulata, R.T., *Air permeability of woven fabrics.* Journal of textile and apparel, technology and Management, 2006. **5**(2): p. 1-10.
32. Umair, M., T. Hussain, K. Shaker, Y. Nawab, M. Maqsood and M. Jabbar, *Effect of woven fabric structure on the air permeability and moisture management properties*. The Journal of The Textile Institute, 2016. **107**(5): p. 596-605.
33. Kullman, R.M.H., C.O. Graham and G.F. Ruppenicker, *Air permeability of fabrics made from unique and conventional yarns. Textile Research Journal*, 1981. **51:** p. 781-786.
34. Sekerden F., *Effect of fabric weave and weft types on the characteristics of bamboo/cotton woven fabrics.* Fibres & Textiles in Eastern Europe, 2011. **19-6** (89): p. 47-52.
35. Fan, J. and L. Hunter, *Engineering apparel fabrics and garments*. 2009, USA: CRC Press.
36. Kaynak, H.K. and M. Topalbekiroglu, *Influence of fabric pattern on the abrasion resistance property of woven fabrics.* Fibres & Textiles in Eastern Europe, 2008. **16**(1): p. 54-56.
37. Kawabata, S., M. Niwa and H. Kawai, *The finite-deformation theory of plain-weave fabrics part- I: the biaxial-deformation theory.* Journal of Textile Institution, 1973. **64**(1): p. 21-26.
38. Realff, M.L., M.C. Boyce and S. Backer, *A micromechanical model of the tensile behavior of woven fabric.* Textile Research Journal, 1997. **67**(6): p. 445-459.
39. Wu, J. and N. Pan, *Grab and strip tensile strengths for woven fabrics: an experimental verification.* Textile Research Journal, 2005. **75**(11): p. 789–796.
40. Ferdousa, N., S. Rahman, R. Kabir and A.E. Ahmed, *A comparative study on tensile strength of different weave structures,* International Journal of Scientific Research Engineering & Technology, 2014. **3**(9): p. 1307-1313.
41. Fatahi, I.I. and A. Alamdar Yazdi, *Assessment of the relationship between air permeability of woven fabrics and its mechanical properties.* Fibres & Textiles in Eastern Europe, 2010. **18**(83): p. 68-71.
42. Ogulata, R.T. and F.D. Kadem, *Prediction of regression analyses of fabric tensile strength of 100% cotton fabrics with yarn dyed in different constructions.* Textile and Confection, 2008. **18**(3): p. 185-190.
43. Unal, P. and C. Taskın, *%100 poliester kumaşlarda dokunun ve sıklıkların kopma mukavemetine etkisi*, Tekstil ve Konfeksiyon, 2007. **17**(2): p. 115-118.
44. Ozdemir, H. and E. Mert, *The effects of fabric structural parameters on the breaking, bursting and impact strengths of diced woven fabrics.* Textile and Confection, 2013. **23**(2): p. 113-123.
45. Kurtca, E., *Atkı ipliği özellikleri, sıklık ve örgü tipinin kumaş mekanik özellikleri üzerine etkisi, in Textile Engineering2001*, Istanbul Technical University: Turkey. p. 74.
46. Yılmaz Akyurek, B., *Şardonlamanın bi-elastik dokuma kumaşlarda mekanik özellikler üzerine etkisinin deneysel belirlenmesi*. Tekstil ve Mühendis, 2016. **23**(101): p. 1-11.

Available online at www.dergipark.org.tr/en

INTERNATIONAL ADVANCED RESEARCHES
and
ENGINEERING JOURNAL

Journal homepage: www.dergipark.org.tr/en/pub/iarej

e-ISSN: 2618-575X

International Open Access

Volume 06
Issue 01

April, 2022

Research Article

Thermoeconomic analysis of a geothermal and solar assisted combined organic Rankine and absorption cycle

Ozan Sen [a,*] ***and Ceyhun Yilmaz*** [a]

[a]*Deparment of Mechanical Enginnering, Afyon Kocatepe University, Technology Faculty, Afyonkarahisar, Turkey*

ARTICLE INFO

Article history:
Received 25 October 2021
Accepted 01 February 2022
Published 15 April 2022

Keywords:
Absorption cooling
Geothermal energy
Organic rankine cycle
Solar energy

ABSTRACT

In this paper, a geothermal and solar-assisted combined system is designed for the electricity and cooling of residences. The geothermal water from the geothermal resource and the heat transfer fluid heated in the parabolic trough collector is used as the heat source in the absorption cooling system. The organic Rankine cycle (ORC) generates power with geothermal water and heat transfer fluid from the absorption cooling cycle. The produced power is supported to the grid. Engineering Equation Solver (EES) and Aspen Plus program are used for thermodynamic and thermoeconomic analysis of the combined system. In these analyzes, the geothermal and solar energy values of Afyonkarahisar city are considered. Geothermal water at a temperature of 130 ºC and a mass flow rate of 85 kg/s and a solar source at 600 W/m^2 radiation is used for the combined system. Parametric studies are performed to demonstrate the way unit electricity and cooling costs change according to the geothermal water temperature and solar radiation. The cooling capacity and the net power output of the system are 2720 kW and 2235 kW, respectively. The unit costs of cooling and electricity in the combined system are calculated 0.017 $/kWh and 0.074 $/kWh, respectively.

1. Introduction

Climate change is a global problem facing the whole world today. The leading cause of this problem is global warming resulting from greenhouse gas emissions. Carbon dioxide (CO_2) is the primary greenhouse gas released from burning fossil fuels such as oil, natural gas, and coal [1]. Meeting the energy demand of any country is of great importance for the development and progress of that country. Especially in the last 20 years, the countries' energy demands have increased due to the increase in the world population. In order to meet this increase in demand, alternative and uninterrupted energy sources are needed [2].

Due to the depletion of fossil fuels and their harmful environmental effects, the search for sustainable and environmentally friendly alternative energy sources has accelerated in recent years. Investments in renewable energy sources are increasing day by day. As a result of the development of engineering applications and technology, the efficiency obtained from renewable energy sources is constantly increasing [3].

Geothermal energy is a renewable source of heat accumulated underground. Geothermal energy reaches the earth's surface in different forms and proportions. Geothermal energy is a renewable energy source without greenhouse gas emissions and environmental pollution [4]. Since geothermal energy works almost all year round, it can produce energy continuously. It is a very efficient source for power generation, district heat, and cooling [5].

In recent years, interest in solar energy has increased worldwide. Solar energy is a renewable and sustainable energy source. The thermal energy of solar energy is an essential alternative to fossil fuels [6]. Cooling systems are expensive systems due to high electricity consumption. Solar and geothermal energy are alternative energy sources to eliminate this electricity cost [7].The most mature cooling technologies are sorption machines, absorption, and adsorption cooling systems. [8] Absorption cooling systems with LiBr-H_2O operate at lower thermal energies than absorption cooling systems with NH_3-H_2O. Absorption cooling systems with LiBr-H_2O have higher efficiency because they work at the higher coefficient of performance (COP) values [9]. The absorption coolingsystem with LiBr-H_2O is the most suitable cooling system due to its low-temperature operation and simple structure [10]. The

* Corresponding author. Tel.: +90-272-218-2549.
E-mail addresses: ozansen@usr.aku.edu.tr *(O.Sen)*, ceyhunyilmaz@aku.edu.tr *(C.Yilmaz)*
ORCID:0000-0002-9913-664X *(O. Sen)*, 0000-0002-8827-692X *(C. Yilmaz)*
DOI: 10.35860/iarej.1014569

single-effect absorption cooling system with LiBr-H_2O has a wide range of applications [11].

Combined cooling and power (CCP) systems are highly efficient systems that can produce both cooling and electricity from one or more heat sources. It works with higher efficiency than independent cooling and power systems [12]. Fossil fuels operate the majority of cooling and power systems around the world. The fact that fossil fuels cause high carbon emissions and severe environmental problems has accelerated the transition to renewable energy sources [13].

Turkey has rich sources of renewable energy. Geothermal and solar-powered electricity production has become popular and common in Turkey, especially in recent years. The industrial output growth has increased Turkey's energy demand in recent years. In order to meet this energy demand, reduce external dependency and decarbonize the energy sector, the capacity of renewable energy sources should be maximized. [14].

Few studies on geothermal and solar-assisted electricity and cooling production are in the literature. These studies are presented in the literature review. Alibaba et al. [15] investigated a individual geothermal cycle and a hybrid geothermal-solar cycle to produce the cooling- heating power of the building. The exergoeconomic analysis of the cycles showed that the solar power plant has the highest cost. Calise et al. [16] proposed a hybrid geothermal-solar plant producing electricity, heat, and cool. As a result of the thermoeconomic analysis of the hybrid geothermal-solar power plant, the payback period of the plant is calculated as 16.7 years. Alirahmi et al. [17] developed a multi-generation geothermal and solar-powered energy system. As a result of thermoeconomics analysis and optimization, the exergetic efficiency and total unit cost of the system are 29.95% and 129.7 $/GJ. Ghasemi et al. [18] compared a hybrid system utilizing geothermal energy and parabolic collectors and the individual geothermal system. The solar and geothermal energy-powered hybrid system showed higher exergy efficiency than the individual geothermal system. Heberle et al. [19] have integrated solar energy into a geothermal-assisted ORC power plant. The geothermal and solar energy-assisted combined system and the individual geothermal system are compared. The combined system has 7.8% more electricity and power than the individual system. Mctigue et al. [20] designed a geothermal and solar energy assisted hybrid power plant. They considered a double flash for a geothermal resource and a concentrated collector for a solar resource and performed the energy and economic analysis of the hybrid power plant. The hybrid plant's unit electricity cost that increased power generation from 22 to 24 MW was obtained 0.07 ± 0.01 $/kWh. Kehvarparast et al. [21] studied thermodynamic analysis for a geothermal power plant hybridized with parabolic trough collectors. A thermodynamic analysis of the hybrid plant is performed. The energy consumption of the fan and the condenser decreased 47.32% and 33.58%, respectively. Haghghi et al. [22] have integrated solar-assisted an ORC and an absorption cooling cycle for power, heating and cooling production. The power, heating and cooling costs are calculated as 15.47 $/GJ, 10.27 $/GJ, and 11.44 $/GJ, respectively. Ayub et al. [23] designed a geothermal resource and parabolic solar collector system. The result of the thermoeconomic analysis indicated that the unit electricity cost of a hybrid system decreased by 2% compared to a standalone geothermal system.

This study performs thermodynamic and thermoeconomic evaluation of a combined absorption cooling and organic Rankine cycle [24]. The absorption cooling cycle for cooling residences and ORC for electricity of residences is considered. The purchased equipment cost of the combined system is calculated in the Aspen Plus program [25]. This paper is a novelty in adding a solar power system to an existing geothermal power plant in Afyonkarahisar. Through the developed model, electricity and cooling production are combined. Two useful outputs are obtained from the combined system. This study contributes to supplying the energy demand of Afyonkarahisar from renewable resources and competitive costs.

The steps to be applied in the study can be written as: (i) the combined system is modeled and solved thermodynamically in a computer environment, (ii) in the thermodynamic and thermoeconomic analysis of the combined system, the geothermal and solar energy values of Afyonkarahisar are used, (iii) parametric analyses of the combined system are performed at different geothermal water temperatures and solar radiation, (iv) unit electricity and cooling costs of the combined system are investigated under different conditions.

2. Description and Operating Principle

In this study, an integrated approach is developed to requirements residential buildings' cooling and electricity supply. In the absorption cooling cycle, the electrical input is replaced by renewable energy heat energy. The cooling process is provided by this heat energy and two working fluids. Conventional vapor compression cycles use a compressor to circulate the refrigerant and create pressure differences. The absorption cooling system circulates the coolant with the help of a secondary fluid or absorber.

Using parabolic trough solar collectors is one of the effective ways to benefit from solar energy with high efficiency. Parabolic trough collectors are used to produce steam from solar energy. The receiver tube of the parabolic trough collector is located along the focal line. In order to reduce heat losses, the surface of the receiver is covered with a glass cover tube along the focal line. The rays from

the sun are reflected in the receiver tube by the parabolic reflective mirrors. Concentrated radiation reaching the receiver tube heats the heat transfer fluid circulating in the receiver, and solar radiation is converted into useful heat. This useful heat is used for power generation in ORC [26].

In Figure 1, hot geothermal water from the geothermal resource (at state 7) and hot heat transfer fluid (Therminol VP-1) heated in the parabolic trough collector (at state 10) is the heat input of the absorption cooling system. The refrigerant vapor in the evaporator and is sent to the absorber (at state 21). The refrigerant vapor is absorbed by lithium bromide in the absorber. The weak solution of lithium bromide enters (at state 13) the heat exchanger by increasing the pressure by the pump. The weak solution of lithium bromide is heated in the heat exchanger and enters the generator (at state 14). With the heat energy transfer of hot geothermal water and hot heat transfer fluid, the refrigerant vapors and leaves (at state 18) the solution. The refrigerant vapor leaving the generator enters the condenser and condensed it in the condenser. The pressure of the liquid refrigerant is reduced in the expansion valve and sent to the evaporator (at state 20). As the refrigerant passes through the evaporator, it absorbs the heat of the hot water, and cold water is produced (at state 23). The cold water leaving the evaporator is sent to the heat exchanger for district cooling, producing cold air (at state 26). The cold air produced is sent to the buildings for district cooling.

The ORC uses the geothermal water and heat transfer fluid as the heat source for electricity generation. R134a is used as the working fluid in the ORC. The geothermal water (at state 8) and heat transfer fluid (at state 11) leaving the generator of the absorption cooling cycle enters the heat exchanger of the ORC to heat a working fluid. The working fluid leaves (at state 3) the heat exchanger as vapor. The vaporized working fluid is sent to the turbine to generate electricity. Electricity is supplied to the grid. The vaporized working fluid leaving the turbine is sent (at state 4) to the water-cooled condenser and condensed in the condenser. The working fluid leaves (at state 1) the condenser as liquid, and the cycle is completed. The geothermal water is reinjected (at state 9) back to the resource. The Therminol VP-1 fluid is pumped (at state 28) to the parabolic trough collector to be reheated.

The geothermal water enters the combined system at 130 °C and is reinjected back to the resource at 60°C. The solar radiation for the solar source is 600 W/m^2, and the mass flow rate of working fluid circulating in the parabolic collector is 0.2 kg/s [27].

3. Thermodynamic Analysis

Thermodynamic assumptions for the geothermal and solar-assisted combined organic Rankine and absorption cycle are given following. The equipment of the system operates on a steady-state and steady flow condition. The potential and kinetic changes are negligible. The isentropic efficiency of pumps and turbines is 85%.The pressure drops and losses in the equipment of the system are negligible. Environment temperature is 25°C and atmospheric pressure is 100 kPa. Considering the temperature range and solar radiation, Therminol VP-1 is chosen as the working fluid in the parabolic collectors [28].

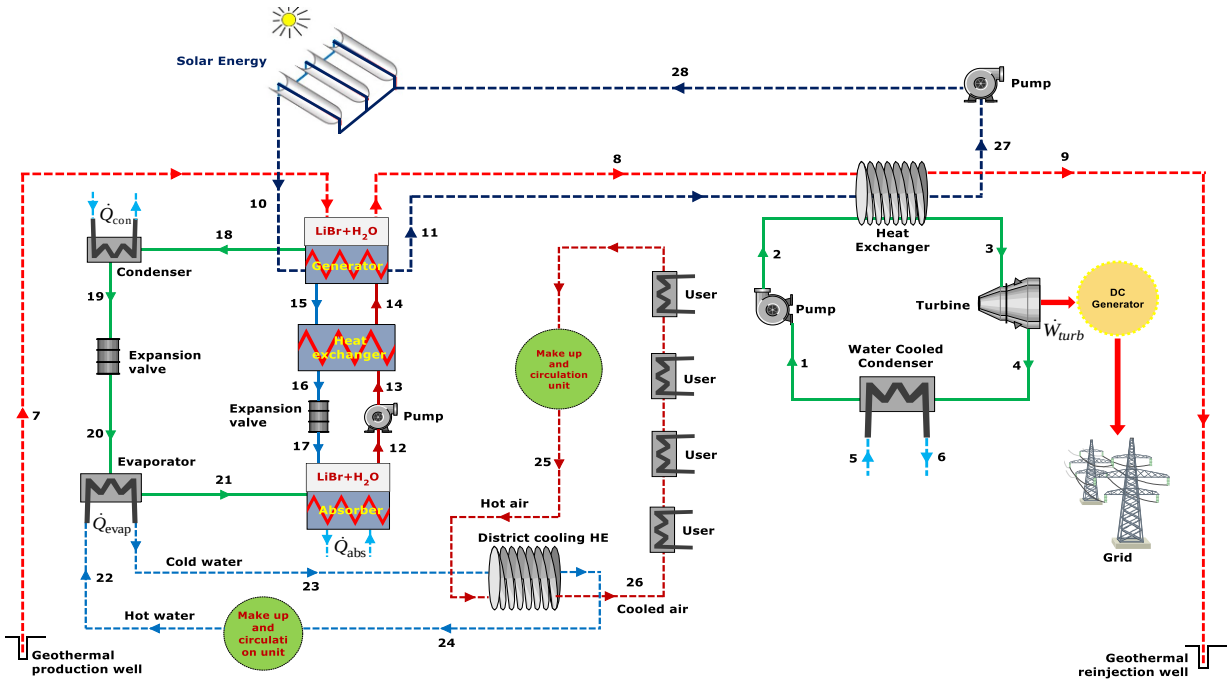

Figure 1. Geothermal and solar energy combined system

The COP value of the absorption cooling cycle is calculated from:

$$COP_{ARC} = \frac{\dot{Q}_{eva}}{(\dot{Q}_{gen} + \dot{W}_{pump})} \quad (1)$$

where, $\dot{Q}_{eva}$ is the cooling capacity of the evaporator, $\dot{Q}_{gen}$ is the heat capacity of the generator and $\dot{W}_{pump}$ is pump power.

The exergy efficiency of the absorption cooling cycle can be determined with the help of the following equation:

$$\varepsilon_{ARC} = \frac{-\dot{Q}_{eva}(T_0 / T_E - 1)}{\dot{Q}_{gen}(T_0 / T_G - 1)} \quad (2)$$

where, T_0 is ambient temperature, T_E is evaporator temperature and T_G is generator temperature.

The power output from the ORC is calculated from [29]:

$$\dot{W}_{net} = \dot{W}_T - \dot{W}_P \quad (3)$$

where, $\dot{W}_T$ is turbine power and $\dot{W}_P$ is pump power.

The overall energy efficiency of ORC is the ratio of net power output to energy input, and the overall exergy efficiency of ORC can be defined as [29]:

$$\eta_{ORC} = \frac{\dot{W}_{net}}{\dot{Q}_{in}} \quad (4)$$

$$\varepsilon_{ORC} = \frac{\dot{W}_{net}}{\dot{E}x_{in}} \quad (5)$$

Energy efficiency for the overall system can be calculated by ratio of net power output from ORC and the cooling capacity of the evaporator to the total heat energy entering the overall system:

$$\eta_{overall} = \frac{\dot{W}_{net} + \dot{Q}_{eva}}{\dot{Q}_{geo} + \dot{Q}_{solar}} \quad (6)$$

For the combined system, the expression of exergy efficiency determined as follows:

$$\varepsilon_{overall} = \frac{\dot{W}_{net} + \dot{Q}_{eva}((T_0 / T_E) - 1)}{\dot{E}x_{geo} + \dot{E}x_{solar}} \quad (7)$$

4. Thermoeconomic Analysis

Engineering economics is a science that offers techniques for the economic analysis of engineering systems [30]. Determining the cost of the system and choosing the best alternative is a fundamental issue in engineering economics. In economic analysis, the operating and maintenance costs and the levelized capital investment costs of the investigated system are provided [29].

The capital recovery factor (CRF) can be calculated depending on the interest rate (i) and the life time period of the system (n) [31]:

$$\mathrm{CRF} = \frac{i(1+i)^n}{(1+i)^n - 1} \quad (8)$$

The $\dot{Z}$ is the total cost rate (\$/h) summation with ($\dot{Z}^{CI}$) capital I nvestment and ($\dot{Z}^{OM}$) the operating and maintenance costs [31]:

$$\dot{Z} = \dot{Z}^{\mathrm{CI}} + \dot{Z}^{\mathrm{OM}} \quad (9)$$

Thermoeconomics is a discipline that considers both thermodynamics and economics. Many different economic applications can be used in engineering systems. Considering exergy values would be a better option for engineering economics. Therefore, the specific exergy costing method (SPECO) is preferred for thermoeconomic analysis. The fundamental principles of the SPECO method are the direct application of exergy flows instead of matter and energy flows. The three steps of this method are; (i) identification of exergy streams, (ii) definition of fuel and product (iii) cost equations and derivation of auxiliary equations [32].

In the SPECO method, all exergy streams are associated with a cost. Thus, the exergy transfer rate associated with entering and exiting streams of the equipment, the exergy transfer rate associated with output work and input heat can be expressed [32]:

$$\dot{C}_{\mathrm{i}} = c_{\mathrm{i}}\dot{E}x_{\mathrm{i}} = c_{\mathrm{i}}(\dot{m}_{\mathrm{i}}ex_{\mathrm{i}}) \quad (10)$$

$$\dot{C}_{\mathrm{e}} = c_{\mathrm{e}}\dot{E}x_{\mathrm{e}} = c_{\mathrm{e}}(\dot{m}_{\mathrm{e}}ex_{\mathrm{e}}) \quad (11)$$

$$\dot{C}_{\mathrm{w}} = c_{\mathrm{w}}\dot{W} \quad (12)$$

$$\dot{C}_{\mathrm{q}} = c_{\mathrm{q}}\dot{E}x_{\mathrm{q}} \quad (13)$$

For a *k* component receiving the heat and the power can be written as [32]:

$$\sum_{\mathrm{e}}\left(c_{\mathrm{e}}\dot{E}x_{\mathrm{e}}\right)_{\mathrm{k}} + c_{\mathrm{w,k}}\dot{W}_{\mathrm{k}} = c_{\mathrm{q,k}}\dot{E}x_{\mathrm{q,k}} + \sum_{\mathrm{i}}\left(c_{\mathrm{i}}\dot{E}x_{\mathrm{i}}\right)_{\mathrm{k}} + \dot{Z}_{\mathrm{k}} \quad (14)$$

where, c_e, c_i, c_w and c_q denote average costs per unit of exergy in dollars per gigajoule (\$/GJ). c_i and c_e are the cost per unit associated with the inlet and outlet exergy stream. c_w and c_q are the cost per unit associated with the output work and heat [32].

The certain assumptions are performed in the economic and thermoeconomics analysis. The annual working hour of the system is 7446 hours and its economic life is 20 years. The annual interest rate (i, interest rate) is assumed as 10% [31].

Primarily, combined system simulated and operated in the Aspen Plus program and the purchase costs of the equipment are obtained. Then, in the EES program, the necessary data calculated for the system are coded into the program by us, and the results of thermoeconomic analysis are obtained.

5. Results and Discussion

Energy, exergy and economic analysis results of the combined system are presented in this section. The thermophysical properties of the geothermal water, R134a fluid and lithium-bromide (LiBr-H_2O) solution are provided from the EES program. For the thermoeconomic analysis to be concluded correctly, the thermodynamic analysis should be performed carefully. Therefore, thermodynamic analysis is critical to the economic results of the study.

The geothermal fluid and heat transfer fluid (Therminol VP-1), 25,261 kW of heat and 5578 kW of exergy are input to the combined energy system. Geothermal water (130°C and 85 kg/s) from the production well and Therminol VP-1 fluid (145°C and 0.2 kg/s) from the parabolic trough collector are heat sources of the absorption cooling system. Considering these thermodynamic properties, the heat transferred to the generator is calculated as 3634 kW. The cooling capacity of the absorption cooling system is 2720 kW. The actual COP value of the absorption cooling system is determined as 0.748 from Equation (1). The second law efficiency of the absorption cooling system is 22.5% from Equation (2).

Table 1. Thermoeconomics values of components [22]

Component	PEC ($)	$\dot{Z}$ ($/h)
ORC-Pump	70,000	1.17
ORC-Heat exchanger	325,000	5.43
ORC-Turbine	480,000	8.028
ORC-Condenser	325,000	5.436
Pump-1	5000	0.083
Expansion valve-1	5000	0.083
Heat exchanger-1	22,000	0.367
Generator	100,000	1.672
Condenser	26,900	0.449
Expansion valve-2	5000	0.083
Evaporator	11,500	0.192
Absorber	94,200	1.575
Heat exchanger-2	11,500	0.192
Pump-2	1000	0.016
Parabolic collector	72,000	1.203
Total PEC	**1,554,100**	-

The geothermal water and Therminol VP-1 fluid from the absorption cooling system, 21,579 kW of heat and 4505 kW of exergy are the input of the ORC in which the electricity is produced. The net power obtained from the ORC is determined as 2235 kW. The first law efficiency of ORC is calculated as 10.3% and second law efficiency as 49.6%. The first law efficiency of the combined system is 19.6%, and the second law efficiency is 43.7%.

The annual working hour for the system is 7446 hours and its economic life is 20 years. The annual interest rate (i) we use in economic analysis has been accepted as 10%. The CRF value is calculated as 0.1175. Table 1 below created for the system shows the purchased equipment costs (PEC) of the model equipment and the total cost rate ($\dot{Z}$). The total PEC of the equipment used in the model is calculated as $ 1,554,100.

Based on the SPECO method, all equations used in the thermoeconomic analysis of the combined system are given in Table 2.

Table 2. Thermoeconomic equations of the components associated with exergy

Component	Exergetic cost rate balance equation	Auxiliary equations
ORC-Pump	$\dot{C}_1 + \dot{Z}_P + \dot{C}_{W_p} = \dot{C}_2$	c_1 (is known) c_2 (variable)
ORC-Heat exchanger	$\dot{C}_2 + \dot{C}_8 + \dot{C}_{11} + \dot{Z}_{HE} = \dot{C}_3 + \dot{C}_9 + \dot{C}_{27}$	$c_8 = c_9$
ORC-Turbine	$\dot{C}_3 + \dot{Z}_T = \dot{C}_{W_T} + \dot{C}_4$	$c_3 = c_4$ $c_{electricity}$ (variable)
ORC-Condenser	$\dot{C}_4 + \dot{C}_5 + \dot{Z}_{WCC} = \dot{C}_1 + \dot{C}_6$	$c_5 = 0$
Pump-1	$\dot{C}_{12} + \dot{Z}_P + \dot{C}_{W_p} = \dot{C}_{13}$	c_{12} (is known)
Heat exchanger-1	$\dot{C}_{13} + \dot{C}_{15} + \dot{Z}_{HE} = \dot{C}_{14} + \dot{C}_{16}$	$c_{15} = c_{16}$
Generator	$\dot{C}_7 + \dot{C}_{10} + \dot{C}_{14} + \dot{Z}_{GEN} = \dot{C}_8 + \dot{C}_{11} + \dot{C}_{15} + \dot{C}_{18}$	$c_7 = c_8$
Condenser	$\dot{C}_a + \dot{C}_{18} + \dot{Z}_{CON} = \dot{C}_b + \dot{C}_{19}$	$c_a = 0$
Evaporator	$\dot{C}_{20} + \dot{C}_{22} + \dot{Z}_{EVA} = \dot{C}_{21} + \dot{C}_{23}$	$c_{22} = 0$ $c_{20} = c_{21}$
Absorber	$\dot{C}_c + \dot{C}_{17} + \dot{C}_{21} + \dot{Z}_{ABS} = \dot{C}_d + \dot{C}_{12}$	$c_c = 0$
Heat exchanger-2	$\dot{C}_{23} + \dot{C}_{25} + \dot{Z}_{DHE} = \dot{C}_{24} + \dot{C}_{26}$	$c_{25} = 0$ $c_{23} = c_{24}$
Parabolic collector	$\dot{C}_{28} + \dot{Z}_{PTC} = \dot{C}_{10}$	c_{28} (is known)

In consideration of technical assumptions, auxiliary equations are solved in the EES program accordingly.

The unit cooling cost is 0.074 $/kWh (20.77 $/GJ) in the absorption cooling cycle. The unit electricity cost (LCOE) produced in the ORC cycle is 0.017 $/kWh (4.71 $/GJ).

In this section, the variation of unit cooling and electricity costs in different geothermal water temperatures and solar radiation are investigated. In Figures 2 and 3, the geothermal water temperature varies between 120 and 150°C, while the solar radiation is constant at 600 W/m^2. When Figure 2 is observed, the increase in geothermal water temperature caused an increase in unit cooling cost. This is because the absorption cooling cycle can use a lower proportion of geothermal energy at a higher geothermal source temperature.

Figure 3 indicates the variation of unit electricity cost at different geothermal temperatures. At high temperatures, the unit electricity cost decreases linearly because more power is obtained from geothermal energy. The unit cooling and electricity costs corresponding to the geothermal data points are given in Table 3.

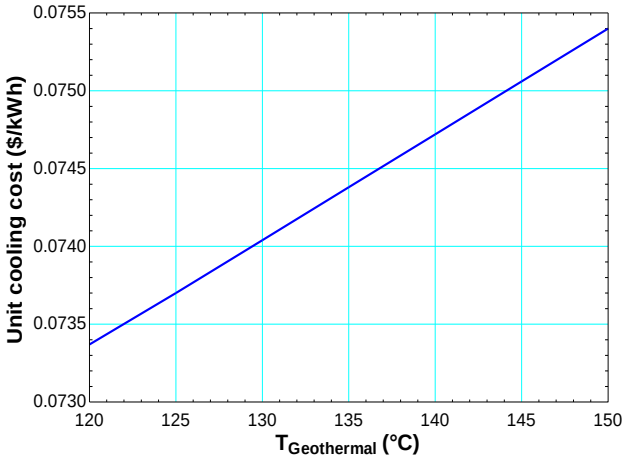

Figure 2. Variation of unit cooling cost with the geothermal temperature.

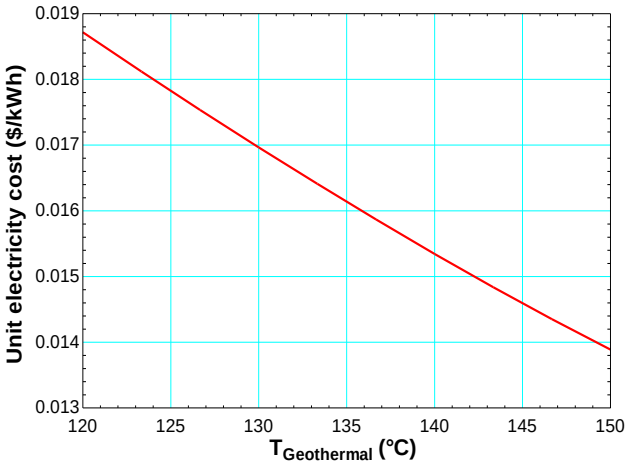

Figure 3. Variation of unit electricity cost with the geothermal temperature

Table 3. Unit cooling and electricity cost corresponding to geothermal data points.

Geothermal temperature (°C)	Unit cooling cost ($/kWh)	Unit electricity cost ($/kWh)
120	0.0733	0.0187
125	0.0737	0.0178
130	0.0740	0.0169
135	0.0743	0.0161
140	0.0747	0.0153
145	0.0751	0.0145
150	0.0754	0.0138

In Figures 4 and 5, the solar radiation varies between 300 and 1000 W/m^2, while the geothermal water temperature is constant at 130°C. Figure 4 shows the variation of unit cooling cost at different solar radiations. When Figure 4 is observed, the unit cooling cost increases because solar energy can be used at a lower level with the increase of solar radiation. Since the absorption cooling cycles can absorb and use the energy at high temperatures to a certain ratio, the COP and cooling capacity of the cooling cycles decrease with the increase in the source temperature. Thus the cooling costs increase linearly.

When Figure 5 is observed, solar radiation directly affects the unit electricity cost. With the increase of solar radiation, the production cost of electricity decreases because more energy is used. This parametric study showed that the effect of solar radiation on system outputs (unit cooling and electricity cost) is lower than that of geothermal water. This is because the power output is far less than geothermal resource due to the considerable amount of losses in the parabolic collectors. Table 4 for solar data points shows unit cooling and electricity costs.

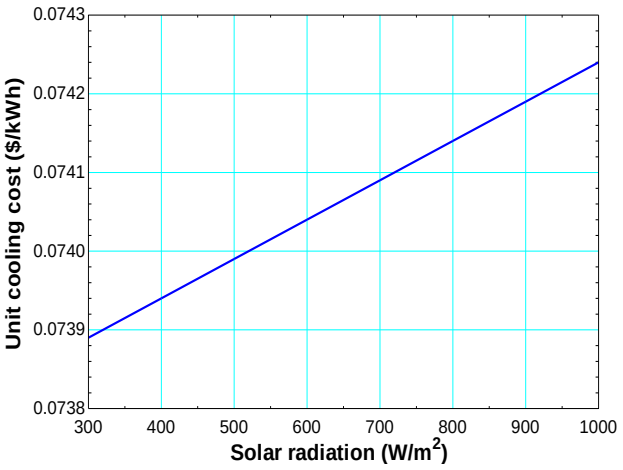

Figure 4. Variation of unit cooling cost with the solar radiatio

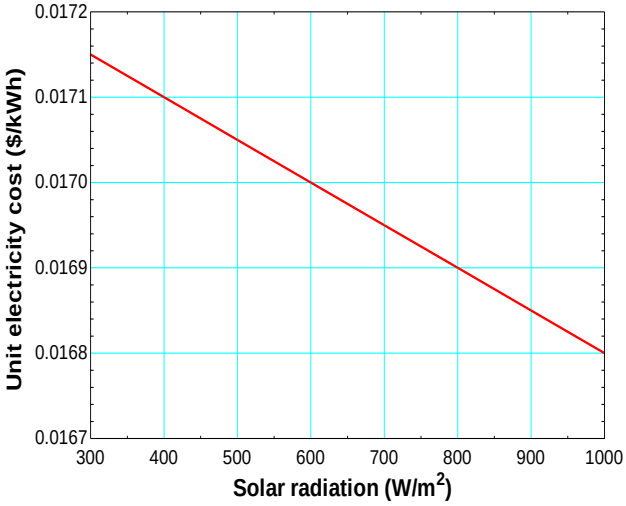

Figure 5. Variation of unit electricity cost with the solar radiation

Table 4. Unit cooling and electricity cost corresponding to solar data points

Solar radiation (W/m^2)	Unit cooling cost ($/kWh)	Unit electricity cost ($/kWh)
300	0.07389	0.01715
400	0.07394	0.01710
500	0.07399	0.01705
600	0.07404	0.0170
700	0.07409	0.01695
800	0.07414	0.01690
900	0.07419	0.01685
1000	0.07424	0.01680

5.1 Proposed System Validation and Comparison

This geothermal and solar energy combined system has a 2720 kW cooling capacity and 2235 kW net power. The combined system's first and second law efficiencies are 19.6% and 43.7%. The unit cooling and electricity cost is 0.074 $/kWh (20.77 $/GJ) and 0.017 (4.71 $/GJ) $/kWh, respectively.

Alirahmi et al. [17] developed a multi-generation solar and geothermal energy-powered system. According to thermodynamic analysis and optimization, the exergetic efficiency of the system is 29.95%, and the total unit cost is 129.7 $/GJ. Heberle et al. [19] have integrated solar energy into a geothermal assisted ORC plant. The obtained results of the system show the LCOE with 0.145 $/kWh considering costs for operation and maintenance of 0.0023 $/kWh. Mctigue et al. [20] performed thermodynamic and thermoeconomic analysis of a hybrid plant integrating heat from a concentrating solar collector for a geothermal plant. The energy efficiency of the hybrid plant is 17.3%. The levelized cost of electricity (LCOE) of the hybrid plant is obtained 0.07 $/kWh. Haghghi et al. [22] have integrated solar-assisted an ORC and an absorption cooling cycle for power, heating and cooling production. The power, heating, and cooling costs are calculated as 15.47 $/GJ, 10.27 $/GJ, and 11.44 $/GJ. Behnam et al. [33] designed a geothermal energy-assisted system for producing freshwater, heating, and electricity. Electricity is generated in the ORC. The unit electricity cost is 0.0402 $/kWh. Ghiasirad et al. [34] performed a thermoeconomics analysis of geothermal-assisted combined power, heating and cooling system. The absorption chiller's COP and cooling capacity are 0.798 and 4991 kW. The unit electricity and cooling costs of the combined system are calculated 0.562 and 0.201 $/kWh, respectively.

6. Conclusions

Geothermal and solar energy is widely used in many countries today. Geothermal and solar energy is among the fastest-growing renewable energy technologies in Turkey in recent years. Geothermal and solar energy can be widely used in electricity generation, heating, cooling, industrial applications, and greenhouse cultivation. The use of economically renewable energy sources in heating and cooling also makes electricity production more profitable. In addition, the use of renewable energy sources in power and cooling production helps to eliminate fossil fuel emissions. The most significant advantage of renewable energy-powered systems is that exhaust gases do not contain hydrocarbon emissions. When all the results are evaluated together, it is seen that different approaches can be developed for the use of renewable energies in cooling systems, and they can be successfully applied in terms of thermodynamics.

The absorption cooling cycle considered for district cooling in has been successfully combined with the organic Rankine cycle for electricity generation. The unit cooling and electricity cost is calculated as 0.074 $/kWh and 0.017 $/kWh, respectively. This study proved that it is technically and cost-effectively possible to integrate power generation and space cooling into a system. The next stage of this study is to find the optimum operating conditions for the system by optimizing the system. As a result, it is expected that the cooling and power production of the system will increase, and the cost of unit cooling and electricity produced will decrease.

The study results will be beneficial for researchers interested in the variation of different operating temperatures on energy and exergy costs, as well as improving the sustainable energy demand.

Declaration

The authors declared no potential conflicts of interest with respect to the research, authorship, and/or publication of this article. The authors also declared that this article is original, was prepared in accordance with international publication and research ethics, and ethical committee permission or any special permission is not required.

Author Contributions

C. Yilmaz developed the methodology. O. Sen performed the analysis. C. Yilmaz and O. Sen wrote the manuscript together.

Acknowledgment

This study supported by TUBITAK under Research Project (project no: 218M739), Turkey.

Nomenclature

$\dot{C}$	: Cost rate associated with exergy [$/h]
$\dot{E}x$	: Exergy rate [kW]
i	: Interest rate [%]
$\dot{m}$	: Mass flow rate [kg/s]
n	: Operating period
$\dot{Q}$	: Heat energy [kW]
T	: Temperature [ºC]
$\dot{W}$	: Power [kW]
$\dot{Z}$	: Equipment cost rate [$/h]
η	: Energy efficiency
ε	: Exergy efficiency

References

1. Salehi, S., Yari, M.and Rosen, M. A.,*Exergoeconomic comparison of solar-assisted absorption heat pumps, solar heaters and gas boiler systems for district heating in Sarein Town, Iran*. Applied Thermal Engineering, 2019. **153**: p. 409-425.
2. Rahman, A., Abas, N., Dilshad, S.and Saleem, M. S.,*A case study of thermal analysis of a solar assisted absorption air-conditioning system using R-410A for domestic applications.* Case Studies in Thermal Engineering, 2021. **26**: 101008.
3. Yu, J., Tang, Y. M., Chau, K. Y., Nazar, R., Ali, S., and Iqbal, W.,*Role of solar-based renewable energy in mitigating CO2 emissions: Evidence from quantile-on-quantile estimation*. Renewable Energy, 2021. **182**: p. 216-226.
4. El Haj Assad, M., Sadeghzadeh, M., Ahmadi, M. H., Al-Shabi, M., Albawab, M., Anvari-Moghaddam, A. and Bani Hani, E.,*Space cooling using geothermal single-effect water/lithium bromide absorption chiller*. Energy Science & Engineering, 2021. **9**: p. 1747-1760.
5. Mirzaee, M., Zare, R., Sadeghzadeh, M., Maddah, H., Ahmadi, M. H., Acıkkalp, E. and Chen, L., *Thermodynamic analyses of different scenarios in a CCHP system with micro turbine–Absorption chiller, and heat exchanger*. Energy Conversion and Management, 2019. **198**: 111919.
6. Rahman, A., Abas, N., Dilshad, S. and Saleem, M. S.,*A case study of thermal analysis of a solar assisted absorption air-conditioning system using R-410A for domestic applications*. Case Studies in Thermal Engineering, 2021. **26**: 101008.
7. Gunhan, T., Ekren, O., Demir, V., Hepbasli, A., Erek, A.and Sahin, A. S.,*Experimental exergetic performance evaluation of a novel solar assisted LiCl–H2O absorption cooling system*. Energy and buildings, 2014. **68**: p. 138-146.
8. Zhai, X. Q., Qu, M., Li, Y., Wang, R. Z. *A review for research and new design options of solar absorption cooling systems*. Renewable and sustainable energy reviews, 2011. **15**: p. 4416-4423.
9. Hassan, H. Z., & Mohamad, A. A. *A review on solar cold production through absorption technology*. Renewable and Sustainable Energy Reviews, 2012. **16**: p. 5331-5348.
10. Cabrera, F. J., Fernández-García, A., Silva, R. M. P., & Pérez-García, M. *Use of parabolic trough solar collectors for solar refrigeration and air-conditioning applications*. Renewable and sustainable energy reviews, 2013. **20**: p. 103-118.
11. Bellos, E., Tzivanidis, C. and Antonopoulos, K. A., *Exergetic, energetic and financial evaluation of a solar driven absorption cooling system with various collector types*. Applied Thermal Engineering, 2016. **102**: p. 749-759.
12. Parikhani, T., Ghaebi, H.and Rostamzadeh, H.,*A novel geothermal combined cooling and power cycle based on the absorption power cycle*: *Energy, exergy and exergoeconomic analysis*. Energy, 2018. **153**: p. 265-277.
13. Wang, Y., Chen, T., Liang, Y., Sun, H. and Zhu, Y.,*A novel cooling and power cycle based on the absorption power cycle and booster-assisted ejector refrigeration cycle driven by a low-grade heat source: Energy, exergy and exergoeconomic analysis*. Energy Conversion and Management, 2020. **204**: 112321.
14. Yilmaz, C.,*Thermoeconomic cost analysis and comparison of methodologies for Dora II binary geothermal power plant*. Geothermics, 2018. **75**: p. 48-57.
15. Alibaba, M., Pourdarbani, R., Manesh, M. H. K., Ochoa, G. V. and Forero, J. D.,*Thermodynamic, exergo-economic and exergo-environmental analysis of hybrid geothermal-solar power plant based on ORC cycle using emergy concept*. Heliyon, 2020. **6**: e03758.
16. Calise, F., Cappiello, F. L., d'Accadia, M. D. and Vicidomini, M.,*Energy and economic analysis of a small hybrid solar-geothermal trigeneration system: A dynamic approach*. Energy, 2020. **208**: 118295.
17. Alirahmi, S. M., Dabbagh, S. R., Ahmadi, P. and Wongwises, S.,*Multi-objective design optimization of a multi-generation energy system based on geothermal and solar energy*. Energy Conversion and Management, 2020. **205**: 112426.
18. Ghasemi, H., Sheu, E., Tizzanini, A., Paci, M. and Mitsos, A.,*Hybrid solar–geothermal power generation: Optimal retrofitting.* Applied energy, 2014. **131**: p. 158-170.
19. Heberle, F., Hofer, M., Ürlings, N., Schröder, H., Anderlohr, T.and Brüggemann, D.,*Techno-economic analysis of a solar thermal retrofit for an air-cooled*

geothermal Organic Rankine Cycle power plant. Renewable Energy, 2017. **113**: p. 494-502.

20. McTigue, J. D., Castro, J., Mungas, G., Kramer, N., King, J., Turchi, C. and Zhu, G.,*Hybridizing a geothermal power plant with concentrating solar power and thermal storage to increase power generation and dispatchability*. Applied energy, 2018. **228**: p. 1837-1852.
21. Keshvarparast, A., Ajarostaghi, S. S. M. and Delavar, M. A.,*Thermodynamic analysis the performance of hybrid solar-geothermal power plant equipped with air-cooled condenser*. Applied Thermal Engineering, 2020. **172**: 115160.
22. Haghghi, M. A., Mohammadi, Z., Pesteei, S. M., Chitsaz, A. and Parham, K.,*Exergoeconomic evaluation of a system driven by parabolic trough solar collectors for combined cooling, heating, and power generation; a case study*. Energy, 2020. **192**: 116594.
23. Ayub, M., Mitsos, A. and Ghasemi, H.,*Thermo-economic analysis of a hybrid solar-binary geothermal power plant*. Energy, 2015. **87**: p. 326-335.
24. F-Chart Software, EES, engineering equation solver. In: F-Chart Software, Internet Website, www.fchart.com/ees/ees.shtml, 2021.
25. Aspen Plus Version 8.4, Aspen Technology Incorporated, Ten Canal Park, Cambridge, MA, USA, Available from: www.aspentech.com, 2014.
26. Kalogirou, S. A. *Solar energy engineering: processes and systems*, Academic Press, 2013.
27. Quoilin S, Orosz M, Hemond H, Lemort V. *Performance and design optimizationof low-cost solar organic Rankine cycle for remote power generation*. Sol Energy, 2011. **85**: p. 955–66.
28. Kumar KR, Reddy KS. *Thermal analysis of solar parabolic trough with porous discreceiver*. Appl Energy 2009. **86**: p. 1804–12.
29. Cengel, Y. A., Boles, M. A., Kanoglu, M., *Thermodynamics: An Engineering Approach*, McGraw-Hill, ninth edition, New York, A.B.D., 2019.
30. Bejan, A., Tsatsaronis, G., Moran, M., *Thermal Design and Optimization*, Wiley&Sons, New York, 1998.
31. Dhillon B. S., *Life Cycle Costing for Engineers*, Crc Press, 2009.
32. Lazzaretto, A. and Tsatsaronis, G., *SPECO: a systematic and general methodology for calculating efficiencies and costs in thermal systems*. Energy, 2006. **31**: p. 1257-1289.
33. Behnam, P., Arefi, A., Shafii, M. B. *Exergetic and thermoeconomic analysis of a trigeneration system producing electricity, hot water, and fresh water driven by low-temperature geothermal sources*. Energy conversion and management, 2018. **157**: p. 266-276.
34. Ghiasirad, H., Asgari, N., Saray, R. K., Mirmasoumi, S. *Thermoeconomic assessment of a geothermal based combined cooling, heating, and power system, integrated with a humidification-dehumidification desalination unit and an absorption heat transformer*. Energy Conversion and Management, 2021. **235**: 113969.

Available online at www.dergipark.org.tr/en

INTERNATIONAL ADVANCED RESEARCHES and ENGINEERING JOURNAL

Journal homepage: www.dergipark.org.tr/en/pub/iarej

e-ISSN: 2618-575X

International Open Access

Volume 06
Issue 01

April, 2022

Research Article

Wearable sensor device for posture monitoring and analysis during daily activities: A preliminary study

Gizem Özgül [a] ***and Fatma Patlar Akbulut*** [a,*]

[a]*Department of Computer Engineering, Faculty of Engineering, İstanbul Kültür University, İstanbul, Turkey*

ARTICLE INFO

Article history:
Received 04 November 2021
Accepted 11 April 2022
Published 15 April 2022

Keywords:
Posture disorder
Rehabilitation
Wearable sensor
Wearable vest

ABSTRACT

The increase in technological advancements in recent years has led to the emergence of a new lifestyle. Although being assisted by machines for small-scale tasks in daily housework makes daily life easier, this has caused people to reduce their daily active movements and negatively affects human health. Especially during the COVID-19 pandemic, with the conversion of the working style to the home environment, working hours spent at the desk are more than ever. Due to the prolongation of the working time, the employees stay in the same position more inactive, thus their muscles weaken and they start to have muscle disease. Weaknesses in the muscles have occurred to the formation of postural problems in people. In our study, a smart vest system was developed to detect and control posture disorders. The proposed system is designed to recommend the most suitable exercises to avoid any physical discomforts. It is also aimed to detect hunched posture by collecting data on the person wearing the vest through sensors. Besides, it is encouraged to correct the posture disorder by warning the person audibly during the hunched posture. The experiments conducted with eight participants showed that the proposed system warns the users with necessary posture corrections, proving its potential use.

1. Introduction

The rapid acceleration of technological developments has made our lives easier in many ways, and besides, physical labor has left its place to machine-based work. In the present age machines are used in many professions because of cheap labor costs so that, working activities of people are decreasing day by day [1]. It is seen that the inadequacy of the inspection processes regarding the compliance of the working conditions in the workplaces with the ergonomics rules seriously puts the health of the people at risk. Recently epidemics caused changes in working conditions and forms. With the appearance of COVID-19, most companies demanded their employees to work at the home office and bring flexible office working. In this way, employees have come to a position to work more than before at their current working hours [2]. Even if they have an ergonomic chair at the office, they couldn't find the same environment at home thus physical activities were decreased. Due the increase in the time spent at the computer than usual, the inactivity of the muscles in the waist and neck region increases and weakens and causes posture disorders.

Posture disorder, which is a muscle problem [3], can be encountered in every stage of our life such as growth, aging, working or sports periods. Early interventions to these deformations have been proven to significantly strengthen the healing processes. The factor of recovery in childhood is much stronger than at an earlier stage in life. With today's advancing technology, wearable posture monitoring devices assist in the treatment of these spinal deformities [4-6]. Pandian and Mohanavelu [7] stated that conventional sensors and medical devices are known to be quite difficult to wear for long periods of time as wearables are unusable for physiological monitoring applications. There was a need for better quality monitoring and physiological support in the market. In line with our study, primarily employees and children were targeted. In this context, a smart vest was designed that people can wear comfortably while performing physiotherapeutic movements suitable for their age category. Along with the proposed system, it is also aimed to develop and analyze a smart vest for posture tracking in physiotherapy rehabilitation exercises. People often have to pay a lot of money to be able to do physiotherapeutic exercises and

* Corresponding author. Tel.: *+90-212-498-4854*; Fax: +90-212-465-8308.
E-mail addresses: ozgulgizem@gmail.com *(G.Özgül)*, f.patlar@iku.edu.tr *(F.Patlar Akbulut)*
ORCID: 0000-0003-4130-4310 *(G.Özgül)*, 0000-0002-9689-7486 *(F.Patlar Akbulut)*
DOI: 10.35860/iarej.1018977

cannot go to rehabilitation centers on a regular basis. For this reason, home rehabilitation has various benefits in terms of both the extended effectiveness of health care and relaxation for the patient [8-10]. With the smart vest, people will be able to do their exercises comfortably at home. Reduction of behavioral disorders due to the utilization of smart vest will be a natural result.

In this study, we developed a sensor-based assistive device that not only warns the individual, but also aids to maintain the ideal posture. In order to examine the effectiveness of the smart vest on posture disorder, we tested it during activities such as walking, sitting and running. With this study, it is aimed that individuals with postural disorders can rehabilitate this problem with the help of a wearable system without affecting their daily lives. The major objectives of this study are:

- Developing a low-cost wearable sensor device to monitor posture during daily activities,
- Real-time transmission of posture data via the microcontroller's Bluetooth interface to increase system availability and analyze data simultaneously.
- To gain the habit of correct posture, in the long run, suggest daily exercises based on the postural structure of individuals through a mobile app.

The rest of this paper is organized as follows: Section 2 surveys the related work in the literature, Section 3 explores the proposed system. We present results on the preliminary experiments in Section 4, and conclude in Section 5.

2. Literature Research

The simplest definition of the concept of posture in the medical language can be defined to be the correct standing of the skeletal system [11]. Many factors affect the posture of the body, some of which are; body type, physical habits, genetic structure and muscle balance. Familial factors, structural disorders and habits are determinants of posture in humans. Posture disorders are usually caused by the weakening of the muscles due to improper sitting for a long time. It is necessary to be very carefully perform sports or various activities; otherwise, health problems may occur [12]. The body acquires a proper posture as a result of the harmonious operation of many muscles with the help of its ligaments during movement. While the skeleton is in a normal state, there is a partial hump on the back [13] as shown on Figure 1. Many of existing posture monitoring systems studies include sensor technology. Numerous useful results have been obtained with the employment of sensors and developing technology on products that people use daily. As a result of the rapid development on wearables, studies that establish a direct connection between the human body and smart devices have become widespread [14, 15].

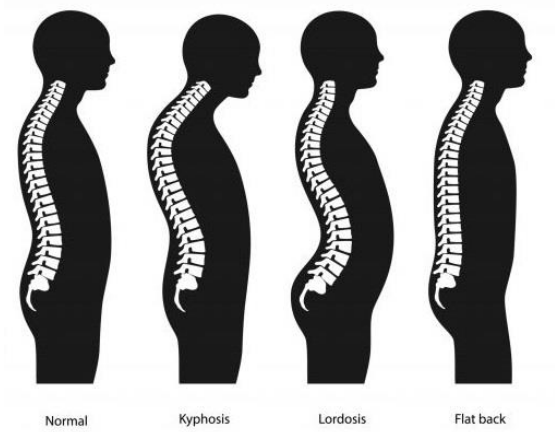

Figure 1. Lateral view of posture positions: the first image is normal or straight posture, the second one displays kyphosis is spine dysfunction, the third image lordosis is the reverse of a hunchback, and in the last one, the spine becomes flat because it loses its natural lower back curve

The fact that such devices communicate with each other and create interfaces on mobile devices using various protocols and wireless technologies such as Bluetooth has made the use of devices popular. Many wearable technology devices and applications have been developed especially for use in the health domain [16, 17]. The most well-known feature of these devices with health applications is that they can measure and monitor motor activities along with various physiological data such as heart rate, amount of oxygen in the blood, body temperature. As a result of long-term desk work neck flattening and back pain are increasing day by day. In particular, health problems occur as a result of many faulty situations such as not using smart devices, increasing erroneous sitting times, falling asleep at the desk [18-21]. As a consequence of these reasons, the technological interest in wearable devices for the prevention of back and low back pain in terms of health applications in the developing market is increasing [22, 23].

Due to the COVID-19 disease, which has affected the whole world in the last two years, it has caused many changes in people's social and business lives. A new lifestyle has been developed at home due to pandemic. With this new lifestyle, institutions have introduced a new working model called working from home by adopting remote working models for people who are in working life. The time spent at the desk increased, while the time spent at the desk increased in relation to this sudden change due to improper implementation of this new approach [24]. The increase in the time spent at the desk has led to the emergence of some symptoms in individuals of all age groups. It has been ensured that chairs, clothes, and wearable devices can be integrated into many different platforms with the positive progress of sensor technology [25-27].

The main motivation of our study is to contribute to improving the quality of life of individuals with postural disorders by performing bodily characteristic analyzes

with correct information and evaluating these data with correct techniques. Health-conscious people think that they need to "fix" their posture and, to a large extent, neck pain, headaches, and especially lower back pain [28]. Precise posture is vital for balance. Correct posture plays a vital role not only in daily life but also in professional life. For example, playing in balance in any sport will strengthen one's abilities in the activity and even increase the duration of the activity. Physical causes of poor posture may include some medical history [29]. In these cases, expert care and diagnosis are necessary to correct negative posture [30].

3. Method

3.1 Wearable Device Design

In our proposed study, the vest's task is to detect and analyze postural imbalance instead of eliminating posture disorder like other vests introduced in the literature. In this context, measurements were collected from sensors placed on different parts of the body. The vest has an adjustable design with back pockets, for ensuring accurate sensor location and measurement. Since it has elastic fabric, people of different body sizes can wear it easily; this is an important factor for the accurate positioning of the sensors during spinal movements and can also be crucial to support long-term usage. In addition, its adhesion to the skin allows us to make a healthier data measurement. Points A, B, C, D, E on the back of the prototype vest shown in Figure 2 below are designated as sensor placement points. A and B are alternative sensor placement locations to be used in measurements to be made from the dorsal region. Likewise, the D and E pockets are designed to be used in choosing the most suitable place on the waist. Zone C pocket is designed to increase the development efficiency of the work. With this pocket, optional sensors such as pulse, temperature, etc. can be placed, and data measurements can be collected, accordingly.

The system consists of a central microcontroller embedded with a number sensors to monitor and analyze users' posture during daily activities. As the central component Arduino UNO R3 processor equipped microcontroller is used to orchestrate the sensor platform. The system is equipped with HC05 Bluetooth module to connect mobile app. In addition, two MPU6050 that have both a 3-axis accelerometer and 3-axis gyroscope integrated on a single chip were employed to monitor and analyze posture. MPU6050 uses I2C communication protocol that enables efficient retrieval of data from both sensors by activating the AD0 addressing pin. This allows measuring rotational velocity or rate of change of the angular position over time, along the X, Y, and Z-axis. The sensors are calibrated to send feedback through the gateway when unequal pressures are sensed between them.

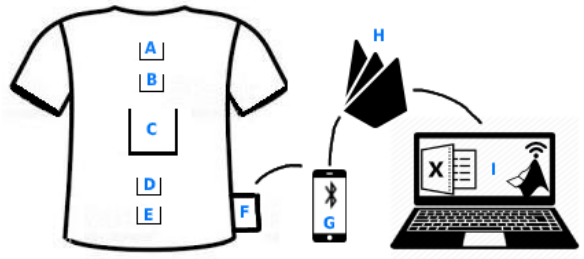

Figure 2. View of the proposed wearable vest and data flow: A, B, C, D, E on the back of the prototype vest shown are designated as sensor placement points

Figure 3. First prototype of posture monitoring vest with multiple pockets on the back to place accelerometer sensors.

Therefore, if the pressure applied to the sensors placed on the back is higher than the set threshold value and as a result, a light on the vest lights up and gives an audible warning with vibrotactile feedback is generated to alert the user. The proposed prototype is powered by a lithium-ion battery and can perform an average of 7 hours of continuous data transfer.

Figure 2 also shows the prototype and data flow lifecycle. Vest data, which is a data fusion from multiple sensors, is processed through sensor platform and becomes usable in real-time. After preprocessing raw data, it is transferred to the Firebase Realtime Database and remains available when application goes offline. We used Firebase to easily access and analyze the stored data. We have conducted a number of experiments to make sure that all services are operational and data transfer are lossless. Figure 3 shows two participants wearing the proposed posture monitoring vest prototype.

Measurements from the back are compared between the two sensors after data preprocessing. As a result of this comparison, the posture disorder tray of the user varies according to the points where the sensors are attached. The sensors used in the system were placed on the back and waist region to determine the hump status. Referencing to the degree of humpback, which is angularly graded, the user is prompted with an audible warning by means of a bell, allowing her/him to correct his posture.

3.2 Mobile Application Design

A mobile application was developed to transfer the collected data and show it to the end user. Android Studio

was preferred as the development interface and Android 11 SDK (API level 30) was used to develop the application. The data collected during the day and during the activity is stored in the Firebase database and reported via the mobile app. Android app uses Bluetooth connection, to discover, connect and communicate with the vest. Figure 4 shows the interfaces of the application.

We aimed for the application to use data according to different activities such as walking, sitting, running etc. to be performed at different times of the day. The system also keeps demographic information of the user such as age, height, weight, and gender.

We have developed interfaces (Figure 5) to control user's movements and provide postural balance. If the user wants to learn the postural balance in the sitting position, by clicking the *Good Sitting* button, she/he can obtain many information such as the appropriate page position, the angular balance of the body and the upright state, both verbally and visually [31]. Other tabs show the right and wrong directions of the walking and running pole. It also includes verbal narration and provides a clear physical therapy support through visual explanations. The accelerometer on the smart vest transmits the information of linear changes in three planes. In this way, both the curvatures of the back and the movement of the body are detected. In order to determine the posture disorder, the measured data are compared with the threshold values that we define as correct posture. Following that, the slopes in the back area can be determined and posture suggestion is made.

4. Experimental Results

While most of the wearable devices in the literature promise potential use in a broad variety of clinical applications, the most prominent challenge is the lack of validation of these sensors. For this reason, the studies first go through the stages of prototype designs and testing, so that the devices are pre-verified. We also conducted a preliminary study to validate the use of the prototype we developed as part of the study for long-term postural monitoring and improvement. Larger and longer-term validation studies are needed following the study.

Traditionally, several tests are performed in hospitals for preliminary diagnosis for patients with postural disorders. During pandemic, the hospital environment is thought to be dangerous for patients [32]. By using smart wearable vests, it is determined which tests should be done to patients in hospitals. The data of the movements of the participants were displayed and analyzed through the developed mobile application. Recommended analyzes consist of three different activities such as sitting, running and walking tests. The experiments were performed by eight subjects, five females and three males aged between 18 and 51.

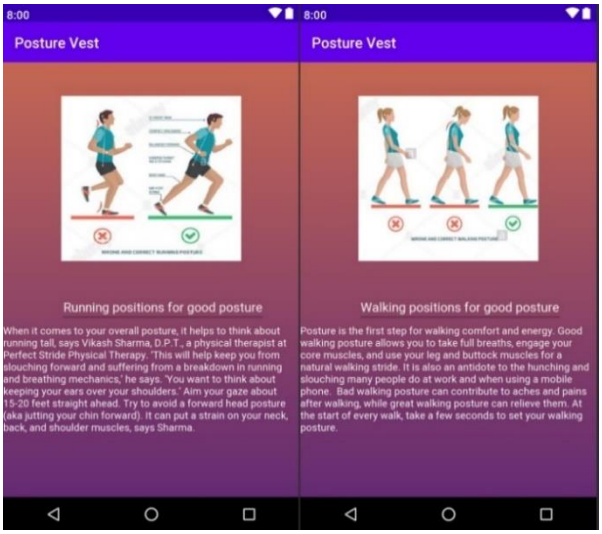

Figure 4. Sample view from the mobile application that includes right and wrong directions of the walking and running activities

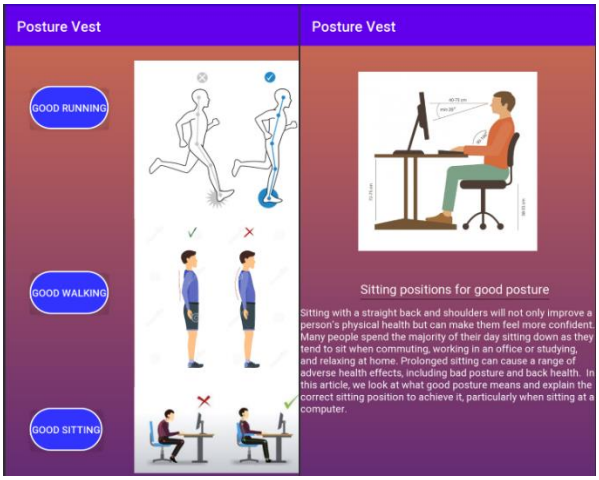

Figure 5. Correct posture suggestions and explanations for different activities

Three of the females and one male were the scoliosis patient; the remaining participants did not declare any back condition or any other treatment. A total of 720 minutes of data were obtained by recording 30 minutes of each activity. We gathered 216000 data points from each sensor with a 5Hz sample rate. In order to determine the sitting positions; head control, trunk control, and foot control were performed. In the sitting tests, we observed that 70% of the participants take the warning system as a basis and change their posture within 5 seconds. When we evaluated the posture of the people during walking with the walking test, we found that the reaction times of the participants decreased by 3 to 5 seconds compared to sitting position. The data we measured from the participants at 12ms intervals showed deterioration in signal during walking and more noisy data than sitting activity. Running test results also have noisy data comparable to walking results. However, we observed 30% less hunched posture during walking and running (Figure 6).

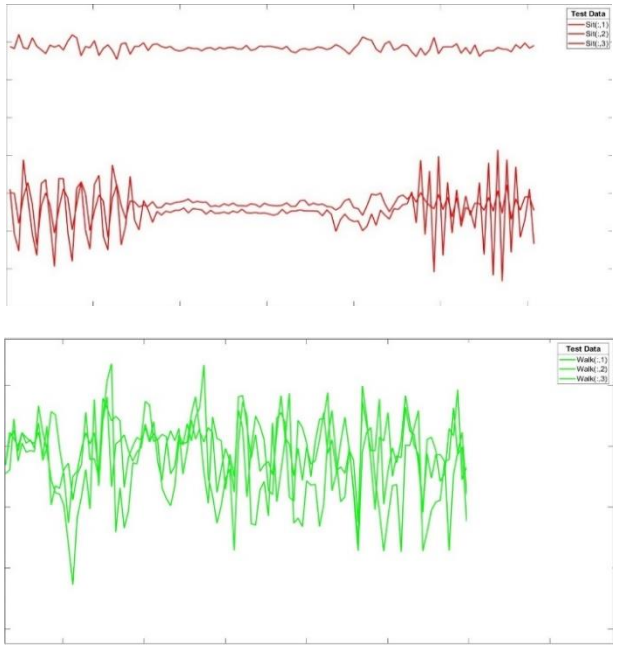

Figure 6. Sample sensor data from sitting and walking activities

Because of COVID-19 pandemic and its limitations, the experiment analyze phase is conducted with limited number of users. Besides, personal information such as height, weight, age and gender of the users were not taken into account. As this study will continue, demographic information will be taken into account in the second version of the vest. With initial prototype, we aimed to develop services that will rehabilitate scoliosis with audible stimuli. In case of regular use, the main goal is to make the user a habit of correct posture.

5. Conclusions

The gradual increase in epidemics such as Covid-19, shows us that people are less likely to reach doctors and health institutions during lockdowns. In addition, there is an inverse correlation between the increasing number of patients in hospitals and the number of health workers. Healthcare professionals can allocate less time to other patients, as they give priority to patients affected by the viruses during epidemic periods. For this reason, the treatment period of the patients is postponed to a later date and the recovery period of the patients may be extended. Today, the hospital-centered treatment approach is being replaced by the patient-centered approach. With the mobile health monitoring systems developed today, it has become possible for patients to continue their treatment at home without the need to go to a hospital or health institution. Our study offers a national alternative to research on posture disorders. With the proposed system, sensor readings of people with posture disorders are recorded and analyzed using low-cost stock sensors to support traditional rehabilitation. In this study, the wearable vest system designed has been implemented using wireless network technologies to strengthen interaction with mobile systems. As the continuation of this work, we will focus on improvements for the ergonomics of the smart vest and make it suitable for daily use.

Declaration

The authors declared no potential conflicts of interest with respect to the research, authorship, and/or publication of this article. The authors also declared that this article is original, was prepared in accordance with international publication and research ethics. All procedures and protocols were approved by the ethical committee at Istanbul Kultur University (approval number: 2020.29).

Author Contributions

G. Özgül developed the methodology, performed the analysis and F. Patlar Akbulut supervised and improved the study.

Acknowledgments

The authors would like to thank undergraduate students Y. Aktas and O.Durmus for contributing to the thorough testing and improvement of the system.

References

1. Şen C, Kılıç A, and Öndoğan Z., *Endüstri 4.0 ve Moda Sektöründeki Uygulamaları*. Turkish Journal of Fashion Design and Management, 2020. **2**(2): p. 53-65 (in Turkish).
2. Vural Ö, Eler S, and Güzel N.A., *Masa Başı Çalışanlarda Fiziksel Aktivite Düzeyi ve Yaşam Kalitesi İlişkisi*. SPORMETRE Beden Eğitimi ve Spor Bilimleri Dergisi, 2010. **8**(2): p. 69-75 (in Turkish).
3. Hamera, E., Goetz, J., Brown, C., and Van Sciver, A., *Safety considerations when promoting exercise in individuals with serious mental illness*. Psychiatry research, 2010. **178**(1): p. 220-222.
4. Cancela, J., Pastorino, M., Arredondo, M. T., Nikita, K. S., Villagra, F., and Pastor, M. A., *Feasibility study of a wearable system based on a wireless body area network for gait assessment in Parkinson's disease patients*. Sensors, 2014. **14**(3): p. 4618-4633.
5. Puranik, A., Kanthi, M., and Nayak, A. V., *Wearable device for yogic breathing with real-time heart rate and posture monitoring*. Journal of Medical Signals and Sensors, 2021. **11**(4): 253.
6. Koçak O, Kaya H, and Üncü Y. *İnsan bilgisayar etkileşimi ile postür analizi ve uyarıcı cihazının geliştirilmesi*. in Sağlık & Bilim: Medikal Araştırmalar. 2021. Efe Akademi, p. 53-62 (in Turkish).
7. Pandian, P. S., Mohanavelu, K., Safeer, K. P., Kotresh, T. M., Shakunthala, D. T., Gopal, P., and Padaki, V. C.Smart, *Vest: Wearable multi-parameter remote physiological monitoring system*. Medical engineering & physics, 2008. **30**(4): p. 466-477.
8. Çalışkan, T. and Esen, H., *Yaşlanan nüfus gereksinimlerine yönelik: evde sağlik hizmetleri 2020 yılı değerlendirmesi eğitim araştırma hastanesi örneği*. Avrasya Sosyal ve Ekonomi Araştırmaları Dergisi, 2021. **8**(3): p. 514-522 (in Turkish).

9. Akbulut, F. P., Akan, A., *Smart wearable patient tracking systems*. in *2015 Medical Technologies National Conference (TIPTEKNO)*, IEEE, 2015. Bodrum, Muğla: p. 1-4.
10. Akbulut, F. P., Özgür, Ö., and Cınar, I., *e-Vital: A wrist-worn wearable sensor device for measuring vital parameters.* in *2019 Medical Technologies Congress (TIPTEKNO)*, IEEE, 2019. Kuşadası, İzmir: p. 1-4.
11. Ercan D.H., *Çocukluk Çağından İtibaren Görülen Postür (Duruş) Bozuklukları*, [cited 2020 21 October]; Available from: https://montessori.kapadokya.edu.tr/makaleler/cocukluk-cagindan-itibaren-gorulen-postur-durusbozukluklari (in Turkish).
12. Külcü, D. G., Gülşen, G., and Altunok, E. Ç., *Short-term efficacy of pulsed electromagnetic field therapy on pain and functional level in knee osteoarthritis: a randomized controlled study*. Archives of Rheumatology, 2009. **24**(3): p. 144-148.
13. Tlili, F., Haddad, R., Bouallegue, R., and Shubair, R., *Design and architecture of smart belt for real time posture monitoring*. Internet of Things, 2022. **17(**100472): p. 1-12.
14. Shi, Q., Dong, B., He, T., Sun, Z., Zhu, J., Zhang, Z., and Lee, C., *Progress in wearable electronics/photonics—Moving toward the era of artificial intelligence and internet of things*. InfoMat, 2020. **2**(6): p. 1131-1162.
15. Heo, J. S., Eom, J., Kim, Y. H., and Park, S. K., *Recent progress of textile-based wearable electronics: a comprehensive review of materials, devices, and applications*. Small, 2018. **14**(3): 1703034.
16. Song, Y., Min, J., Yu, Y., Wang, H., Yang, Y., Zhang, H., and Gao, W., *Wireless battery-free wearable sweat sensor powered by human motion*. Science advances, 2020. **6**(40): eaay9842.
17. Seneviratne, S., Hu, Y., Nguyen, T., Lan, G., Khalifa, S., Thilakarathna, K., ... and Seneviratne, A., *A survey of wearable devices and challenges*. IEEE Communications Surveys & Tutorials, 2017. **19**(4): p. 2573-2620.
18. Zhang, J., Zhang, H., Dong, C., Huang, F., Liu, Q., and Song, A., *Architecture and design of a wearable robotic system for body posture monitoring, correction, and rehabilitation assist*. International Journal of Social Robotics, 2019. **11**(3): p. 423-436.
19. Park, J. H., Kang, S. Y., Lee, S. G., and Jeon, H. S., *The effects of smart phone gaming duration on muscle activation and spinal posture: Pilot study*. Physiotherapy theory and practice, 2017. **33**(8): p. 661-669.
20. Yeom, H., Lim, J., Yoo, S. H., and Lee, W., *A new posture-correcting system using a vector angle model for preventing forward head posture*. Biotechnology & Biotechnological Equipment, 2014. **28**(sup1): p. 6-13.
21. Low, E., Sam, T. H., Tee, K. S., Rahim, R. A., Saim, H., Zakaria, W. N. W., ... and Soon, C. F., *Development of a wireless and ambulatory posture monitoring system*. International Journal of Integrated Engineering, 2020. **12**(2): p. 170-176.
22. Seneviratne, S., Hu, Y., Nguyen, T., Lan, G., Khalifa, S., Thilakarathna, K., ... and Seneviratne, A., *A survey of wearable devices and challenges*. IEEE Communications Surveys & Tutorials, 2017. **19**(4): p. 2573-2620.
23. Ardito, M., Mascolo, F., Valentini, M., and Dell'Olio, F. Low-Cost Wireless Wearable System for Posture Monitoring. Electronics, 2021. **10**(21): p. 2569.
24. Rahmati-Ahmadabad, S., and Hosseini, F., *Exercise against SARS-CoV-2 (COVID-19): Does workout intensity matter? (A mini review of some indirect evidence related to obesity)*. Obesity medicine, 2020. **19(**100245): p. 1-3.
25. Zhang, J., Zhang, H., Dong, C., Huang, F., Liu, Q., and Song, A., *Architecture and design of a wearable robotic system for body posture monitoring, correction, and rehabilitation assist*. International Journal of Social Robotics, 2019. **11**(3): p. 423-436.
26. Ardito, M., Mascolo, F., Valentini, M., and Dell'Olio, F. *Low-Cost Wireless Wearable System for Posture Monitoring*. Electronics, 2021. **10**(21): p. 2569.
27. Zhao, Y., You, Y., *Design and data analysis of wearable sports posture measurement system based on Internet of Things*. Alexandria Engineering Journal, 2021. **60**(1): p. 691-701.
28. Salamon, M., *Does It Hurt When I Do This?: An Irreverent Guide to Understanding Injury Prevention and Rehabilitation*. 2021, Rowman & Littlefield Publishers.
29. Kaynak, K. Ö., Uluğtekin, N. M., *Çalışma ortamındaki fiziksel faktörlerin ergonomik analizi :Dokuz Eylül Üniversitesi Hastanesi Örneği*. Mühendislik Bilimleri ve Tasarım Dergisi, 2017. **6**(1): p. 319-325 (in Turkish).
30. Karakuş, S., Kılıç, F., *Postür ve sportif performans*. Kastamonu Eğitim Dergisi , 2006. **14** (1): p. 309-322.
31. Demirci, F. B., *Sağlıklı bireylerde oturmada farklı ayak pozisyonlarının rahatsızlık hissi, ağırlık aktarımı ve postür üzerine biyomekanik etkileri* 2020, İnönü University: Turkey. p. 35 (in Turkish).
32. Yücesan, b., Özkan, Ö., *Covid 19 pandemi sürecinin sağlık yönetimi açısından değerlendirilmesi*. Avrasya Sağlık Bilimleri Dergisi, 2020. **3**(covid-19): p. 134-139 (in Turkish).

Available online at www.dergipark.org.tr/en

INTERNATIONAL ADVANCED RESEARCHES
and
ENGINEERING JOURNAL

Journal homepage: www.dergipark.org.tr/en/pub/iarej

e-ISSN: 2618-575X

International Open Access

Volume 06
Issue 01

April, 2022

Research Article

Implementation and evaluation of a comprehensive Li-Fi system using Matlab/Simulink

Ahmet Fetullah Yilmaz [a], ***Indrit Myderrizi*** [b,*] ***and Betul Damla Kalfa*** [a]

[a]*Istanbul Gelisim University, Faculty of Engineering and Architecture, Department of Electrical and Electronics Engineering, Istanbul, 34310, Turkey*
[b]*Istanbul Gelisim University, Faculty of Applied Sciences, Department of Avionics, Istanbul, 34315, Turkey*

ARTICLE INFO

Article history:
Received 27 October 2021
Accepted 29 January 2022
Published 15 April 2022

Keywords:
Convex lens
Li-Fi (Light fidelity)
Mirror
Simulink model
Wireless communication
Wi-Fi (Wireless fidelity)

ABSTRACT

Li-Fi technology is a type of visible light communication that uses LEDs as a data transmission source. Li-Fi is expected to occupy an important place in wireless network technology by providing high-speed internet access and having high bandwidth. It may be a common technology to provide internet access instead of Wi-Fi in places where radio waves are inconvenient, such as hospitals and airplanes. In this paper, a comprehensive Li-Fi system model implemented using Simulink® is proposed and evaluated. The model is equipped with a mirror and a thin convex lens to increase the efficiency of the Li-Fi system by reflecting and focusing the light beam emitted from the LEDs. The result obtained from the evaluation test shows that the output signal from the model of the proposed Li-Fi system is much higher than that of the basic Li-Fi system. Thus, using the proposed comprehensive model, more efficient Li-Fi systems can be realized.

1. Introduction

With the development of technology, the internet has become a part of daily life. Internet use has turned out to be more common as computers, phones, televisions, and many devices have Wi-Fi receivers. Wi-Fi uses radio waves to transmit data. Radio waves correspond to the frequency range of 3 Hz to 300 GHz in the electromagnetic spectrum. With the increasing use of radio waves, when this bandwidth starts to fill up, the data transfer rate of Wi-Fi devices slows down [1]. There are also places where radio waves are not suitable. Wi-Fi use is not appropriate for hospitals as the health of people exposed to radio waves is negatively affected (tumor, cancer, etc.). At the same time, radio waves can interfere with the equipment used in hospitals. Radio waves are not suitable for use not only on hospital equipment but also on airplanes due to safety concerns and device interference [2-3].

As a solution to these limitations, Li-Fi (Light Fidelity) technology is recommended. Li-Fi technology, proposed by the German physicist Harald Haas, sends data via a light-emitting diode (LED) bulb that flashes too fast for the human eye [4]. Using the visible light spectrum to transmit data, Li-Fi technology corresponds to a frequency range of 430 THz to 790 THz. This means that the size of the infrared and visible light spectrum together is approximately 2600 times the size of the entire radio frequency spectrum of 300 GHz [5]. Consequently, this wide bandwidth range is considered an alternative to the limited bandwidth of radio waves [6]. Li-Fi is also advantageous in terms of internet speed. Researchers at the University of Oxford have achieved bidirectional speeds of 224 Gbps. In the study, LEDs and receivers working with different fields of view are used and internet connection speeds of 224 Gbps and 112 Gbps are achieved for 60° and 36° wide viewing areas at a distance of 3 meters. These speeds are well above those offered by modern Wi-Fi technology (approximately 600 Mbps) [1]. Thanks to the Li-Fi system's use of visible light, it does not cause interference to devices. In addition, since no light can pass through the walls in a closed environment, internet access cannot be provided to other areas. Although this may seem like a negative effect, it is important from a safety point of view. Li-Fi's usage areas are very advantageous compared to Wi-Fi in terms of high bandwidth, harmless to human health and speed [7]. All in all, Li-Fi is an advantageous alternative to Wi-Fi.

* Corresponding author. Tel.: +0-212-422-7000; Fax: +0-212-422-7401.
E-mail addresses: afyilmaz@gelisim.edu.tr *(A. F. Yilmaz)*, imyderrizi@gelisim.edu.tr *(I. Myderrizi)*, bdkalfa@gelisim.edu.tr *(B. D. Kalfa)*
ORCID: 0000-0002-8816-1380 *(A. F. Yilmaz)*, 0000-0002-2112-7911 *(I. Myderrizi)*, 0000-0002-3012-2768 *(B. D. Kalfa)*
DOI: 10.35860/iarej.1015638

The basic principle of data transmission is to turn the light on and off. In other words, digital '1' information is transmitted when the light is turned on and digital '0' when the light is turned off. The intensity of the LED is modulated so fast that the human eye cannot perceive it and therefore the light appears constant [8-9].

In recent researches several models to describe and simulate the Li-Fi systems are developed. In [10], a Li-Fi model including a standard transceiver circuit is developed using MATLAB®. Through simulations, Wi-Fi and Li-Fi technology are compared in terms of data transfer rate, packet loss, delay data and it is seen that Li-Fi technology is superior. In [11], Li-Fi is introduced as a communication system with its modulation techniques, and analysis of the system modelled with the Simulink® block diagrams is performed. In [12], Li-Fi system with ambient noise is modelled in Optisystem 15. The ambient light effects on the Li-Fi communication link and the performance of the receiver under ambient noise power due to different sources is evaluated through simulations. In [13], a prototype model for a Li-Fi health monitoring system is created to transmit data from a patient-held FBG sensor to an optical receiver installed in the patient's ceiling room via different propagation links. In [14], a model of a Li-Fi system for transmitting audio signals is considered and designed with a minimum number of electrical elements.

The aim of this paper is implementation and evaluation of a more advanced and efficient model for Li-Fi system. To increase efficiency over previous Li-Fi models [10-11], various components such as mirrors and lenses are added to the Simulink® model of the Li-Fi system. As the light emitted from the LED using a mirror and/or lens is focused on the photodiode, an increase in the magnitude of the output signal is expected [10, 15].

The paper is organized as follows: In Section 2 basic concepts about the Li-Fi architecture and how light interacts with mirrors and lenses are briefly presented. In Section 3 Simulink® models developed for Li-Fi system are given, with details. Performance verification of the implemented models through simulations are evaluated in Section 4. Finally, in Section 5, conclusions are drawn.

2. Basic Concepts

2.1 Li-Fi Architecture

Li-Fi can be thought of as light-based Wi-Fi. In short, Li-Fi uses light with the help of high-speed switchable LEDs instead of radio waves to transmit data [16].

A basic Li-Fi system consists of two main parts. The first part, called the transmitter circuit, includes the converter that converts the incoming signal into binary information in the form of 1s and 0s, the driver circuit used to switch the LED, and the LEDs used to transmit information. The second part, called the receiver circuit, includes a photodiode used to detect information coming from the LED, an amplifier circuit used to amplify the detected signal, and a converter circuit that converts the obtained information to its original state. The receiver and transmitter circuits are physically separate and distant from each other. However, an empty optical communication channel (Li-Fi channel) connects these two main parts [17-19]. The block diagram of the basic Li-Fi system is shown in Figure 1.

As visible light passes through the communication channel, its intensity decreases inversely with the square of the distance, causing the signal to the receiver to be very low. As a photodiode moves away from the light source (LED), the light falling on the photodiode per unit time decreases. The inverse square law formula is applied as shown below,

$$\frac{I_1}{I_2} = \frac{d_2^2}{d_1^2} \tag{1}$$

where I_1 and I_2 are the light intensities of LED at distances d_1 and d_2 from the photodiode, respectively.

The communication channel can contain multiple sources of optical noise. During the daytime, the most important source of noise is the sun. Other noise sources are represented by transmitters in visible light communication or any light source with or without data transmission capabilities. In outdoor visible light communication applications, the unpredictability is even greater due to weather. The water particle caused by rain, snow, or heavy fog can cause the light containing the data to scatter, affecting the visible light communication link [20].

2.2 Interaction of Light with Mirror and Lens

Mirrors and glossy surfaces reflect most of the light falling on them according to the laws of reflection. The reflection event is illustrated in Figure 2.

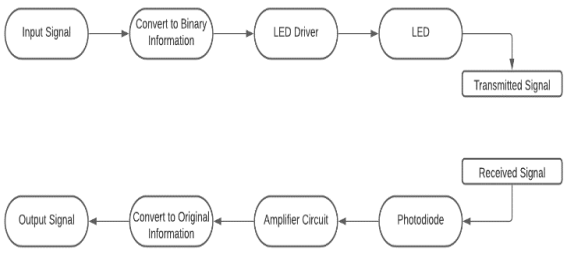

Figure 1. Block diagram of the basic Li-Fi system

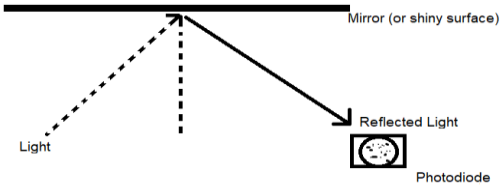

Figure 2. Illustration of specular reflection

In a Li-Fi system with mirror, incoming light is reflected from the surface and directed to the photodiode. Snell's law describes the reflection and refraction phenomena of light. According to Snell's law, the ratio of the sines of the angles of incidence and refraction is equivalent to the ratio of phase velocities in the two media, or equivalent to the reciprocal of the ratio of the indices of refraction:

$$\frac{sin\theta_1}{sin\theta_2} = \frac{v_1}{v_2} = \frac{n_2}{n_1} \quad (2)$$

where θ_1 is the angle of incidence and θ_2 is the angle of refraction, both measured from the normal of the boundary, v_1 and v_2 are the velocities of incoming and outgoing lights, n_1 and n_2 are the refractive indices of the respective mediums [21].

Any incident ray traveling parallel to the principal axis of a converging lens is refracted through the lens and passes through the focal point F' on the opposite side of the lens. The diagram in Figure 3 shows the behavior of two incident rays approaching parallel to the principal axis. In this case, the point where the two rays converge is known as the focal point F' of the lens. In a Li-Fi system, the photodiode has a specific viewing angle. It cannot see light rays that are out of this field of view. If the photodiode is placed at the F' point, the light intensity falling on the photodiode increases [21].

Lenses consist of two curvilinear refractive surfaces. The refractive power P or the reciprocal of the focal length f (distance between lens and focal point) of a lens in air is given by the lensmaker's general equation:

$$P = \frac{1}{f} = (n-1)\left[\frac{1}{R_1} - \frac{1}{R_2} + \frac{(n-1)d}{nR_1R_2}\right] \quad (3)$$

where n is the index of refraction of the lens material, d is the distance along the optical axis between the two surfaces of the lens, known as the thickness of the lens, and R_1 and R_2 are the radii of curvature of the two surfaces.

3. Implementation of a Comprehensive Li-Fi System Using Simulink®

3.1 Simulink® Model of the Basic Li-Fi System

Simulink® model for the basic Li-Fi system illustrated in Figure 1 is shown in Figure 4.

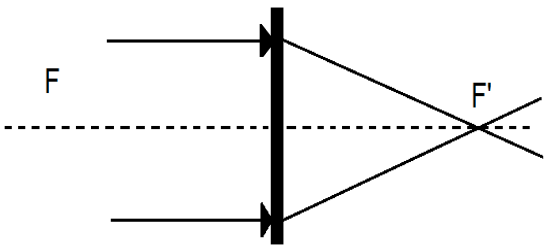

Figure 3. Movement of light through a converging lens [19]

The model consists of a transmitter part involving a square wave generator used to represent the conversion of the input signal to binary information, a switching circuitry used to drive the LED, and the LED transmitting the information through light. Following the transmitter an optical channel serving as the medium through which the light propagates, and used to transmit the information to the receiver's side, is added. Next, a receiver part involving a photodiode that converts optical power to electrical signal and an amplifier circuit used to amplify the converted electrical signal is placed [10-11].

3.2 Simulink® Model of the Li-Fi System with Mirror

Simulink® model for the Li-Fi system with mirror is shown in Figure 5. The model includes the model developed for the basic Li-Fi system in the previous section, and a mirror model represented by a Matlab® function arranged according to Equation (2), which directs light from the LED to the photodiode. While modeling the mirror in Simulink®, the refractive index of the air medium, the refractive index of the mirror used to reflect the light, and the angle of the mirror are selected as 1, 1.75 and 30°, respectively. The values used for the simulation are based on the 300-1500 lx value range that the research in [22] provides for adequately illuminating an office with LEDs and the angles of the mirrors used to increase the performance of the system. Values may vary in the model, depending on the need and application.

3.3 Simulink® Model of the Li-Fi System with Convex Lens

While the light produced by the LED spreads to all parts of the environment (room, office, airplane cabin, etc.), it does not spread evenly at every point, and the photodiode can detect the incoming data at a certain viewing angle. Although not all of the emitted light can be collected on the photodiode using a thin convex lens, light outside the field of view can be focused onto the photodiode. Simulink® model for the Li-Fi system with thin convex lens is shown in Figure 6. The model includes the model developed for the basic Li-Fi system, and a thin lens model represented by a Matlab® function arranged according to Equation (3), which focuses the scattered light on the photodiode. Values may vary in the model, depending on the need and application.

3.3 Simulink® Model of the Comprehensive Li-Fi System

When the thin convex lens and mirror are used simultaneously, the scattered lights are diverted and more light is focused on the photodiode. Because in this case, the light reflected from the mirror and the thin convex lens falls directly on the photodiode. Thus, the signal to be obtained at the output of the system is expected to increase even more. Simulink® model incorporating both a thin convex lens and a mirror, for the comprehensive Li-Fi system, is shown in Figure 7.

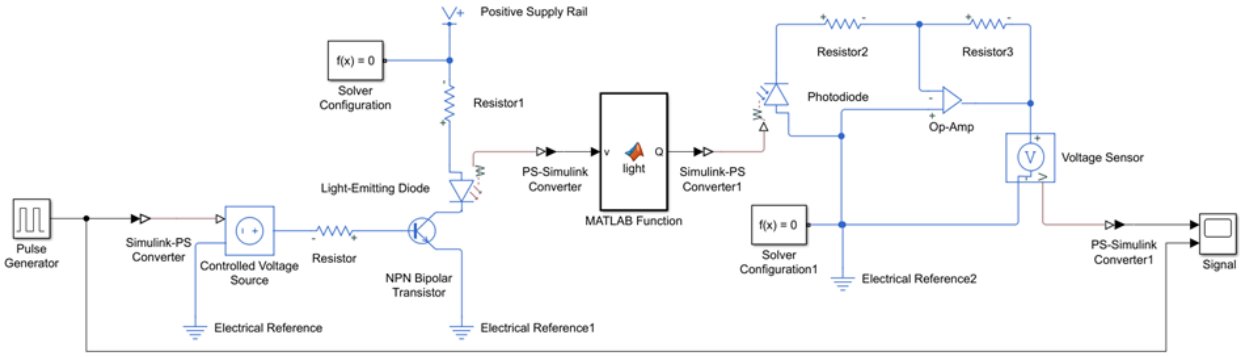

Figure 4. Simulink® model of the basic Li-Fi system

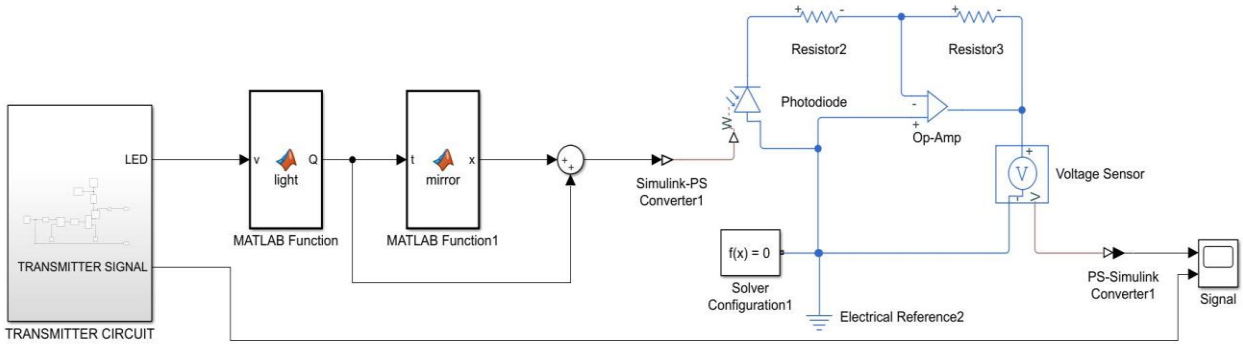

Figure 5. Simulink® model of the Li-Fi system with mirror

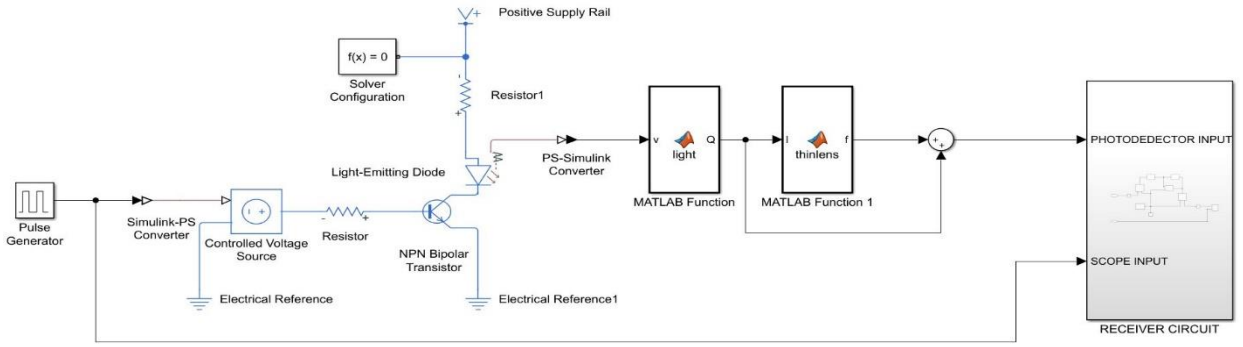

Figure 6. Simulink® model of the Li-Fi system with thin convex lens

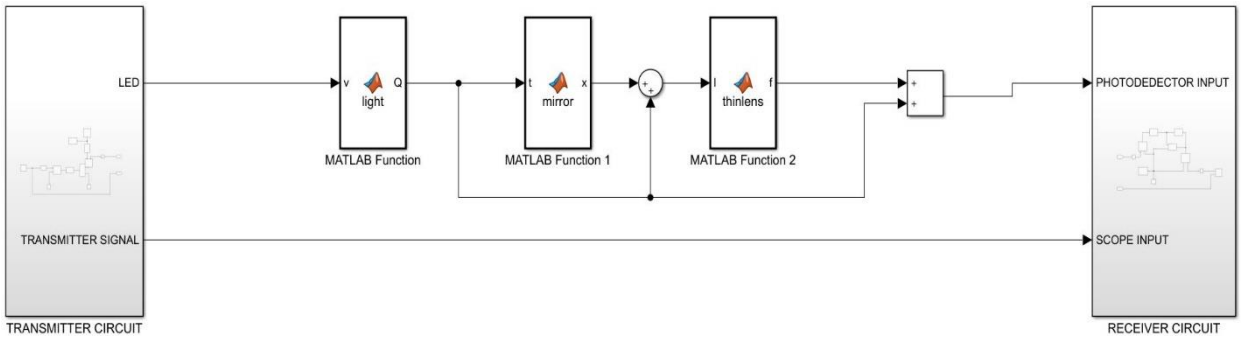

Figure 7. Simulink® model of the proposed comprehensive Li-Fi system

4. Performance Verification

The implemented models are evaluated through simulations. The performance of the models is examined by applying an input signal with amplitude of 3.3 V and obtaining the output signal. Figure 8 shows the waveforms of the transmitter and receiver (input and output signals of

the system) signals for Simulink® model of the basic Li-Fi system.

As seen in Figure 8, the 3.3 V signal sent from the transmitter circuit is received as 1.213 V in the receiver circuit.

Figure 9 shows the waveforms of the transmitter and receiver (input and output signals of the system) signals for Simulink® model of the Li-Fi system with mirror.

As seen in Figure 9, the 3.3 V signal sent from the transmitter circuit is received as 1.396 V in the receiver circuit. The signal obtained at the receiver is increased by the effect of the mirror.

Figure 10 shows the waveforms of the transmitter and receiver (input and output signals of the system) signals for Simulink® model of the Li-Fi system with thin convex lens.

As seen in Figure 10, the 3.3 V signal sent from the transmitter circuit is received as 1.549 V in the receiver circuit. With the focusing effect created by the thin convex lens, the signal obtained at the receiver is increased.

Figure 11 shows the waveforms of the transmitter and receiver (input and output signals of the system) signals for Simulink® model of the proposed comprehensive Li-Fi system.

As seen in Figure 11, the 3.3 V signal sent from the transmitter circuit is received as 2.687 V in the receiver circuit. By using both the mirror and the thin convex lens in the model at the same time, the signal obtained at the receiver's output is significantly increased.

Comparison of the implemented Li-Fi system Simulink® models in terms of output signal is given in Table 1.

As a result, when the proposed models are compared, the output signal increases by about 15% in the Li-Fi system with mirror, about 28% in the Li-Fi system with thin convex lens, and about 122% in the comprehensive Li-Fi system, compared to the basic Li-Fi system. In addition, the comprehensive Li-Fi system outperforms the Li-Fi system with mirror and the Li-Fi system with thin convex lens by 93% and 74%, respectively. Although a unity gain amplifier is used in the mirror and convex lens model, a higher amplitude signal is obtained compared to the study in [11] that uses an amplifier with gain.

Table 1. Comparison of the implemented Li-Fi system Simulink® models

Model	Transmitted Signal(V)	Received Signal(V)
Basic	3.3	1.213
Mirror	3.3	1.396
Convex Lens	3.3	1.549
Comprehensive	3.3	2.687

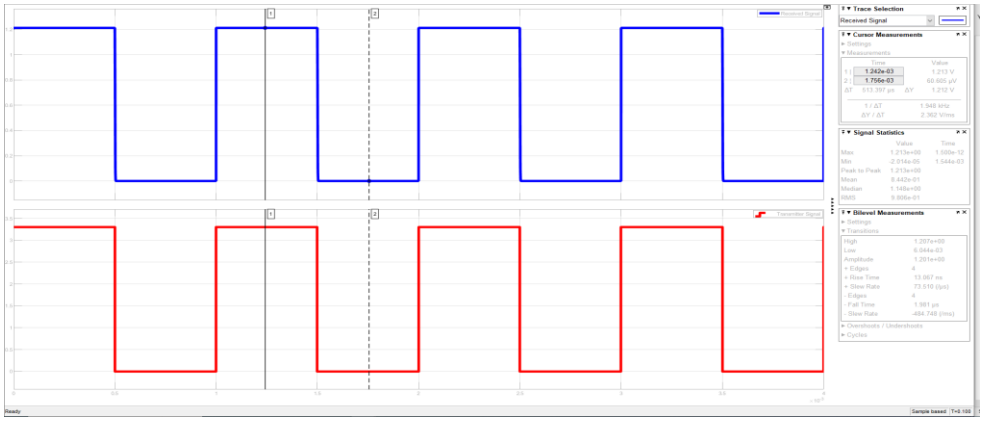

Figure 8. Transmitted and received signals for Simulink® model of the basic Li-Fi system

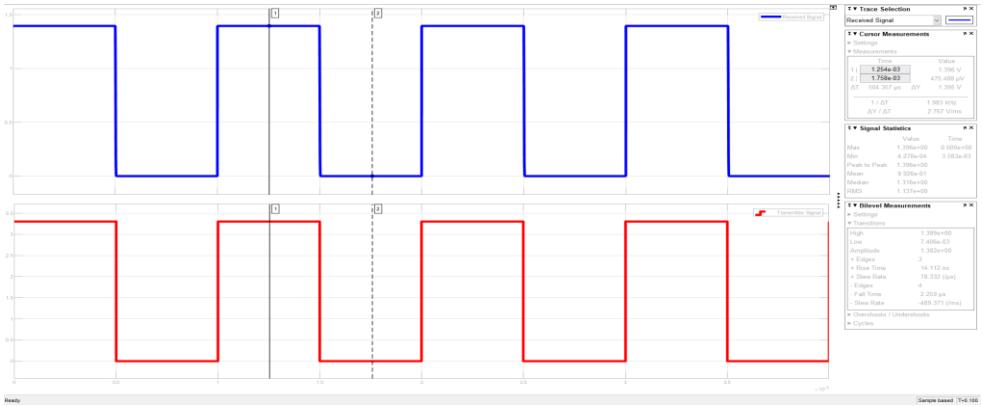

Figure 9. Transmitted and received signals for Simulink® model of the Li-Fi system with mirror

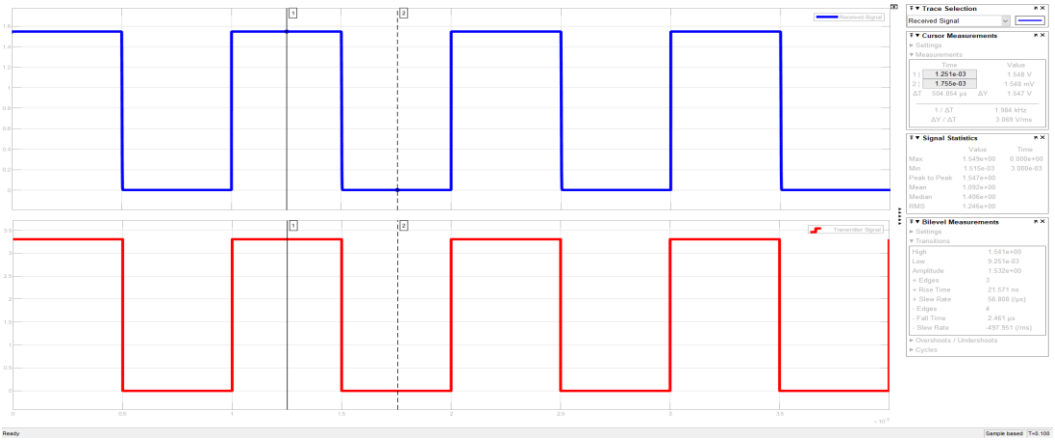

Figure 10. Transmitted and received signals for Simulink® model of the Li-Fi system with thin convex lens

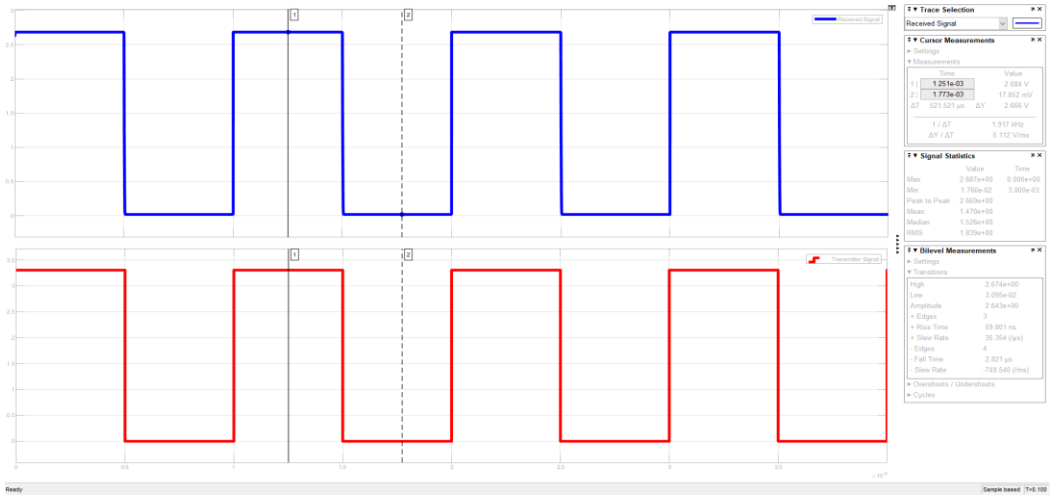

Figure 11. Transmitted and received signals for Simulink® model of the comprehensive Li-Fi system

5. Conclusions

In this paper, a comprehensive Li-Fi system model is developed. Prior to the proposed comprehensive model, two Simulink® models with mirror and thin convex lens, respectively, are implemented for the Li-Fi system. The performance of the models is compared with the model of the basic Li-Fi system existing in the literature, in terms of output signal. The proposed comprehensive model shows a very high performance. An increase of 122% is observed in the output signal compared to the basic model. In addition, the output signal obtained in mirror-only and thin convex lens-only models shows an increase of 15% and 28%, respectively, compared to the basic model. The proposed model lays the groundwork for further improving the efficiency of existing Li-Fi systems and offers a new approach for highly efficient applications in Li-Fi technology.

Declaration

The authors declared no potential conflicts of interest with respect to the research, authorship, and/or publication of this article. The authors also declared that this article is original, was prepared in accordance with international publication and research ethics, and ethical committee permission or any special permission is not required.

Author Contributions

I. Myderrizi, A. F. Yilmaz and B. D. Kalfa proposed and developed the models. A. F. Yilmaz performed the simulations. I. Myderrizi and A. F. Yilmaz wrote the manuscript. I. Myderrizi supervised and improved the study.

Acknowledgment

This work has been funded by Istanbul Gelisim University Scientific Research Projects Application and Research Center (Project number: KAP-141220-IM), Turkey.

Nomenclature

Li-Fi	: Light Fidelity
Wi-Fi	: Wireless Fidelity
LED	: Light Emitting Diode
FBG	: Fiber Bragg Grating
I	: Light intensity
d	: Distance

θ : Angle of incidence
v : Velocity
n : Refractive index
P : Refractive power
f : Focal length
R : Radii of curvature
V : Volt

References

1. Sarkar, A., S. Agarwal, and A. Nath, *Li-Fi technology: data transmission through visible light.* International Journal of Advance Research in Computer Science and Management Studies, 2015. **3**(6): p. 3-10.
2. Pall, M. L., *Wi-Fi is an important threat to human health.* Environmental Research, 2018. 164: p. 405-416.
3. Leba, M., S. M. Riurean, and A. C. Ionica, *Li-Fi – the path to a new way of communication*, in CISTI2017: Lisbon, Portugal. p. 1-6.
4. Sharma, R. R., Raunak, and A. Sanganal, *Li-Fi technology: transmission of data through light.* International Journal of Computer Technology and Applications, 2014. **5**(1): p. 150-154.
5. Haas, H., *LiFi is a paradigm-shifting 5G technology.* Review in Physics, 2018. **3**: p. 26-31.
6. Khan, L. U., *Visible light communication: applications, architecture, standardization and research challenges.* Digital Communications and Networks, 2017. **3**(2): p. 78-88.
7. Sanusi, J., A. M. Aibinu, S. Adeshina, G. Koyunlu, and S. Idris, *Review of handover in Li-Fi and Wi-Fi networks*, in ICCNCT2019: Coimbatore, India. p. 955-964.
8. Abdalla, A. M., J. Rodriguez, I. Elfergani, and A. Teixeira, *Optical and wireless convergence for 5G networks.* 2019, Wiley-IEEE Press.
9. Albraheem, L. I., L. H. Alhudaithy, A. A. Aljaser, M. R. Aldhafian, and G. M. Bahliwah, *Toward designing a Li-Fi-based hierarchical IoT architecture.* IEEE Access, 2018. **6**: p. 40811-40825.
10. Arinze, S. N., G. N. Onoh, and D. O. Abonyi, *Network performance comparison of light fidelity and wireless fidelity.* International Journal of Advanced Scientific and Techical Research, 2020. **1**(10): p. 14-24.
11. George, R., S. Vaidyanathan, A. S. Rajput, and K. Deepa, *LiFi for vehicle to vehicle communication – a review.* Procedia Computer Science, 2019. **165**: p. 25-31.
12. Pradhan, J., V. K. Kappala, and S. K. Das, *Performance analysis of a Li-Fi system under ambient light conditions*, in NCC2020: Kharagpur, India. p. 1-6.
13. Majeed, A. F. and I. A. Murdas, *Novel design for Li-Fi healthcare monitoring system.* International Journal of Intelligent Engineering&Systems, 2019. **12**(6): p. 59-70.
14. Valkovski, T., and K. Dimitrov, *Low Cost Laboratory Environment for the Use of Optical Methods for Transmission of Audio Signals*, in ICEST2020: Nis, Serbia. p. 65-68.
15. Abid, S. M. T., S. Khabir, M. A. Hasan, A. Saha, and M. Masuduzzaman, *Li-Fi technology: increasing the range of Li-Fi by using mirror.* International Journal of Information Technology and Computer Science, 2019. 11(1): p. 50-57.
16. Raj, B. D., B. S. Rakesh, N. Avinash, K. Balakrishnan, and S. Basavaraju, *Visible spectrum using optical communication.* Perspectives in Communication, Embedded-System and Signal-Processing, 2018. **2**(7): p. 153-156.
17. Goswami, P. and M. K. Shukla, *Design of a Li-Fi transceiver.* Wireless Engineering and Technology, 2017. **8**(4): p. 71-86.
18. Cevik, T. and S. Yilmaz, *An overview of visible light communication systems.* International Journal of Computer Networks and Communications, 2015. **7**(6): p. 139-150.
19. Liu, CB., B. Sadeghi, and E. W. Knightly, *Enabling vehicular visible light communication (V2LC) networks*, in VANET2011: Las Vegas, NV, USA. p. 41-50.
20. Cailean, A., *Etude et realisation d'un systeme de communications par lumiere visible (VLC/LiFi). Application au domaine automobile.* 2014, Optique / photonique. Universite de Versailles Saint-Quentin en Yvelines.
21. Vasan, S., *Basics of photonics and optics.* 2004, Trafford Publishing.
22. Komine, T. and M. Nakagawa, *Fundamental analysis for visible-light communication system using LED lights.* IEEE Transactions in Consumer Electronics, 2004. **50**(1): p. 100-107.

Available online at www.dergipark.org.tr/en

INTERNATIONAL ADVANCED RESEARCHES and ENGINEERING JOURNAL

Journal homepage: www.dergipark.org.tr/en/pub/iarej

e-ISSN: 2618-575X

International Open Access

Volume 06
Issue 01

April, 2022

Review Article

Reduction of operation temperature in SOFCs utilizing perovskites: Review

Nagihan Caylak Delibas [a,*], ***Soudabeh Bahrami Gharamaleki*** [b], ***Masrour Mansouri*** [c] ***and Alighol Niaei*** [b]

[a]*Department of Physics, Faculty of Art & Science, University of Sakarya , Sakarya, Turkey*
[b]*Catalyst and Reactor Research Lab, Department of Chemical Engineering, University of Tabriz, Iran*
[c]*Faculty of Technology and Engineering, Central Branch of Islamic Azad University, Tehran, Iran*

ARTICLE INFO

Article history:
Received 19 July 2021
Accepted 17 March 2022
Published 15 April 2022

Keywords:
Fuel cell
SOFC
Perovskite

ABSTRACT

Fuel cells are electrochemical devices utilized for converting chemical energy to electrical energy. Solid Oxide Fuel Cells (SOFCs) have several advantages over other kinds. For instance, high energy efficiency expanded fuel flexibility, low environmental pollutant emission are the properties of SOFCs that make them superior to other fuel cell types. Due to these special characteristics, SOFCs are gained a great deal of attraction. These fuel cells consist of different main operating parts, a cathode, an anode, and electrolyte which each of them demands special materials to operate with the most efficiency. SOFCs mostly operate in high temperatures (800-1000 °C). Reducing the operating temperature to lower than 600 °C or intermediate temperatures 600-800 °C is one of the methods that can make them more practical devices. Perovskite oxides can be used effectively as all main parts of SOFCs because of their excellent properties like electrical and ionic conductivities, oxygen ion vacancies, great catalytic properties, thermal durability, and chemical stability to decrease the operating temperature. In this review, numerous perovskite-based materials utilized in the anode and the cathode electrodes of SOFCs are investigated in the most recent, advanced, and novel works. The perovskite materials, their properties, and their influence on the fuel cell's performance, and in some cases the sulfur tolerance of the materials when H_2S co-exists in the fuel of the fuel cell are reviewed in this paper Adding different dopants in A-site and B-site of the perovskite oxides is the most effective way to modify the characteristics of the materials. This review can provide great data on the possible perovskite oxides with the capability of enhancing the efficiency of SOFCs by reducing the operating temperature, and their most decisive and significant characteristics, like composition, structure, electrical conductivity, electrochemical and mechanical properties for research groups working on solid oxide fuel cells.

1. Introduction

Fuel cells are efficient devices for conversion of chemical energy to electrical through electrochemical reactions, and among different fuel cells, like polymer electrolyte membrane, molten carbonate, and alkaline fuel cells (Table 1) solid oxide fuel cells (SOFCs) are the promising energy convertor with high efficiency, great fuel flexibility, they can use hydrocarbons, coal syngas, ammonia, and hydrogen, and low pollutant emission [1-4]. SOFCs consist of different parts like anode, cathode, electrolyte, current collectors, interconnectors, and sealants. Nonetheless, all parts are effective on the performance of the fuel cells, three main elements that determine the efficiency of the cell are the porous anode, electrolyte, and porous cathode. Oxidant gas flows into the cathode and the fuel available in the anode electrode, and the reactions happen at the three-phase boundary (TBP) of electrolyte, gas, and electrode interface [5].

* Correspond author. Tel.: *+90-264-295-6095.*
E-mail addresses: caylak@sakarya.edu.tr *(N. Caylak Delibas),* sudabehbahrami68@yahoo.com *(S.B. Gharamaleki),* masrour86@yahoo.com *(M. Mansouri),* ali.niaei@gmail.com *(A. Niaei)*
ORCID: 0000-0001-5752-062X *(N. Caylak Delibas),* 0000-0002-2060-7032 *(S.B. Gharamaleki,* 0000-0002-3277-9894 *(M. Mansouri),* 0000-0001- 5580-4266 *(A. Niaei)*
DOI: 10.35860/iarej.972864

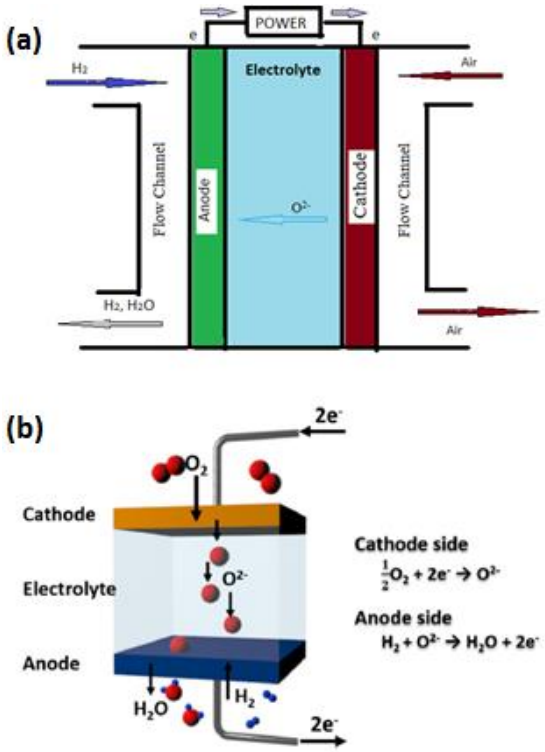

Figure 1. (a) : A schematic picture of SOFC with H_2 as fuel, (b) electrochemical reactions inside the cell [6]

In this process, the oxygen anions travel from the cathode to the anode through the electrolyte and react with the fuel in the anode electrode. As a result, electrons release in anode and go through the outer path to the cathode electrode. This way, chemical energy of the electrochemical reactions turn to electricity. A schematic picture of a solid oxide fuel cell is demonstrated in Figure 1 [6]. Although SOFCs have several advantages which make them excellent devices for electrical energy production, they have some drawbacks. One of the most problematic features of these fuel cells is their operating temperature. SOFCs mostly work at 800-1000 ^oC. Operating in such high temperatures could result in a decreased lifetime of the cell, low compatibility between the components, high thermal degradation of cell's materials, a long time of start-up, and higher costs. Thus, lowering the operating temperature to low temperatures like < 600 ^oC or to intermediate temperatures 600-800 ^oC is essential to address these problems to have the possibility to chooses among various materials, with different characteristics, that can work in lower temperatures without having the problems mentioned above for fuel cell's components used in high temperatures [7-9].

This way, the chance to find the most suitable material for three main parts of the SOFC can enhance and as a result, the efficiency of the fuel cell can increase. However, cathodic polarization increases at lower temperatures, which leads to reduced cell output.

Table 1. Different fuel cells' properties [12]

Fuel Cell	**T (^oC)**	**Electrolyte**	**Transported Ion**	**Efficiency**
Solid Oxide	550-1000	Dense Ceramics	O^{2-}	40-60%
Polymeric Exchange Membrane	60-100	Polymer	H^+	35-45%
Alkaline	50-120	Potassium Hydroxide	OH^-	35-55%
Molten Carbonate	550-650	Molten Carbonates	CO_3^{2-}	45-55%
Phosphoric Acid	180-210	Phosphoric Acid	H^+	35-45%

Due to this issue, the selection of materials for the electrodes is a vital decision and can significantly affect the cell's efficiency [10]. Perovskite-based materials are one of the most appropriate anode and cathode materials for SOFCs because of their excellent characteristics such as super electrical conductivity, catalytic activity, Ferro and piezoelectric, thermal stability, magnetoresistance, mechanical durability, and low cost [11]. In this review, we focused on the perovskite-based materials utilized in the anode and the cathode of SOFCs operating mostly in low or intermediate temperatures. In other words, the perovskite materials, their characteristics, performance, and weaknesses when used as SOFCs' anode and cathode are elaborated in this review paper and the most efficient way to improve the electrochemical properties of the perovskite oxides is introduced. All in all, this paper cold be used as a source to review the features of the perovskites used in SOFCs electrodes to enhance their performances, how to make those perovskite materials, and how to measure the properties of the oxides by the researchers and students working on improving intermediate temperature solid oxide fuel cells.

2. Perovskites

Perovskites have ABO_3 composition formula, but there are other perovskite-based materials such as double perovskites, layered perovskites, and perovskite-like materials. [13,14]. Perovskites have a cubic structure in which the A-site cation's (mostly alkaline earth or rare earth metal cation) coordination number is 12 and the B-site cation's (transition metal cation) coordination number is 6. The B- site cation is often smaller than the A-site cation.

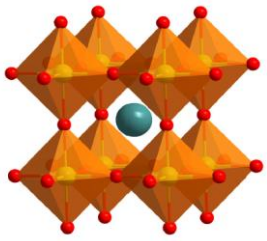

Figure 2. Schemaic of pervoskite structure [7]

A single perovskite's structure is illustrated in Figure 2 [15, 16]. Mixed ionic and electric-conducting perovskites have excellent oxygen ionic and electric conductivity with larger TBP areas that result in enhanced performance of the cell [17, 18]. Numerous studies have been done on the investigation of the synthesis method's effect, the performance of the perovskite-based materials, and their characteristics. . Because of their electrochemical, catalytic properties and various structures, perovskites have numerous applications like being solid oxide fuel cells' components, gas sensors, and high temperature superconductors, magnetic and dielectric materials. Perovskite materials can have different morphologies (Figure 3) [19]. The structure of perovskites can elongate, tilt or rotate due to the decrease of a coordination number, doping, pressure and temperature. Moreover, the distortion from cubic to one of lower symmetry can result in various morphologies such as orthorhombic, tetragonal, and monoclinic structures.

Composition, structure, and chemical bonds in the perovskite explain the features of the oxides. For instance, the thermal expansion coefficient and catalytic activity of the perovskite materials depend on strength of chemical bonds and band structure. Figure 4 demonstrates the dependence of the electronic conductivity to temperature of various $SrTiFeO_3$ (STF) and $SrTiNbO_3$ (STN) perovskites. One can see from this picture that STN perovskites have better conductivity than STFs and temperature does not have significant effect on the electronic conductivity of all perovskites [20].

3. Perovskites Utilized in The Cathode

In the cathodic part of the fuel cell, oxygen enters the fuel cell and turns into oxygen ions through oxygen reduction reaction (ORR) [22, 23]. There are various perovskite-based materials that can make great cathodes. Perovskites with cobalt at the B-site of the perovskite structure have properties like reducing polarization resistance, and high conductivity that make them suitable materials for the cathode electrodes Figure 5 demonstrates the conductivity of a La-based perovskite. For instance, Meng et al investigated the conductivities and CTEs of $Pr_{1-x}Sr_xCo_{0.8}Fe_{0.2}O_{3-\delta}$ (x=0.2, 0.4, 0.6) perovskites and they reported that the sample with x=0.4 has the highest conductivity (1040 Sm^{-1}) among all perovskites. However, the CTEs of the samples were higher than the CTEs of standard electrolytes, thus, they cannot be used without further modifications in fuel cells to reduce CTEs [24].

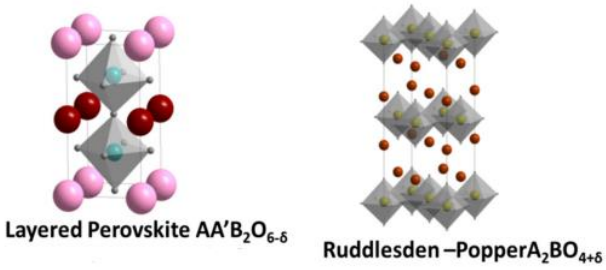

Figure 3. Different perovskite materials' structure [19]

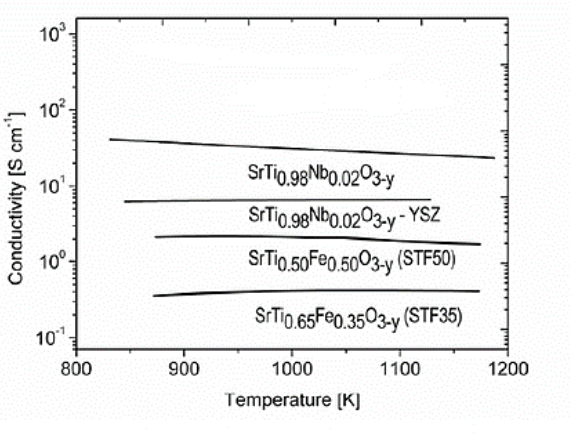

Figure 4. Electronic conductivity of STN and STF perovskites [20]

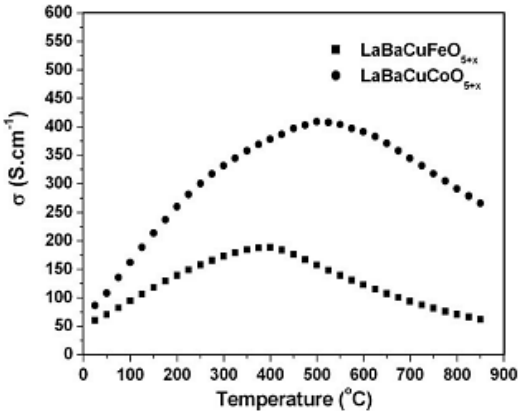

Figure 5. La-based perovskite showed better conductivity with Co rather than Fe in B-site [21]

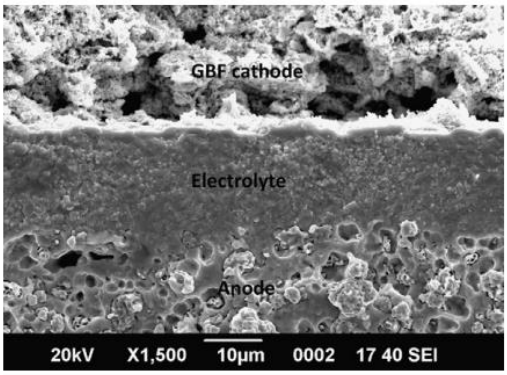

Figure 6. GBF cathode layer in a tri-layer cell [25]

Moreover, perovskites with Lanthanum at A-site with a transition metal at B-site because of high MIEC are one of the most promising cathode materials. Also, it is reported that at low temperatures, La-based perovskite materials have good porosity and ionic and electrical conductivity that make them a good choice for SOFC's electrodes [10].

$GdBaFe_2O_{5+\delta}$ (GBF) perovskites were synthesized using modified Pechini process and characterized by Ding et al [25] and the sample showed good catalytic activity for oxygen reduction. It also demonstrated the lowest polarization resistance 0.08 Ωcm^2 and the highest power density 861 $mWcm^{-2}$ at 700 ^{O}C. GBF cathode layer is demonstrated in Figure 6. Bebels et al investigated the electrochemical properties of $La_{0.58}Sr_{0.44}Co_{0.2}Fe_{0.8}O_{3-\delta}$, $La_{0.78}Sr_{0.2}Co_{0.2}Fe_{0.8}O_{3-\delta}$ and composite $La_{0.65}Sr_{0.3}MnO_{3-\delta}$ – 8 mol% Y_2O_3 stabilized ZrO_2 as cathode electrodes for SOFCs with $Ce_{0.8}Gd_{0.2}O_{2-\delta}$ (CGO) and YSZ as electrolyte at 600–850 ˚C using impedance spectroscopy and current-overpotential measurements. The perovskite materials were prepared by the spray-drying technique. Tests have demonstrated that the L_{78}SCF perovskite exhibits the lowest area specific polarization resistance RF (0.4 W cm^2 at 800 ˚C and PO_2 = 21 kPa) which means that this perovskite has the highest electrocatalytic activity among all other samples. [26].

Zhou et al [27] investigate $LaSrMnCoO_{5+\delta}$'s CTE and conductivity between 30-1000 ^{o}C and reported that the perovskite has higher CTE compared to YSZ, and $Sm_{0.2}Ce_{0.8}O_{1.9}$ (SDC) which are standard electrolytes, and lower conductivity than the $LnBaCo_2O_{5+\delta}$ perovskite. Nevertheless, it exhibited good thermal compatibility with SDC at 600-850 ^{o}C. Irshad et al studied the performance of a solid oxide fuel cell with a cobalt doped $LaNiO_3$ perovskite ($LaNi_{1-x}Co_xO_{3-\delta}$ (x = 0.4, 0.6, 0.8) as cathode electrode. The perovskite oxides were synthesized by high temperature decomposition in a furnace approach. Measurements reveal that $LaNi_{1-x}Co_xO_{3-\delta}$ (x =0.6) showed the highest value of conductivity (Figure 7) because of its porous and networked structure of sub micrometric grains. The maximum power density for the cell with $LaNi_{1-x}Co_xO_{3-\delta}$ (x = 0.6) as cathode was 0.45 Wcm^2[28]. Ling et al [29] observed the performance of cubic perovskite oxide $Sm_{0.5}Sr_{0.5}Fe_{0.8}Cu_{0.2}O_{3-\delta}$ (SSFCu) prepared by the modified Pechini method. They stated that the oxygen (O_2) vacancies enhanced which led to the improved electrochemical activity of the sample and the conductivity of the sample is about 72-82 S Cm^{-1} between 400-600 ^{o}C. They also mentioned that the CTEs of SSFC and SDC (as electrolyte) are about the same. The temperature dependence of the conductivity of the SSFC is depicted in Figure 8. Three cathode materials $La_{0.6}Sr_{0.4}Co_{0.2}Fe_{0.8}O_3$, $Ba_{0.5}Sr_{0.5}Co_{0.2}Fe_{0.8}O_3$, and $Sm_{0.5}Sr_{0.5}Co_{0.2}Fe_{0.8}O_3$ were studied by Shen et al [30] at various temperatures and it was understood that $La_{0.6}Sr_{0.4}Co_{0.2}Fe_{0.8}O_3$ had the highest conductivity (176 S cm^{-1}) at 300 ^{o}C. Mostafavi et al compared the properties of two different types of $La_{0.6}Sr_{0.4}Co_{0.2}Fe_{0.8}O_3$ (LSCF) powders (one prepared by co-precipitation method and the other one purchased from a commercial source) as cathode materials.

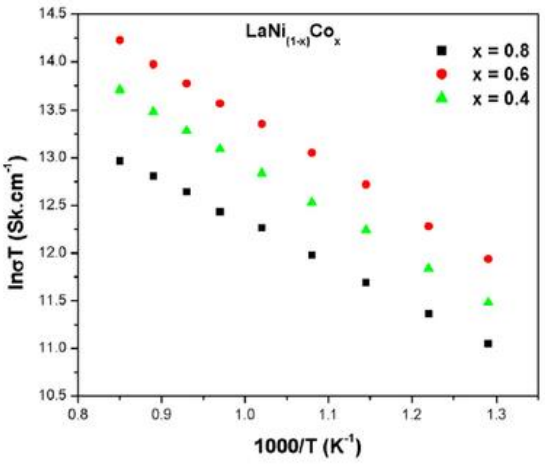

Figure 7. Comparison of electronic conductivity of $LaNi_{1-x}Co_x$ (x= 0.4, 0.6, and 0.8) [28]

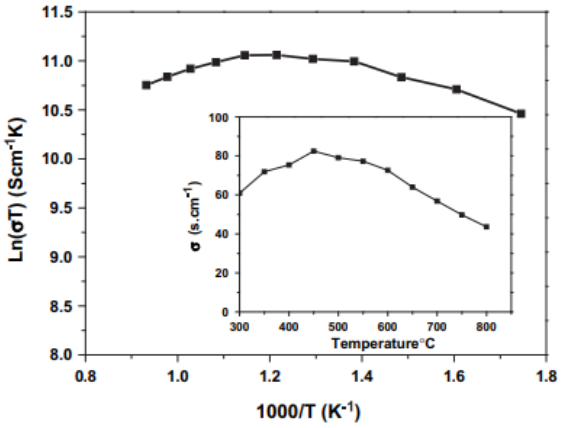

Figure 8. Electrical conductivities of SSFCu samples at different temperatures [29]

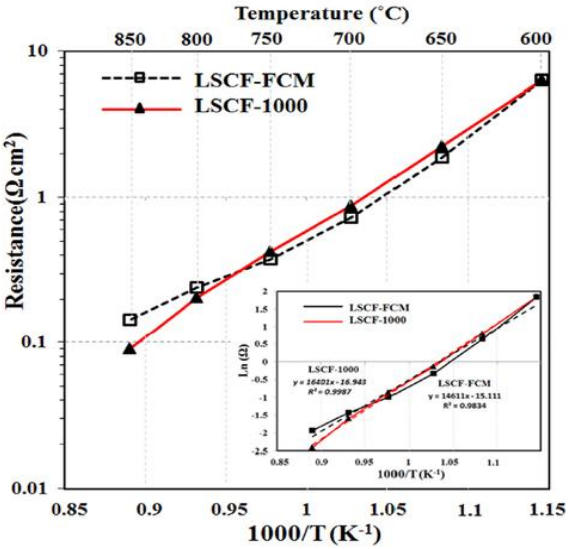

Figure 9. Comparison of resistance of two types of LSCF perovskites [31]

They studied various features of these perovskites such as electrochemical characteristics, morphology, phase composition and particle size and reported that polarization resistance and activation energy are almost the same for both powders and as it is illustrated in Figure 9 polarization resistance decreases when temperature increases. [31].

Choi et al [32] studied electrical conductivity of $Nd_{1-x}Sr_xCoO_{3-\delta}$ (NSC) with (x=0.3, 0.4, 0.5, 0.6, and 0.7) and stated that the conductivity of the samples improved with the increase of Sr content up to 0.5, but when the Sr content surpassed 0.5, due to more dominant ionic compensation, the electrical conductivity decreases.

The electrical conductivities of NSC perovskites are demonstrated in Figure 10.

Wu et al [33] investigated the characteristics of $La_{1-x}Sr_xCoO_{3-\delta}$(x=0-0.6) perovskites. The conductivities of the samples were dependent on the structure of the materials, the amount of dopants, and the temperature. The results showed the transferring semiconductor to a metallic behavior and among all the compositions the sample with x=0.4 demonstrated the best conductivity (2583 S Cm^{-1}) at 500 °C. However, the CTE of the sample was quite high in comparison with the standard electrolytes that could lead to the reduction of mechanical durability and the sample should be modified to have lower CTE. Hammouche et al [34] tested the thermal expansion coefficient and conductivities of $La_{1-x}Sr_xMnO_3$ system (x=0-0.5) and reported that all the samples CTEs are close to the standard electrolyte YSZ, nevertheless, the weakly doped compositions demonstrated the highest thermal compatibility with YSZ and the electrochemical activity of the samples increased with the increasing of dopant content. Ullmann et al measured the electrochemical (electrical conductivity and ionic transport) and other important properties (thermal expansion and oxygen deficiency) of $A_{1-a}A'_aBO_3$ perovskite-type materials (A=La, Pr, Ce; A=Sr; B=Mn, Fe, Co, Ni, Ga, Mg) as cathode. They stated that lanthanum manganite has the lowest thermal expansion coefficient and highest thermodynamic stability among all other perovskite-type oxides. They also found that the electronic conductivity is affected by Fe and Co in the b-site of the perovskite and ionic conductivity is related to the concentration of Sr in the A-site of the structure [35].

The crystal structure, electrical conductivity, and CTE of $NdBaCu_2O_{5+\delta}$ and $NdBa_{0.5}Sr_{0.5}Cu_2O_{5+\delta}$ were investigated by Kong et al [36] and they observed that the electrical conductivity of samples at 560 °C (16.87 S Cm^{-1}) and 545°C (51.92 S Cm^{-1}) are higher than conductivities at other temperatures due to some phase transitions. Also, it was reported that the CTE values of the samples were compatible with $Sm_{0.2}Ce_{0.8}O_{2-\delta}$ electrolyte.

The reduction in CTE values for these cobalt-free Nd-based perovskites is related to the spin-state transition of Cu and the absence of Co.

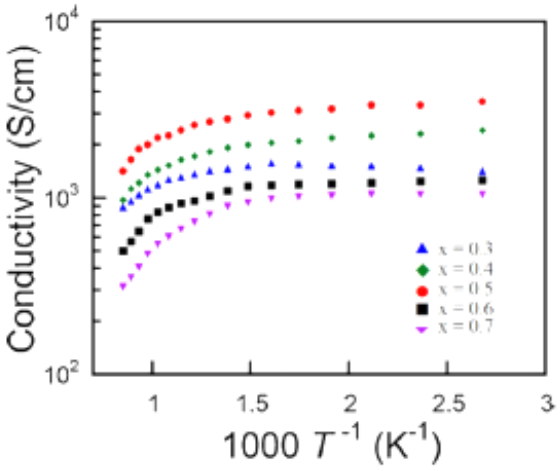

Figure 10. Electrical conductivities of NSC samples at different temperatures [6]

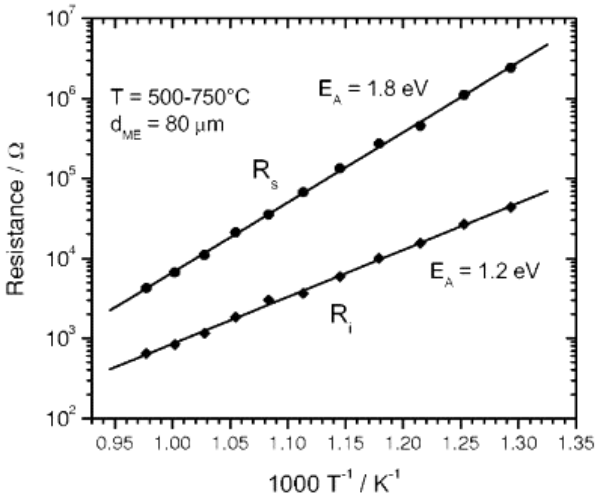

Figure 11. Resistance of BSCF perovskite at different temperatures [37]

The MICE perovskite materials like $Ba_{0.5}Sr_{0.5}Co_{0.8}Fe_{0.2}O_{3-\delta}$ (BSCF) and $La_{0.6}Sr_{0.4})_{0.9}Co_{0.8}Fe_{0.2}O_{3-\delta}$ (LSCF) were studied by Baumann et al [37] and the data exhibited that the surface exchange kinetics improved by the substitution of the A-site cation La in $La_{1-x}Sr_xCo_{1-y}Fe_yO_{3-\delta}$ by Sm and Ba. In fact, the electrochemical resistance was 0.09 Ωcm^2 for the BSCF at 750 °C. Resistance- Temperature diagram of BSCF is depicted in Figure11. Gędziorowski et al. [38] observed the features of Ba-doped $La_{1-x}Ba_xCo_{0.2}Fe_{0.8}O_{3-\delta}$ and stated that by increasing the amount of Ba the level of oxygen non-stoichiometry increased, as the result of reduction of the distortion of perovskite structure, which resulted in increasing conductivity; however, the conductivities were lower than the suitable amount for the cathode materials of SOFCs. Li et al [39] investigated the performance of $GdBaCo_2O_{5+\delta}$ perovskite material prepared by conventional ceramic method and they stated that the CTE values are close to the standard electrolyte material SDC and the electrical conductivity was 512-290 S Cm^{-1} in

the temperature range of 500-800 °C. The properties of Sr doped on $PrBa_{1-x}Sr_xCo_2O_{5+\delta}$ (x=0, 0.25, 0.5, 0.75, 1.0) double perovskites synthesized by the Pechini process were studied by Park et al [40] and it was stated that the electrical conductivity of $PrBa_{1-x}Sr_xCo_2O_{5+\delta}$ enhances with increasing Sr content because of higher oxygen content as a result of smaller size differences between Sr^{2+} and Pr^{3+} and special order of these ions layers in the structure of the double perovskites for all temperature regions. PrMnO perovskites' efficacy as SOFC cathode electrodes are investigated by Ishihara et al and they stated that Sr-doped material is better than the LSM oxides in terms of thermal expansion compatibility with YSZ electrolytes and low They also demonstrated low reactivity with YSZ and cathodic over-potential (Figure 12) as a result of high activity for the dissociation of oxygen [41].

4. Perovskites Utilized in The Anode

To choose appropriate anode materials for SOFCs, several characteristics should be considered. The materials should have a large surface area at TBP, sufficient porosity, high electronic conductivity, good electrocatalytic activity, stability, and thermal durability [42].

Different perovskite-based anode materials used in SOFCs have been studied. For instance, strontium doped lanthanum chromite (LSCr) perovskites exhibit improved properties (electrical conductivity, thermal durability, redox stability) when other cations with lower coordination numbers (such as Fe, Mn, Ni, and Co) are introduced to these materials [43].

Also, LaSrTiO3 materials due to their excellent electronic conductivity, great dimensional durability and outstanding chemical stability and, high sulfur and coking resistance can make great anode materials [44].

Moreover, there are ferrite-based perovskites that are suitable for SOFC anode applications such as SrFeO3, LaFeO3, and SmFeO3. Nevertheless, these single perovskites require some modifications (like doping with other metal cations with higher oxidation states) to enhance their electrical conductivity and chemical durability [45].

Chen et al developed a cathode-supported SOFC with GDC-impregnated $La_{0.75}Sr_{0.25}Cr_{0.5}Mn_{0.5}O_3$ (LSCM) anode electrode working with weakly humidified hydrogen and/ or methane as fuel and investigated the performance of the fuel cell at different temperatures. They stated that the performance of the cell is comparable to the cell made of Ni cermet while stable in weakly humidified methane fuel with 0.352 W/cm^2 maximum power density at 900°C [46].

The performances of various $La_{0.75}Sr_{0.25}Cr_{0.5}X_{0.5}O_{3\_\delta}$ samples prepared with combustion gel approach with X =Co, Fe, Ti, Mn were tested by Danilovic et al [47] as SOFCs anode. The results depicted that the sample with Co had the highest catalytic activity, while the one with Ti had the lowest catalytic activity when the fuel was CH_4. They, also, reported that the power density of the cell is the highest when the Fe was utilized as the dopant when the feed was CH_4 or H_2, but when the feed contained H_2S and CH_4 the sample with Ti showed the best performance.

Figure 13 depicts the power densities and conductivities of LSC perovskites. Fowler et al [48] investigated the application of $La_{1-x}Sr_xCr_xFe_{1-x}O_{3-\delta}$ material synthesized by solid-state reaction method as SOFC anode. It was reported that the $La_{0.33}Sr_{0.67}Cr_{0.33}Fe_{0.67}O_{3-\delta}$ exhibited the lowest anodic polarization resistance (0.275 Ωcm^2) at 800 °C due to the higher amount of oxygen loss when the content of Fe was high. Furthermore, these perovskites exhibited excellent ionic conductivity. The resistance of the perovskite versus temperature is demonstrated in Figure 14.

Chemical compatibility with different electrolytes and phase stability of $Sr_2BMoO_{6-\delta}$ (B = Mg, Ni and Co) and $Sr_2Fe_{1.5}Mo_{0.5}O_{6-\delta}$ double perovskites have been evaluated by Gomez et al. The findings show that the mentioned perovskites are highly reactive with $Zr_{0.84}Y_{0.16}O_{2-\delta}$ at 800 °C. Nevertheless, their reactivity with $Ce_{0.8}Gd_{0.2}O_{2-\delta}$ was low.

Both perovskites demonstrated low durability against carbonation in the intermediate temperature range 600–800 °C, but $Sr_2Fe_{1.5}Mo_{0.5}O_{6-\delta}$ showed stability in pure CO_2 and H_2 atmospheres [49].

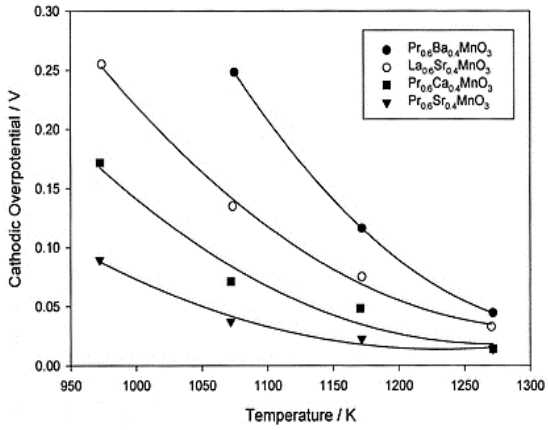

Figure 12. Cathodic overpotential of PrMnO and LSM perovskites [41]

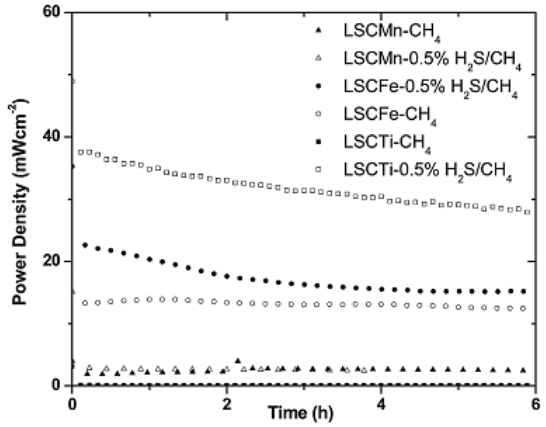

Figure 13. Power Densities of LSC perovskites with various dopants [47]

Li et al [50] tested the properties of different $(La_{0.3}Sr_{0.7})_{1-x}TiO_{3-\delta}$ (x = 0, 0.03, 0.05, 0.07, 0.10) perovskites, prepared by solid-state reaction approach, using an electron-blocking method and they stated that when the A-site deficiency increased the electronic conductivity decreased but the ionic conductivity increased. Moreover, it can improve the thermal durability of the samples and the samples showed stable electrical performance in different situations. The electrical conductivities of the samples are available in Figure 15.

Sun et al. [51] evaluated Mo doped $Pr_{0.5}Ba_{0.5}MnO_{3-\delta}$ (Mo-PBMO) double perovskite material synthesized by modified sol-gel approach as anode material for solid oxide fuel cell. The results of analyses showed that the perovskite has a large amount of oxygen deficiency. This property can improve the oxygen diffusion and electrochemical properties of the double perovskite by introducing Mo to the perovskite structure.

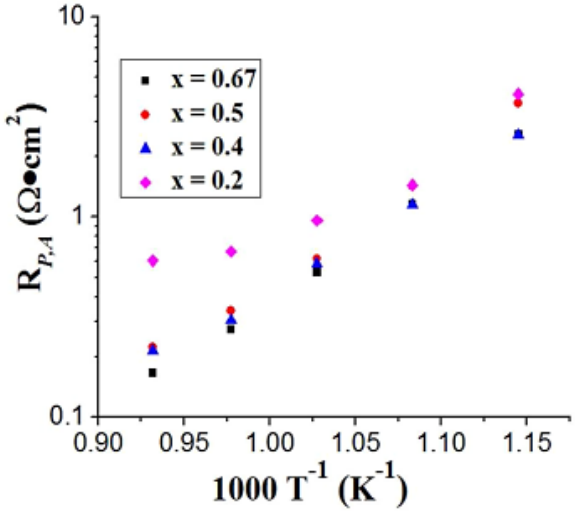

Figure 14. Resistance of LSCrFe samples at different temperatures [48]

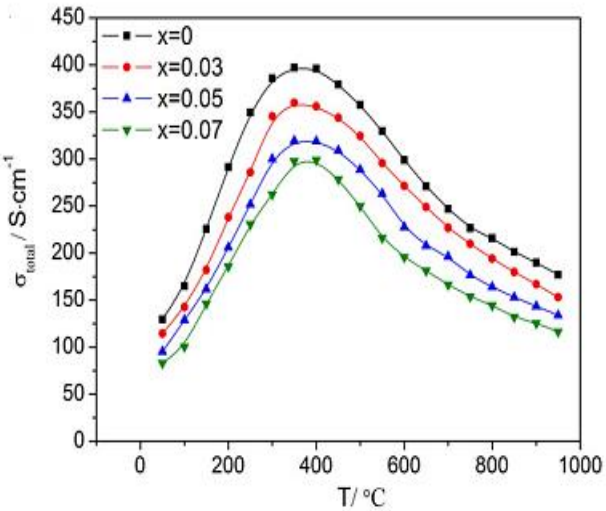

Figure 15. Conductivities of of LST samples at different temperatures [50]

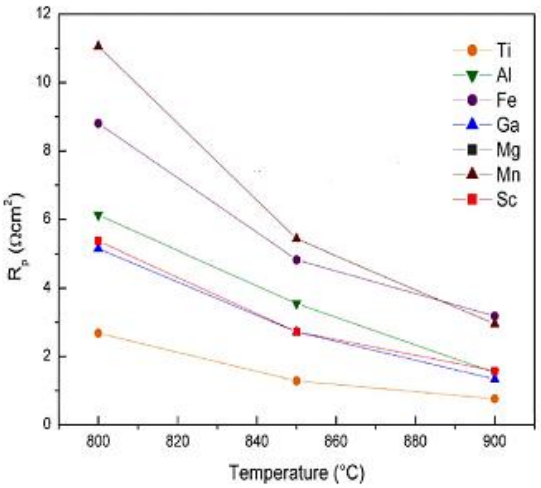

Figure 16. Polarization Resistance of LSTX-YSZ anodes with various dopants at different temperatures [54]

Its catalytic activity enhanced for H_2 and CH_4 oxidation reactions [51]. Steiger et al [52] studied the performance of $La_{0.3}Sr_{0.55}TiO_{3-\delta}$ (LST) and LSTN mixed perovskite-type structure using citrate gel method and they reported that good sulfur tolerance and stability, and 0.58 Ωcm^2 polarization resistance at 850 °C. Yoon et al [53] observed the effect of Co, Mn, and Fe doping in $La_{0.08}Sr_{0.92}M_{0.2}Ti_{0.8}O_{3-\delta}$ as SOFC anode with CH_4 as fuel. The results demonstrated that the Co and Fe doped perovskites showed higher catalytic activity ,which can be related to high oxygen vacancies and high multivalent redox couples' ratio. However, the sample exhibited high polarization resistance at 800 °C. Miller et al [54] tested the characteristics of $La_{0.33}Sr_{0.67}Ti_{0.92}X_{0.08}O_3$ doped with various dopants X (X = Al^{3+}, Ga^{3+}, Fe^{n+}, Mg^{2+}, Mn^{n+}, and Sc^{3+}), and they observed that the type of dopant can influence the redox characteristics, electrochemical performance, and morphology of the samples. It is also mentioned that at 900 °C $La_{0.33}Sr_{0.67}TiO_{3+\delta}$ sample had the lowest polarization resistance while the sample doped with Mg demonstrated the highest polarization resistance which is depicted in Figure 16.

Fu et al studied the performance of $La_{0.4}Sr_{0.6}Ti_{1-x}Mn_xO_{3-x}$ (x = 0, 0.2, 0.4, 0.6) perovskites as SOFCs' anode materials. The results revealed that the $La_{0.4}Sr_{0.6}Ti_{0.4}Mn_{0.6}O_{3-\delta}$ (LSTM4646) perovskite oxide is thermally compatible with the used electrolyte (YSZ) and shows low polarization resistance (0.32 Ωcm^2), high catalytic activity and stability in moderately humidified hydrogen atmosphere. the electronic conductivity is of 1/5 S/cm in wet Ar/4% H_2 (PO_2= 10−18 bar) at 810°C [55].

Choi et al [56] investigated the effect of doping Ce in $Sr_{1-x}Ce_xCo_{0.2}Fe_{0.8}O_{3-\delta}$ (x = 0.10, 0.15, and 0.20) samples prepared by EDTA-citrate complexing approach and they stated that the higher Ce doping in A-site could lead to more stable perovskites. In addition, the samples showed excellent

conductivity at temperatures <600 °C, but at higher temperatures, the samples break down and did not perform well. It is also mentioned that the sample with Ce demonstrated good sulfur tolerance in the presence of H_2S in the fuel. Cascos et al improved the characteristics of $SrMo_{1-x}M_xO_{3-\delta}$ (M = Fe and Cr, x = 0.1 and 0.2) perovskite materials to be used as intermediate temperature solid oxide fuel cells' anode electrode. They doped aliovalent Mg ions at the B-site of the perovskite oxide and test the fuel cell's output power at 850 ° C which was about 900 mW/cm^2. They reported high ion conductivity and good thermal compatibility with the LSGM electrolyte for $SrMoO_3$ perovskite [57].

As Figure 17 demonstrates, the electronic conductivity of the samples decreases by increasing the content of Mg. That would be due to this fact that Mg^{2+} ions can perturb the conduction paths. However, the obtained conductivities for x=0.1 and 0.2 (146 and 114 S cm^{-1} respectively) at 850 ° C are adequate for proper performance of the cell with hydrogen as fuel. The effect of doping Co on the electrochemical performance, stability, and sulfur tolerance of $La_{0.3}Sr_{0.7}Co_{0.07}Ti_{0.93}O_3$ perovskite was investigated by Cui et al [58].

The perovskite was synthesized by solid-state reaction method and it was reported that the electrocatalyst performance and electrical conductivity of the sample increased by the introduction of Co to its structure and it achieved the maximum 300 mW cm^{-2} power density at 900 °C in the presence of H_2S in the fuel. The Co nanoparticles on the surface can reduce the polarization resistance of the anode and also, the material showed high sulfur tolerance and redox stability. The Power Density-temperature diagram is depicted in Figure 18.

$Sr_2FeNb_{0.2}Mo_{0.8}O_{6-\delta}$ (SFNM20) double perovskite's performance as a solid oxide fuel cell's anode has been investigated by Ding et al and they reported that this anode materials showed significant performance, redox cycling in hydrocarbon fuels, and high resistance against carbon build-up. The SFNM20 perovskite demonstrated 5.3 S cm^{-1} electronic conductivity and 520 mW cm^{-2} maximum power density with hydrogen as fuel.

The perovskite material was durable when using different fuels (Figure 19). This figure confirms that the anode material is stable for different fuels and it has high fuel flexibility [59].

Research shows that the substitution of Sr, Ba, and Ce in the A-site of these perovskites can enhance their electrochemical properties. However, some studies suggest that the mentioned perovskite materials require further modification to have higher porosity, durability, and conductivity, therefore, further investigation is needed to tailor the structure and properties of perovskites in order to make them more attractive, applicable, and efficient choices for SOFCs. Table 2 contains a summary of the literature.

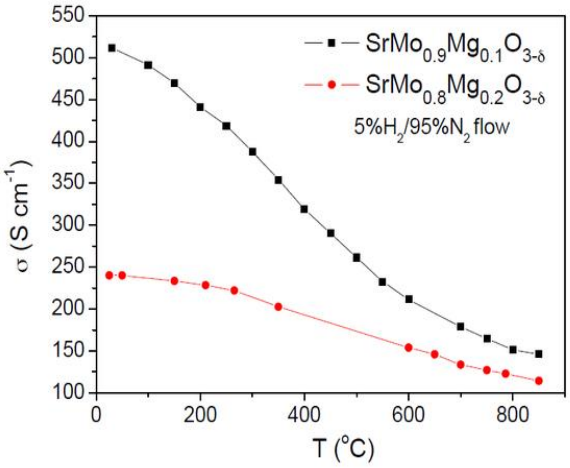

Figure 17. Electronic conductivity of SMMO perovskites [57]

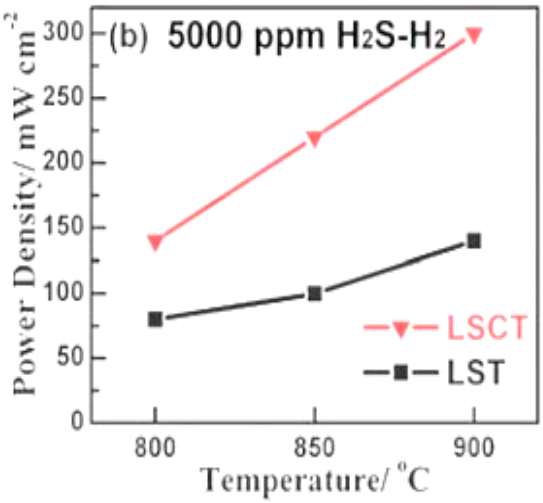

Figure 18. Power Densities of LST and LSCT perovskites with pure H_2/H_2S at different temperatures [58]

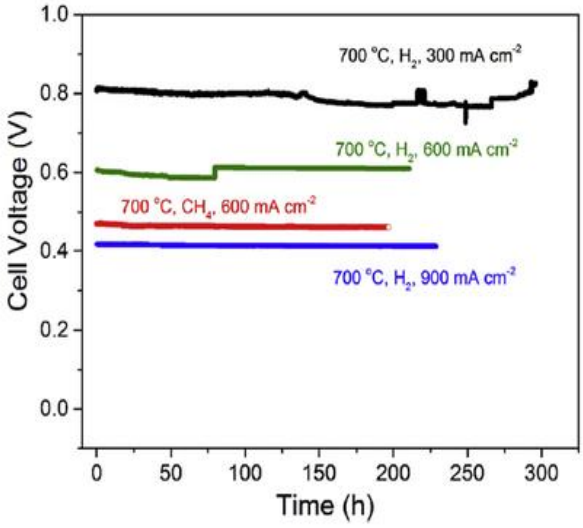

Figure 19. Durability of cell with various fuels [59]

Table 2. Summary of used perovskites as SOFCs anode, cathode and electrolyte

Application	Electrolyte	Cathode	Anode	Ref.
SOFC	$SrTi_{1-x}Nb_xO_{3-\delta}$ (x = 0.2)	$Ni_{0.8}Co_{0.15}Al_{0.05}LiO_2$ (NCAL)	$Ni_{0.8}Co_{0.15}Al_{0.05}LiO_2$ (NCAL)	[60]
SOFC	$Ba_{0.9}Sr_{0.1}Ce_{0.5}Zr_{0.35}Y_{0.1}Sm_{0.05}O_{3-\delta}$	$Ba_{0.5}Sr_{0.5}Co_{0.8}Fe_{0.2}O_{3-\delta}$	Ni-$Ba_{0.5}Sr_{0.5}Co_{0.8}Fe_{0.2}O_{3-\delta}$	[61]
SOFC	$La_{0.8}Sr_{0.2}Ga_{0.7}Mg_{0.3}O_{3-\delta}$	$La_{0.8}Sr_{0.2}MnO_3$	$La_{0.75}Sr_{0.25}Cr_{0.5}Mn_{0.5}O_3$	[62]
SOFC	$La_{0.8}Sr_{0.2}Ga_{0.8}Mg_{0.2}O_3$	$La_{0.6}Sr_{0.4}Fe_{0.8}Co_{0.2}O_3$	$La_{0.6}Sr_{0.4}Fe_{0.8}Co_{0.2}O_3$	[63]
SOFC	$LaGaO_3$	_	Nickel–Gd-doped CeO	[64]
SOFC	Fe-doped $SrTiO_{3-\delta}$	_	_	[65]
SOFC	(La, Sr)(Ga, Mg)O_3	(La,Sr)CoO_3	(La,Sr)(Ga,Mn)O_3	[66]
SOFC	$La_{0.9}Sr_{0.1}Ga_{0.8}Mg_{0.2}O_{2.85}$	$La_{0.75}Sr_{0.25}Cr_{0.5}X_{0.5}O_{3-\delta}$ (X_ = Mn, Fe & Al)	$La_{0.75}Sr_{0.25}Cr_{0.5}X_{0.5}O_{3-\delta}$(X_ = Mn, Fe & Al)	[67]
SOFC	$La_{0.8}Sr_{0.2}Ga_{0.8}Mg_{0.15}Co_{0.05}O_{3-\delta}$	$(La_{0.75}Sr_{0.25})Cr_{0.5}Mn_{0.5}O_{3-\delta}$	$Gd_{0.4}Sr_{0.6}CoO_{3-\delta}$	[68]
SOFC	$BaZr_{0.85}Y_{0.15}O_3$	Ni	$La_{0.6}Sr_{0.4}Fe_{0.8}Co_{0.2}O_3$	[69]
SOFC	$LaGaO_3$	$Ba_{0.6}La_{0.4}CoO_3$.	Ni–Fe bimetal	[70]
SOFC	$La_{0.9}Sr_{0.1}Ga_{0.8}Mg_{0.2}O_3$	$La_{0.6}Sr_{0.4}Ga_{0.3}Fe_{0.7}O_3$	$La_{0.6}Sr_{0.4}Ga_{0.3}Fe_{0.7}O_3$	[71]
SOFC	$La_{0.8}Sr_{0.2}Ga_{0.8}Mg_{0.2}O_3$	$SrFe_{0.9-x}Cu_xW_{0.1}O_{3-\delta}$	_	[72]
SOFC	La-$BaZrYO_{3-\delta}$	$Ni_{0.8}Co_{0.15}Al_{0.05}LiO_2$ (NCAL)	$Ni_{0.8}Co_{0.15}Al_{0.05}LiO_2$ (NCAL)	[73]
SOFC	$BaCe_{0.7-x}Sm_xZr_{0.2}Y_{0.1}O_{3-\delta}$	Ni- $BaCe_{0.7-x}Sm_xZr_{0.2}Y_{0.1}O_{3-\delta}$	_	[74]
SOFC	$La_xSr_{1-x}Ga_yMg_{1-y}O_{3-\delta}$	$Pr_{0.8}Sr_{0.2}Co_xZ_{1-x}O_{3-d}$, (Z=Mn, Fe)	_	[75]
SOFC	Al-doped $La_{1-x}Sr_xScO_3$	_	_	[76]

5. Conclusions

Fuel cells are among the significant electricity producers. One of the major drawbacks of the SOFCs that can lead to several problems like thermal degradation and long start-up time is the high operating temperature of the cell (800-1000 ^oC). To reduce the operating temperature to intermediate (600-800 ^oC) or lower temperature usage of some specific materials for both electrodes is necessary. Perovskite-based materials are proven to be appropriate materials to have efficient SOFCs at low or intermediate temperatures. In this review, we focused on the studies that investigated the characteristics and performance of various perovskite-based materials to give a comprehensive view of the approaches that can be utilized to improve the efficiency of the solid oxide fuel cells at lower temperatures. It is understood from the literature that is reviewed that the introduction of various dopants is a promising approach to modify the characteristics of the perovskites and make them suitable electrodes for SOFCs. La and Sm- based perovskites with Co, Cr, or Ti in B-site of the mixed oxides showed good electrocatalytic activity, conductivity, expansion compatibility with standard electrolytes (YSZ- SDC), stability, and in some cases excellent sulfur tolerance as SOFC's anode and cathode material.

Declaration

The authors declared no potential conflicts of interest with respect to the research, authorship, and/or publication of this article. The authors also declared that this article is original, was prepared in accordance with international publication and research ethics, and ethical committee permission or any special permission is not required.

Author Contributions

All authors conceived the study together. N. Caylak Delibaş and A. Niaei contributed to the formation of the idea, and in scientific support, S.B. Gharamaleki and M. Mansouri were in charge of the preparation of the literature review, and writing the article.

References

1. Kanmaz, İ. and Ü. Abdullah, *Silicon dioxide thin films prepared by spin coating for the application of solar cells.* International Advanced Researches and Engineering Journal, 2021. 5(1): p. 14-18.
2. Turkboyları, E.Y. and A.N. Yuksel, *Use of solar panels in greenhouse soil disinfection,* International Advanced Researches and Engineering Journal, 2018. 2(2): p. 195-199.

3. Sengodan, S., et al., *Layered oxygen-deficient double perovskite as an efficient and stable anode for direct hydrocarbon solid oxide fuel cells*, Nature materials, 2015. 14(2): p. 205-209.
4. Abdalla, A.M., et al., *Achievements and trends of solid oxide fuel cells in clean energy field: a perspective review*, Frontiers in Energy, 2018: p. 1-24.
5. Mendonça, C., A. Ferreira, and D.M. Santos, *Towards the Commercialization of Solid Oxide Fuel Cells*, Recent Advances in Materials and Integration Strategies. Fuels, 2021. 2(4): p. 393-419.
6. Jun, A., et al., *Perovskite as a cathode material: a review of its role in solid-oxide fuel cell technology*, ChemElectroChem, 2016. 3(4): p. 511-530.
7. Afroze, S., et al., *Latest development of double perovskite electrode materials for solid oxide fuel cells: a review*, Frontiers in Energy, 2019. 13(4): p. 770-797.
8. Wachsman, E.D. and K.T. Lee, *Lowering the temperature of solid oxide fuel cells*, Science, 2011. 334(6058): p. 935-939.
9. Thakur, S., O. Pandey, and K. Singh, *A comparative structural, thermal and electrical study of Ca^{2+}, Sr^{2+} substituted $BiMnO_3$*, Solid State Ionics, 2014. 268: p. 23-30.
10. Kaur, P. and K. Singh, *Review of perovskite-structure related cathode materials for solid oxide fuel cells*, Ceramics International, 2020. 46(5): p. 5521-5535.
11. Ding, P., et al., *Review on Ruddlesden–Popper perovskites as cathode for solid oxide fuel cells*, Journal of Physics: Materials, 2021. 4(2): p. 022002.
12. Tarragó, D.P., et al., *Perovskites used in fuel cells. Pan, Likun; Zhu, Guang (ed.). Perovskite materials: synthesis, characterisation, properties, and applications [recurso eletrônico]*, [Rijeka, Croatia]: InTech, 2016. ch. 21, p. 619-637, 2016.
13. Azad, A.K., *Synthesis, structure, and magnetic properties of double perovskites of the type A_2MnBO_6 and A_2FeBO_6;(A= Ca, Sr, Ba, La; B= W, Mo, Cr)*. Thesis for: PhD, Advisor: Professor Sten Eriksson, March 2004.
14. Atta, N.F., A. Galal, and E. El-Ads, *Perovskite nanomaterials–synthesis, characterization, and applications*, Perovskite Materials–Synthesis, Characterisation, Properties, and Applications; Pan, L., Ed, 2016: p. 107-151.
15. Zhou, X., et al., *Progress in La-doped $SrTiO_3$ (LST)-based anode materials for solid oxide fuel cells*, Rsc Advances, 2014. 4(1): p. 118-131.
16. Johnsson, M. and P. Lemmens, *Crystallography and chemistry of perovskites*, Handbook of magnetism and advanced magnetic materials, 2007.
17. Burnwal, S.K., S. Bharadwaj, and P. Kistaiah, *Review on MIEC cathode materials for solid oxide fuel cells*, Journal of Molecular and Engineering Materials, 2016. 4(02): p. 1630001.
18. Sengodan, S., et al., *Self-decorated MnO nanoparticles on double perovskite solid oxide fuel cell anode by in situ exsolution*, ACS Sustainable Chemistry & Engineering, 2017. 5(10): p. 9207-9213.
19. Klyndyuk, A.I., et al., *Layered Oxygen-Deficient Double Perovskites as Promising Cathode Materials for Solid Oxide Fuel Cells*, Materials, 2022. 15(1): p. 141.
20. Gazda, M., et al. *Perovskites in solid oxide fuel cells. in Solid State Phenomena*, 2012. Trans Tech Publ.
21. Hussain, S. and L. Yangping, *Review of solid oxide fuel cell materials: cathode, anode, and electrolyte*, Energy Transitions, 2020: p. 1-14.
22. Lan, R., et al., *A perovskite oxide with high conductivities in both air and reducing atmosphere for use as electrode for solid oxide fuel cells*, Scientific reports, 2016. 6(1): p. 1-8.
23. Zhou, Q., et al., *Electrochemical performances of $LaBaCuFeO_{+x}$ and $LaBaCuCoO_{5+x}$ as potential cathode materials for intermediate-temperature solid oxide fuel cells*, Electrochemistry Communications, 2009. 11(1): p. 80-83.
24. Meng, X., et al., *Characterization of $Pr_{1-x}Sr_xCo_{0.8}Fe_{0.2}O_{3-\delta}$ ($0.2 \leq x \leq 0.6$) cathode materials for intermediate-temperature solid oxide fuel cells*, Journal of Power Sources, 2008. 183(2): p. 581-585.
25. Ding, H. and X. Xue, *Cobalt-free layered perovskite $GdBaFe_2O_{5+x}$ as a novel cathode for intermediate temperature solid oxide fuel cells*, Journal of Power Sources, 2010. 195(15): p. 4718-4721.
26. Bebelis, S., et al., *Electrochemical characterization of perovskite-based SOFC cathodes*, Journal of applied electrochemistry, 2007. 37(1): p. 15-20.
27. Zhou, Q., et al., *LaSrMnCoO5+ δ as cathode for intermediate-temperature solid oxide fuel cells*, Electrochemistry communications, 2012. 19: p. 36-38.
28. Irshad, M., et al., *Electrochemical evaluation of mixed ionic electronic perovskite cathode $LaNi_{1-x}Co_xO_{3-\delta}$ for IT-SOFC synthesized by high temperature decomposition*, International Journal of Hydrogen Energy, 2021. 46(17): p. 10448-10456.
29. Ling, Y., et al., *Investigation of cobalt-free cathode material Sm0.5Sr0.5Fe0.8Cu0.2O3− δ for intermediate temperature solid oxide fuel cell*, International journal of hydrogen energy, 2010. 35(13): p. 6905-6910.
30. Shen, F. and K. Lu, *Perovskite-type $La_{0.6}Sr_{0.4}Co_{0.2}Fe_{0.8}O_3$, $Ba_{0.5}Sr_{0.5}Co_{0.2}Fe_{0.8}O_3$, and Sm0.5Sr0.5Co0.2Fe0.8O3 cathode materials and their chromium poisoning for solid oxide fuel cells*, Electrochimica Acta, 2016. 211: p. 445-452.
31. Mostafavi, E., A. Babaei, and A. Ataie, *$La_{0.6}Sr_{0.4}Co_{0.2}Fe_{0.8}O_3$ perovskite cathode for intermediate temperature solid oxide fuel cells: a comparative study*, Iranian Journal of Hydrogen & Fuel Cell, 2015. 1(4): p. 239-246.
32. Choi, S., et al., *Chemical compatibility, redox behavior, and electrochemical performance of $Nd_{1-x}Sr_xCoO_{3-\delta}$ cathodes based on $Ce_{1.9}Gd_{0.1}O_{1.95}$ for intermediate-temperature solid oxide fuel cells*, Electrochimica acta, 2012. 81: p. 217-223.
33. Wu, Y.-C., et al, *Properties and microstructural analysis of $La_{1-x}Sr_xCoO_{3-\delta}$ (x= 0–0.6) cathode materials*, Ceramics International, 2017. 43(2): p. 2460-2470.
34. Hammouche, A., E. Siebert, and A. Hammou, *Crystallographic, thermal and electrochemical properties of the system $La_{1-x}Sr_xMnO_3$ for high temperature solid electrolyte fuel cells*, Materials Research Bulletin, 1989. 24(3): p. 367-380.
35. Ullmann, H., et al., *Correlation between thermal expansion and oxide ion transport in mixed conducting perovskite-type oxides for SOFC cathodes*, Solid state ionics, 2000. 138(1-2): p. 79-90.
36. Kong, X., et al., *$NdBaCu_2O_{5+\delta}$ and $NdBa_{0.5}Sr_{0.5}Cu_2O_{5+\delta}$ layered perovskite oxides as cathode materials for IT-SOFCs*, International Journal of Hydrogen Energy, 2015. 40(46): p. 16477-16483.

37. Baumann, F., et al., *Quantitative comparison of mixed conducting SOFC cathode materials by means of thin film model electrodes*, Journal of The Electrochemical Society, 2007. 154(9): p. B931.
38. Gędziorowski, B., et al, *$La_{1-x}Ba_xCo_{0.2}Fe_{0.8}O_{3-\delta}$ perovskites for application in intermediate temperature SOFCs*, Solid State Ionics, 2012. 225: p. 437-442.
39. Li, N., et al., *Characterization of $GdBaCo_2O_{5+\delta}$ cathode for IT-SOFCs*, Journal of Alloys and Compounds, 2008. 454(1-2): p. 274-279.
40. Park, S., et al., *Strontium doping effect on high-performance $PrBa_{1-x}Sr_xCo_2O_{5+\delta}$ as a cathode material for IT-SOFCs*, ECS Electrochemistry Letters, 2012. 1(5): p. F29.
41. Ishihara, T., et al., *Doped PrMnO3 perovskite oxide as a new cathode of solid oxide fuel cells for low temperature operation*, Journal of the Electrochemical Society, 1995. 142(5): p. 1519.
42. Zhou, X. and F. Zhou, *Application of $La_{0.3}Sr_{0.7}Fe_{0.7}Ti_{0.3}O_{3-\delta}$ GDC electrolyte in LT-SOFC*, International Journal of Hydrogen Energy, 2021. 46(15): p. 9988-9995.
43. Aliotta, C., et al., *Direct methane oxidation on $La_{1-x}Sr_xCr_{1-y}Fe_yO_{3-\delta}$ perovskite-type oxides as potential anode for intermediate temperature solid oxide fuel cells*, Applied Catalysis B: Environmental, 2016. 180: p. 424-433.
44. Cowin, P.I., et al., *Recent progress in the development of anode materials for solid oxide fuel cells*, Advanced Energy Materials, 2011. 1(3): p. 314-332.
45. Cheng, Y., et al., *Investigation of Ba fully occupied A-site $BaCo_{0.7}Fe_{0.3-x}Nb_xO_{3-\delta}$ perovskite stabilized by low concentration of Nb for oxygen permeation membrane*, Journal of Membrane Science, 2008. 322(2): p. 484-490.
46. Chen, X., et al., *High-performance cathode-supported SOFC with perovskite anode operating in weakly humidified hydrogen and methane*, Fuel Cells Bulletin, 2007. 2007(6): p. 12-16.
47. Danilovic, N., et al., *Correlation of fuel cell anode electrocatalytic and ex situ catalytic activity of perovskites $La_{0.75}Sr_{0.25}5Cr_{0.5}X_{0.5}O_{3-\delta}$ (X= Ti, Mn, Fe, Co)*, Chemistry of Materials, 2010. 22(3): p. 957-965.
48. Fowler, D.E., et al., *Stable, low polarization resistance solid oxide fuel cell anodes: $La_{1-x}Sr_xCr_{1-x}Fe_xO_{3-\delta}$ (x= 0.2–0.67)*, Chemistry of Materials, 2014. 26(10): p. 3113-3120.
49. Dos Santos-Gómez, L., et al., *Chemical stability and compatibility of double perovskite anode materials for SOFCs*, Solid State Ionics, 2013. 239: p. 1-7.
50 Li, X., et al., *Electrical conductivity and structural stability of La-doped $SrTiO_3$ with A-site deficiency as anode materials for solid oxide fuel cells*, International journal of hydrogen energy, 2010. 35(15): p. 7913-7918.
51. Sun, Y.-F., et al., *Molybdenum doped $Pr_{0.5}Ba_{0.5}MnO_{3-\delta}$ (Mo-PBMO) double perovskite as a potential solid oxide fuel cell anode material*, Journal of Power Sources, 2016. 301: p. 237-241.
52. Steiger, P., et al., *Sulfur poisoning recovery on a solid oxide fuel cell anode material through reversible segregation of nickel*, Chemistry of Materials, 2019. 31(3): p. 748-758.
53. Yoon, J.S., et al., *Catalytic activity of perovskite-type doped $La_{0.08}Sr_{0.92}Ti_{1-x}M_xO_{3-\delta}$ (M= Mn, Fe, and Co) oxides for methane oxidation*, international journal of hydrogen energy, 2014. 39(15): p. 7955-7962.
54. Miller, D.N. and J.T. Irvine, *B-site doping of lanthanum strontium titanate for solid oxide fuel cell anodes*, Journal of Power Sources, 2011. 196(17): p. 7323-7327.
55. Fu, Q., F. Tietz, and D. Stöver, *$La_{0.4}Sr_{0.6}Ti_{1-x}Mn_xO_{3-\delta}$ perovskites as anode materials for solid oxide fuel cells*, Journal of the Electrochemical Society, 2006. 153(4): p. D74.
56. Choi, H., et al., *Effect of Ce doping on the performance and stability of strontium cobalt ferrite perovskites as SOFC anode catalysts*, Topics in Catalysis, 2015. 58(4-6): p. 359-374.
57. Cascos, V., J.A. Alonso, and M.T. Fernández-Díaz, *Novel Mg-doped $SrMoO_3$ perovskites designed as anode materials for solid oxide fuel cells*, Materials, 2016. 9(7): p. 588.
58. Cui, S.-H., et al., *Cobalt doped $LaSrTiO_{3-\delta}$ as an anode catalyst: effect of Co nanoparticle precipitation on SOFCs operating on H_2 S-containing hydrogen*, Journal of Materials Chemistry A, 2013. 1(34): p. 9689-9696.
59. Ding, H., et al., *A redox-stable direct-methane solid oxide fuel cell (SOFC) with $Sr_2FeNb_{0.2}Mo_{0.8}O_{6-\delta}$ double perovskite as anode material*, Journal of Power Sources, 2016. 327: p. 573-579.
60. Shah, M. Y, et al, *Semiconductor Nb-Doped $SrTiO_{3-\delta}$ Perovskite Electrolyte for a Ceramic Fuel Cell*, ACS Applied Energy Materials, 2021. 4(1): p. 365-375.
61. Radenahmad, N., et al, *A new high performance proton-conducting electrolyte for next generation solid oxide fuel cells*, Energy Technology, 2020. 8(9): 2000486.
62. Mohammadi, A., et al, *All-Perovskite Solid Oxide Fuel Cells*, Synthesis and Characterization. (2009).
63. Faro, M. L., and Aricò, A. S,. *Electrochemical behaviour of an all-perovskite-based intermediate temperature solid oxide fuel cell*, International journal of hydrogen energy, 2013. 38(34): p. 14773-14778.
64 . Ishihara, T., et al, *Nickel–Gd-doped CeO_2 cermet anode for intermediate temperature operating solid oxide fuel cells using LaGaO3-based perovskite electrolyte*, Solid State Ionics, 2000. 132(3-4): p 209-216.
65. Shah, M. Y., et al, *Semiconductor Fe-doped $SrTiO_{3-\delta}$ perovskite electrolyte for low-temperature solid oxide fuel cell (LT-SOFC) operating below 520 ^oC*, Int J Hydrogen Energy, 2020. 45(28): 1447.
66. Hsu, M. F., et al, *Solid oxide fuel cell fabricated using all-perovskite materials*, Electrochemical and Solid State Letters, 2006. 9(4): A193.
67. Martínez, J.,et al, *Performance of XSCoF (X= Ba, La and Sm) and LSCrX'(X'= Mn, Fe and Al) perovskite-structure materials on LSGM electrolyte for IT-SOFC*, Electrochimica acta, 2007. 52(9): p. 2950-2958.
68. Tao, S. W., et al, *An efficient solid oxide fuel cell based upon single phase perovskites*, Advanced Materials, 2005. 17(14): p. 1734-1737.
69. Serra, J. M., and Meulenberg, W. A thin, *Film proton $BaZr_{0.8}5Y_{0.15}O_3$ conducting electrolytes: toward an intermediate-temperature solid oxide fuel cell alternative*, Journal of the American Ceramic Society, . 2007. 90(7): p. 2082-2089.
70. Ishihara, T., et al, *Intermediate temperature solid oxide electrolysis cell using $LaGaO_3$ based perovskite electrolyte*, Energy & Environmental Science, 2010. 3(5): p. 665-672.
71. Glisenti A. et al, Reversible, *all-perovskite SOFCs based on La, Sr gallates*, Int. Journal of Hydrogen Energy, 2020. 45(2020): 29155e29165.
72. Chuangang Yao et al., *Copper doped SrFe 0.9-x Cu x W 0.1 O 3-δ (x = 0–0.3) perovskites as cathode materials for IT-*

SOFCs, Journal of Alloys and Compounds, 2021. 868: 159127.

73. Shah, M. Y., et al, *Advanced fuel cell based on semiconductor perovskite LaeBaZrYO$_{3-\delta}$ as an electrolyte material operating at low temperature 550 ^{o}C*, Int. J. Hydrogen Energy, 2020. p.45, 51.
74. Irshad M., et al,, *Electrochemical Investigations of BaCe$_{0.7-x}$Sm$_x$Zr$_{0.2}$Y$_{0.1}$ O$_{3-\delta}$ Sintered at a Low Sintering Temperature as a Perovskite Electrolyte for IT-SOFCs*, Sustainability 2021, 13: p. 12595.
75. Kostogloudis, G. C., et al, *Chemical compatibility of alternative perovskite oxide SOFC cathodes with doped lanthanum gallate solid electrolyte*, Solid State Ionics, 2000. 134(1-2), p. 127-138.
76. Kato, H., et al, *Electrical conductivity of Al-doped La$_{1-x}$Sr$_x$ScO$_3$ perovskite-type oxides as electrolyte materials for low-temperature SOFC*, Solid State Ionics, 2003. 159(3-4), p. 217-222.